

**Investigation of Coupled Electron and Proton Transfer in the
Quinol:Fumarate Reductase from *Wolinella succinogenes* with
Electrochemically Induced FTIR and VIS Difference Spectroscopy
and Multiconformation Continuum Electrostatic Calculations**

Dissertation

zur Erlangung des Doktorgrades
der Naturwissenschaften

vorgelegt beim Fachbereich Physik
der Johann Wolfgang Goethe-Universität
in Frankfurt am Main

von

Alexander H. Haas
aus Frankfurt am Main

Frankfurt am Main, 2004

(D F 1)

vom Fachbereich Physik der Johann Wolfgang Goethe–Universität als Dissertation
angenommen.

Dekan: Prof. Dr. Wolf Aßmus

Erster Gutacher: Prof. Dr. Werner Mäntele

Zweiter Gutachter: PD Dr. C. Roy D. Lancaster

Datum der Disputation: 02. September 2004

VERÖFFENTLICHUNGEN

Die meisten Ergebnisse dieser Arbeit sind veröffentlicht oder hierfür in Vorbereitung:

Lancaster, C. R. D., Groß, R., Haas, A., Ritter, M., Mäntele, W., Simon, J., and Kröger, A. (2000) Essential role of Glu-C66 for menaquinol oxidation indicates transmembrane electrochemical potential generation by *Wolinella succinogenes* fumarate reductase, *Proc. Natl. Acad. Sci. USA* 97, 13051–13056.

Haas, A. H., and Lancaster, C. R. D. (2004) Calculated coupling of transmembrane electron and proton transfer in dihemic quinol:fumarate reductase, *Biophys. J.* 87, 4298–4315.

Haas, A. H., Sauer, U. S., Groß, R., Simon, J., Mäntele, W., and Lancaster, C. R. D. (2004) FTIR difference spectra of *Wolinella succinogenes* quinol:fumarate reductase support a key role of Glu C180 within the “E-pathway hypothesis” of coupled transmembrane electron and proton transfer, *manuscript in preparation*.

Haas, A. H., Mäntele, W., and Lancaster, C. R. D. (2004) VIS spectroscopic observation of a redox Bohr effect in wild-type and variant E180Q of quinol:fumarate reductase from *Wolinella succinogenes*, *manuscript in preparation*.

Mileni, M., Haas, A. H., Mäntele, W., Simon, J., and Lancaster, C. R. D. (2004) Support for an involvement of heme propionates in coupled transmembrane electron and proton transfer in dihemic quinol:fumarate reductase by ¹³C-labeling and FTIR-spectroscopy, *manuscript in preparation*.

Lancaster, C. R. D., Sauer, U. S., Groß, R., Haas, A. H., Mäntele, W., Simon, J., and Madej, M. G. (2004) Experimental support for the “E-pathway” hypothesis of coupled transmembrane e⁻ and H⁺ transfer in dihemic quinol:fumarate reductase, *manuscript in preparation*.

ZUSAMMENFASSUNG

Das Enzym Chinol:Fumarat-Reduktase (QFR) des anaeroben ϵ -Proteobakteriums *Wolinella succinogenes* ist Teil der anaeroben Atmungskette dieses Organismus. QFR koppelt die Reduktion von Fumarat zu Succinat an die Oxidation von Menachinol zu Menachinon. In *W. succinogenes* ist Fumarat der terminale Elektronenakzeptor, und der Organismus verwendet z. B. die Substrate Formiat oder molekularen Wasserstoff als Elektronendonator. Der gemeinsame katalytische Substratumsatz der QFR zusammen mit entweder der Hydrogenase oder der Formiat-Dehydrogenase trägt zum Aufbau eines elektrochemischen Protonenpotentials über die bakterielle Cytoplasmamembran bei. Dieses Potential wird von der ATP-Synthase zur Phosphorylierung von ADP mit anorganischem Phosphat (P_i) zu ATP benützt. Zusätzlich zu einem kovalent gebundenen FAD in der A-Untereinheit des Enzyms und drei Eisen-Schwefelzentren in der B-Untereinheit bindet QFR ein Niedrig- und ein Hochpotential-Häm, wie abschließend in der röntgenkristallographisch ermittelten dreidimensionalen Proteinstruktur bei einer Auflösung von 2.2 Å gezeigt werden konnte (Lancaster *et al.*, 1999, *Nature* 402, 377–385). Beide Häme sind offenbar Teil der Elektronentransportkette zwischen den beiden katalytischen Zentren dieses Redox-Enzyms. Die Mittelpunktspotentiale der beiden Hämgruppen sind bekannt, ihre Zuordnung zur distalen und proximalen Position im Enzym jedoch nicht.

Des weiteren wurde für die QFR von *W. succinogenes* ein neuartiger Mechanismus der Kopplung von transmembranen Elektronen- und Protonentransfer, die sogenannte „E-Weg“ Hypothese (Lancaster, 2002, *Biochim. Biophys. Acta* 1565, 215–231), vorgeschlagen.

Das Ziel dieser Arbeit war die genauere Charakterisierung der mechanistischen Beziehung zwischen Struktur und Funktion der QFR, und die detaillierte Untersuchung des vorgeschlagenen Kopplungsmechanismus (der „E-Weg“ Hypothese) mit Hilfe von rechnergestützten elektrostatischen Rechnungen auf Grundlage der röntgenkristallographischen Strukturkoordinaten sowie mit Hilfe von elektrochemisch induzierter FTIR- und VIS-Differenzspektroskopie am QFR Wild-Typ und an verschiedenen zur Verfügung stehenden Enzymvarianten (insbesondere der Variante E180Q, in welcher der entsprechende Rest Glu C180 durch ein Glutamin ersetzt wurde).

- 1.) Im Verlaufe dieser Arbeit konnte gezeigt werden, daß die di-hämhaltige QFR stabile und reproduzierbare elektrochemisch induzierte FTIR-Differenzbanden im mittleren infraroten Spektralbereich zwischen 1800 und 1000 Wellenzahlen (cm^{-1}) aufweist, welche Übergänge des Enzyms zwischen dem oxidierten und reduzierten Zustand der QFR widerspiegeln. Die spektralen Signaturen, die in den Differenzspektren beobachtet wurden, sind vollständig reversibel, wenn das oxidierende und das reduzierende Referenzpotential an der Arbeitselektrode vertauscht werden. Dieses Verhalten weist darauf hin, daß die zugrundeliegenden Redox-Reaktionen des Enzyms an der Gold-Arbeitselektrode unter den verwendeten experimentellen Bedingungen ebenfalls vollständig reversibel sind. Dasselbe reversible spektrale Verhalten wurde auch für die Redox-Abhängigkeit der Soret- und der α -Bande der Häm *b* Gruppen im sichtbaren Spektralbereich festgestellt. Dies wiederum erlaubte die zuverlässige Bestimmung der Mittelpunktspotentiale der Häm *b* Gruppen der QFR bei verschiedenen pH-Werten. Die Analyse der FTIR-Differenzspektren im Bereich der spektralen Beiträge der Amid I Schwingungen weist auf eine strukturelle Umordnung des Polypeptidrückgrats infolge der elektrochemisch induzierten Redox-Reaktion hin.

- 2.) Die mit Hilfe der multikonformations-kontinuums-elektrostatischen (MCCE) Rechnungen simulierten Redox-Titrations an den Hoch- und Niedrigpotential-Hämen der QFR wiesen eine sehr gute Übereinstimmung mit den experimentell ermittelten Werten für die Häm *b* Mittelpunktpotentiale bei pH 7 auf. Die wesentlichen energetischen Beiträge, die mit Hilfe der theoretischen Rechnungen für die unterschiedlichen Mittelpunktpotentiale der beiden Häm *b* Gruppen bestimmt werden konnten, sind ein größerer Verlust an sogenannter „Born“-Energie (diese beschreibt den Verlust an Solvatationsenergie, wenn die relevante chemische Gruppe aus einer hydrophilen löslichen Umgebung in das hydrophobe Innere des Proteins übertragen wird) des proximalen Häms und eine stärkere Destabilisierung des oxidierten Zustands des proximalen Häms aufgrund von mehreren ionisierten Arg und Lys Aminosäureseitenketten. Die explizite Berücksichtigung von röntgenkristallographisch identifizierten Wassermolekülen hatte einen merklichen Effekt auf die absoluten Werte der rechnerisch bestimmten Mittelpunktpotentiale der beiden Häme, obwohl sich deren Differenz relativ gesehen kaum veränderte. Die Ergebnisse der elektrostatischen Rechnungen ließen eine eindeutige Zuordnung des Niedrigpotential-Häms zur distalen Position b_D und des Hochpotential-Häms zur proximalen Position b_P in der Struktur der QFR zu. Diese Zuordnung war mit experimentellen Methoden bisher nicht eindeutig möglich.
- 3.) Der aktuell diskutierte Mechanismus des gekoppelten Elektronen- und Protonentransfers in der QFR (die „E-Weg“-Hypothese) erfährt weitere Unterstützung durch die in dieser Arbeit gewonnenen Ergebnisse. Die Simulationen von intermediären Elektronentransferzuständen in Bezug auf die beiden Häm *b* Gruppen zeigen, daß der Protonierungszustand von Glu C180 von

der Oxidationsstufe der Häm-Gruppen abhängt, wie es im Rahmen der „E-Weg“-Hypothese vorgeschlagen wurde. Dieses Ergebnis liefert daher einen denkbaren Mechanismus für die Kopplung von transientem transmembranen Protonentransfer an die Elektronenübertragung über die Häm-Gruppen, da es eine Rolle von Glu C180 als essentielles Glied einer Protonentransferkette, und somit auch als ein regulatorisches Element des „E-Weges“, stützt. Zusätzlich deuten die Ergebnisse der simulierten Häm-Reduktion darauf hin, daß die Seitenkette von Glu C180 auch eine Konformationsänderung in Abhängigkeit des Redox-Zustandes der Häme erfährt. Die beiden wesentlichen Ergebnisse die Rolle des Aminosäurerestes Glu C180 betreffend, d.h. die Protonierungsänderung sowie die Reorientierung der Seitenkette, stehen in Übereinstimmung mit den Ergebnissen der elektrochemisch induzierten FTIR-Differenzspektroskopie. Von besonderem Interesse war der Spektralbereich oberhalb von 1710 Wellenzahlen (cm^{-1}), in dem die C=O Streckschwingungen von protonierten COOH Carboxylgruppen absorbieren, da diese Gruppen als Protonendonator bzw. -akzeptor agieren und somit an Protonentransferprozessen innerhalb des Proteins beteiligt sein können. Es war möglich, Signale solcher protonierten Carboxylgruppen zu beobachten, die eindeutig dem QFR-Enzym zuzuordnen waren. Diese Signale zeigen, daß die betroffenen Gruppen entweder ihren Protonierungsgrad ändern und/oder eine Umgebungsänderung im Verlauf der induzierten Redox-Reaktion erfahren. Diese Beobachtung wurde von der Tatsache gestützt, daß die entsprechenden FTIR-Differenzsignale sensitiv gegenüber einem Isotopenaustausch von Wasserstoff zu Deuterium ($^1\text{H}/^2\text{H}$) sind und in D_2O zu niedrigeren Wellenzahlen hin verschoben waren. Weiterhin konnte mit Hilfe von gerichteter Mutagenese gezeigt werden, daß der saure Aminosäurerest Glu C180, welcher sich in der transmembranen, hämhaltigen C-Untereinheit der QFR befindet, zum redox-abhängigen Signal der

protonierten Carboxylgruppen beiträgt. Die beobachtete Bande im FTIR-Doppeldifferenzspektrum, gebildet aus dem Wild-Typ der QFR und der Enzymvariante E180Q, kann als Protonierungsänderung von Glu C180 interpretiert werden, welche von einer Umgebungsänderung der entsprechenden C=O Schwingung überlagert wird. Dieses Ergebnis stellt eine weitere deutliche Untermauerung der „E-Weg“ Hypothese des gekoppelten transmembranen Elektronen- und Protonentransfers im Enzym QFR dar, welche besagt, daß Glu C180 ein essentieller Bestandteil eines transienten, redox-kontrollierten transmembranen Protonentransferweges ist.

- 4.) Als zweiter möglicher Bestandteil des vorgeschlagenen „E-Weges“ könnte das Ring C Propionat des distalen Häms in Frage kommen, welches in ungewöhnlicher Weise in allen modellierten Redox-Zuständen als vollständig protoniert berechnet wurde. Dieses Ergebnis deutet darauf hin, daß diesem Propionat eine mögliche Rolle als transienten Protonendonator bzw. -akzeptor im Rahmen des diskutierten „E-Weges“ zukommen könnte. Ähnlich wie für Glu C180 wurde auch in diesem Fall mit Hilfe der FTIR-Spektroskopie an einer Variante der QFR, in welcher speziell die Carboxylkohlenstoffatome der Hämpropionate mit dem Kohlenstoffisotop ^{13}C markiert waren, Ergebnisse gewonnen, die auf eine Beteiligung mindestens eines der beiden Propionate des distalen Häms b_D am vorhergesagten Protonentransfer hindeuten. Die beobachteten Signale werden vorläufig derart interpretiert, daß das Ring C Propionat des Häms b_D eine redox-gekoppelte Protonierungsänderung erfährt, welche möglicherweise von einer Umgebungsänderung des selben Propionats überlagert wird.

- 5.) Auch der Nachweis eines ausgeprägten Redox-Bohr Effektes für beide Hämgruppen der QFR steht im Einklang mit der vorgeschlagenen „E-Weg“ Hypothese, da dieser Effekt einen möglichen und gut studierten Mechanismus darstellt, wie Protonentransfer an Änderungen der Oxidationsstufe von Häm-Gruppen gekoppelt sein kann. Vergleicht man den beobachteten Effekt im QFR Wild-Typ und in der Variante E180Q und stellt dieses Ergebnis in Zusammenhang mit den anderen Resultaten der FTIR-Spektroskopie und der elektrostatischen Rechnungen, so kommt man zu dem Schluß, daß das Ring C Propionat des distalen Häms die dominierende protolytische Gruppe für die pH-Abhängigkeit des Mittelpunktspotentials von Häm b_D zu sein scheint, und daß Glu C180 die entsprechende Gruppe in bezug auf das Häm b_P darstellt. Der genaue Ursprung des (im Vergleich zum Wild-Typ sehr deutlich geänderten) Redox-Bohr Effekts für das Häm b_P in der Enzymvariante E180Q konnte nicht eindeutig identifiziert werden. Die Beobachtung dieses Redox-Bohr Effekts in der Variante deutet auf den Einfluß anderer protolytischer Gruppen hin, welche mit Häm b_P in Wechselwirkung stehen, und die möglicherweise ebenfalls notwendig sein könnten für einen funktionellen „E-Weg“.

SUMMARY

The enzyme quinol:fumarate reductase (QFR) from the anaerobic ϵ -proteobacterium *Wolinella succinogenes* is part of the anaerobic respiratory system of this organism. It couples the reduction of fumarate to succinate to the oxidation of menaquinol to menaquinone. *W. succinogenes* uses fumarate as terminal electron acceptor and can use various substrates (e.g., formate or molecular hydrogen) as electron donors. The concerted catalytic substrate turnover of either a hydrogenase or a formate dehydrogenase in conjunction with QFR contributes to the generation of an electrochemical potential gradient across the bacterial plasma membrane, which is used for the phosphorylation of ADP with inorganic phosphate, P_i , to ATP. In addition to an FAD (in subunit A) and three iron-sulfur clusters (in subunit B), QFR binds a low- and a high-potential heme *b* group in its transmembrane subunit C, as was ultimately shown in the crystal structure at 2.2 Å resolution (Lancaster *et al.*, 1999, *Nature* 402, 377–385). Both hemes are part of the electron transport chain between the two catalytic sites of this redox enzyme. The midpoint potentials of the hemes are well established but their assignment to the distal and proximal positions in the structure had not yet been determined.

Furthermore, QFR from *W. succinogenes* has been proposed to exhibit a novel coupling mechanism of transmembrane electron and proton transfer, which has been described in the so-called “E-pathway” hypothesis (Lancaster, 2002, *Biochim. Biophys. Acta* 1565, 215–231).

The aim of this project was to characterize the relationship between structure and function of QFR and to investigate the details of the proposed coupling mechanism (“E-pathway”) with the help of computer-based electrostatic calculations on the QFR wild-type

(WT) coordinates, and electrochemically induced FTIR and VIS difference spectroscopy on the QFR WT and available variant enzymes (in particular enzyme variant E180Q, in which the glutamic acid at position C180 has been replaced by a glutamine).

- 1.) It was demonstrated in this study that the diheme-containing QFR exhibits stable and reproducible electrochemically induced FTIR difference bands in the mid-infrared range from 1800 cm^{-1} to 1000 cm^{-1} that reflect transitions from the reduced to the oxidized state of the enzyme. The spectral features that were observed in the FTIR difference spectra are fully reversible when changing from a reductive to an oxidative reference potential at the working electrode and vice versa. This indicates that the underlying redox reactions of the enzyme at the gold grid working electrode are also fully reversible under the applied experimental conditions. The same reversible spectral redox behavior in the visible range could also be ascertained for the Soret- and α -band of the two heme *b* groups of QFR. This behavior allowed to reliably determine the heme *b* midpoint potentials of QFR at various pH values. Analysis of the FTIR difference spectra in the amide I range yields evidence for structural reorganizations of the polypeptide backbone upon the electrochemically induced redox reaction.
- 2.) The redox titrations of the high- and low-potential heme *b* of QFR as simulated by multiconformation continuum electrostatics (MCCE) calculations showed a very high level of agreement with respect to the experimentally observed midpoint potentials of the heme *b* groups at pH 7. As determined with the help of the theoretical calculations, prominent features governing the differences in redox potential between the two hemes are the higher loss of reaction field energy for the proximal heme and the stronger destabilization of the oxidized form of the proximal

heme due to several buried and ionized Arg and Lys residues. The explicit incorporation of crystallographically identified water molecules in the calculations had a noticeable effect on the absolute values of the determined midpoint potentials, although the relative difference of the two obtained midpoints did not change significantly. The results of the electrostatic calculations clearly showed that the low-potential heme corresponds to the distal position b_D in the structure, and that the high-potential heme is identical to the proximal heme b_P . This assignment could previously not be achieved unequivocally with experimental methods.

- 3.) In addition, the currently discussed mechanism of coupled electron and proton transfer in the QFR of *W. succinogenes* (i.e., the “E-pathway” hypothesis) is further supported by the results of this study. The simulations of intermediate states of electron transfer via the heme b groups show that the protonation state of the key amino acid residue Glu C180 depends on the redox states of the heme groups as suggested in the “E-pathway” hypothesis. This result yields a possible mechanism for the coupling of transient transmembrane proton transfer via Glu C180 to the electron transfer via the heme b groups, since Glu C180 could be part of a “proton wire” and its redox-dependent protonation state could serve as the regulatory element of the “E-pathway”. Furthermore, the results of simulated heme reduction indicate that the side chain of Glu C180 also changes its conformation with respect to the redox state of the hemes. Both major results concerning the role of Glu C180, the change of protonation as well as the reorientation of the side chain upon reduction of the heme groups, are consistent with the results from electrochemically induced FTIR difference spectroscopy: Of particular interest was the spectral range above 1710 cm^{-1} , where C=O stretching vibrations of protonated COOH carboxyl groups absorb, because those groups can act as proton donors, respectively acceptors, and can be

involved in intra-protein proton transfer reactions. It was possible to observe signals of such protonated carboxyl groups originating from QFR enzyme, which either change their protonation state and/or experience an environmental change in the course of the induced redox reaction. This finding was supported by the fact that the relevant FTIR difference signals are sensitive to an isotopic hydrogen/deuterium ($^1\text{H}/^2\text{H}$) exchange via the buffer solution, since they were shifted towards lower wavenumbers in D_2O . Furthermore, it could be shown with the help of site-directed mutagenesis that the acidic residue Glu C180, which is located in the membrane-spanning, diheme-containing subunit C of QFR, is contributing to the redox dependent signal of protonated carboxyl groups. The observed residual signal in the FTIR double-difference spectrum of QFR wild-type and enzyme variant E180Q (Glu C180 has been replaced with a Gln residue) could be interpreted as a protonation/deprotonation event that is superimposed by an environmental effect on the specific C=O vibration. This result strongly supports the proposed “E-pathway” of coupled transmembrane electron and proton transfer in the QFR enzyme, which states that residue Glu C180 is an essential constituent of a transient redox-controlled transmembrane proton transfer pathway.

- 4.) As a second possible constituent of the suggested “E-pathway”, the ring C propionate of the distal heme was found to be unusually fully protonated in all simulated redox states, indicating a possible role as a transient proton donor/acceptor in the “E-pathway”. Similarly to Glu C180, experimental evidence from FTIR difference spectroscopy on a modified QFR with ^{13}C -labeled heme propionates was obtained, which indicates an involvement of at least one of the two propionates of heme b_D in proton transfer. The observed signals can tentatively be interpreted as a redox-coupled (de)protonation of the ring C propionate of b_D , which is possibly

superimposed by a conformational or environmental change of the specific propionate.

- 5.) Also the observation of a strong redox Bohr effect for both heme b groups in QFR is in line with the proposed “E-pathway” hypothesis, as this effect yields a possible and well-established mechanism for the coupling of proton transfer and redox changes of the heme groups. The comparison of the observed effect in QFR WT and E180Q together with the results from FTIR spectroscopy and MCCE calculation indicate that the ring C propionate of the distal heme is dominating the pH-dependence of the midpoint potential of b_D , and that the corresponding group for b_P is Glu C180. The origin of the redox Bohr effect for b_P in the enzyme variant E180Q (which is dramatically changed with respect to the WT) could not be identified unequivocally, but the observation of this redox Bohr effect in the variant implies the presence of other protolytic groups, which interact with heme b_P and which may be necessary for a functional “E-pathway”.

CONTENTS

| | |
|---|-----------|
| Veröffentlichungen..... | i |
| Zusammenfassung..... | iii |
| Summary..... | ix |
| List of Figures..... | xix |
| List of Tables..... | xxi |
| 1 Introduction..... | 1 |
| 1.1 The “Chemiosmotic Hypothesis”..... | 1 |
| 1.2 The Redox Bohr Effect..... | 3 |
| 1.2.1 The Nernst Equation and the theory of the redox Bohr effect..... | 3 |
| 1.3 Anaerobic Fumarate Respiration in <i>Wolinella succinogenes</i> | 6 |
| 1.4 Classification of SQORs..... | 7 |
| 1.5 The Structure and Function of the Quinol:Fumarate Reductase from <i>W. succinogenes</i> | 8 |
| 1.5.1 Coupled transmembrane electron and proton transfer in QFR: The “E-pathway” hypothesis..... | 9 |
| 1.6 Heme Propionate ¹³ C-Labeling of QFR WT for FTIR Spectroscopy..... | 12 |
| 1.7 Goals of this Work and Motivation of the Employed Methods..... | 14 |
| 2 Materials and Methods..... | 17 |
| 2.1 Materials..... | 17 |
| 2.1.1 List of mediators..... | 17 |
| 2.1.2 List of chemicals..... | 18 |
| 2.1.3 List of laboratory equipment..... | 18 |
| 2.2 Electrostatic Calculations..... | 19 |
| 2.2.1 The “Multiconformation Continuum Electrostatics” method..... | 19 |
| 2.2.1.1 Description of the individual steps of the complete MCCE calculation.. | 20 |
| 2.2.2 Structural model of QFR and coordinates..... | 23 |
| 2.2.3 Simulated redox potential titrations..... | 25 |
| 2.2.4 Simulated heme reduction..... | 25 |
| 2.3 Electrochemically Induced VIS and FTIR Difference Spectroscopy..... | 26 |
| 2.3.1 Electrochemistry..... | 26 |
| 2.3.1.1 The electrochemical cell..... | 27 |
| 2.3.1.2 Surface modification of the gold grid working electrode..... | 28 |
| 2.3.1.3 Redox mediators..... | 29 |
| 2.3.2 Infrared spectroscopy..... | 29 |
| 2.3.2.1 Fourier transform infrared spectroscopy..... | 30 |
| 2.3.2.2 FTIR spectroscopy in the context of coupled ET and PT in QFR..... | 32 |
| 2.3.2.3 Experimental details of FTIR spectroscopy of QFR..... | 33 |

| | | |
|----------|---|----|
| 2.3.3 | VIS spectroscopy and heme redox titrations of QFR..... | 34 |
| 2.3.4 | Sample preparation..... | 35 |
| 2.3.5 | Heme propionate ¹³ C-labeling..... | 36 |
| 3 | Results | 37 |
| 3.1 | Electrostatic Calculations | 37 |
| 3.1.1 | Electrostatic interactions of the hemes and their propionates with the protein | 37 |
| 3.1.2 | Protonation states of residues interacting with the hemes..... | 41 |
| 3.1.3 | Comparison of simulated and experimental E_h titrations and heme assignment | 42 |
| 3.1.4 | Nonstandard protonation states of residues in the QFR model at pH 7 | 46 |
| 3.1.5 | Simulated heme reduction and its effect on conformer occupancy | 46 |
| 3.1.6 | Simulated pH titrations of Glu C180 as a function of the heme redox states .. | 50 |
| 3.1.7 | Conformational change of Glu C180 mediated by waters W11 and W33..... | 52 |
| 3.2 | FTIR and VIS Spectroscopy | 57 |
| 3.2.1 | FTIR on QFR WT and enzyme variants | 57 |
| 3.2.1.1 | Electrochemically induced IR and VIS difference spectra | 57 |
| 3.2.1.2 | Contributions of the amide I band and secondary structure elements..... | 60 |
| 3.2.1.3 | Contributions of the amide II and III bands | 61 |
| 3.2.1.4 | Effects of ¹ H/ ² H isotope exchange | 61 |
| 3.2.1.5 | Contributions of the potassium phosphate buffer | 63 |
| 3.2.1.6 | Contributions of the FAD/FADH ₂ couple..... | 63 |
| 3.2.1.7 | Contributions of the iron-sulfur clusters | 65 |
| 3.2.1.8 | Contributions of the heme <i>b</i> groups and their propionates | 65 |
| 3.2.1.9 | Contributions of quinones | 66 |
| 3.2.1.10 | Contributions of the amino acid residues..... | 67 |
| 3.2.1.11 | Table with tentative FTIR band assignments of QFR enzyme | 69 |
| 3.2.1.12 | Influence of amino acid exchanges on FTIR difference signals in the range of $\nu(\text{COOH})$ modes | 72 |
| 3.2.1.13 | The pH dependency of $\nu(\text{COOH})$ modes..... | 76 |
| 3.2.2 | FTIR difference spectroscopy on QFR with ¹³ C-labeled heme propionates.... | 77 |
| 3.2.2.1 | Midpoint potentials of labeled hemes at pH 7..... | 77 |
| 3.2.2.2 | Reversible FTIR difference spectra of the “full potential” step..... | 78 |
| 3.2.2.3 | Separation of redox-induced IR signals from hemes b_D and b_P | 79 |
| 3.2.2.4 | Tentative signals of protonated heme propionate(s) of heme b_D | 82 |
| 3.2.2.5 | “Unlabeled-minus- ¹³ C-labeled” QFR FTIR double-difference spectra... 84 | |
| 3.2.3 | The pH-dependence of QFR WT and E180Q heme <i>b</i> midpoint potentials: The redox Bohr effect..... | 85 |
| 4 | Discussion..... | 89 |
| 4.1 | Electrostatics | 89 |
| 4.1.1 | Simulated heme E_h titrations | 89 |
| 4.1.2 | Assignment of the low- and high-potential heme to b_D and b_P | 91 |
| 4.1.3 | Simulated heme reduction and affected ionization states as a function of pH. 93 | |

| | | |
|---------|--|-----|
| 4.1.4 | Reorientation of the Glu C180 side chain upon heme reduction | 94 |
| 4.1.5 | Protonation state of the ring C propionate of heme b_D | 95 |
| 4.1.6 | Implications for the E-pathway hypothesis | 96 |
| 4.2 | Spectroscopy | 97 |
| 4.2.1 | Comparison of QFR WT and variant FTIR difference spectra, and redox-induced conformational changes of the enzyme | 97 |
| 4.2.2 | Effects of $^1\text{H}/^2\text{H}$ isotope exchange in QFR WT and implications for conformational changes..... | 98 |
| 4.2.3 | Analysis of the $\nu(\text{COOH})$ signals in QFR WT and variants | 99 |
| 4.2.4 | The pH-dependence of the observed $\nu(\text{COOH})$ signals in QFR WT..... | 100 |
| 4.2.5 | Hydrogen bonding strength of the observed $\nu(\text{COOH})$ signals..... | 101 |
| 4.2.6 | Analysis of QFR WT and variant double-difference spectra..... | 101 |
| 4.2.7 | FTIR difference spectroscopy on QFR with ^{13}C -labeled heme propionates.. | 103 |
| 4.2.7.1 | Tentative vibrations of protonated heme propionates..... | 103 |
| 4.2.7.2 | Tentative anti- and symmetric vibrations of deprotonated heme propionates | 104 |
| 4.2.7.3 | Differences between the full and partial potential step for b_D | 105 |
| 4.2.8 | Analysis of the observed redox Bohr effect | 106 |
| 4.2.8.1 | Redox Bohr effect in WT QFR and the role of the ring C propionate of heme b_D | 106 |
| 4.2.8.2 | Redox Bohr effect in variant E180Q and the role of Glu C180 in the WT | 107 |
| 4.2.8.3 | Consequences of the observed redox Bohr effect on heme b_P in QFR variant E180Q for the “E-pathway” | 109 |
| 4.3 | Conclusions | 110 |
| 5 | References | 113 |
| 6 | APPENDIX | 129 |
| 6.1 | Electrostatics | 129 |
| 6.1.1 | Non-uniform and uniform partial charges for QFR iron-sulfur clusters..... | 129 |
| 6.1.2 | Influence of FeS-cluster redox state on simulated heme redox titrations | 131 |
| 6.1.3 | Results of simulated heme reduction in QFR based on model X..... | 132 |
| 6.2 | Spectroscopy | 134 |
| 6.2.1 | Data fitting of (VIS) heme redox titrations with the Nernst equation..... | 134 |
| 6.2.2 | Preparation and calibration of the Ag/AgCl reference electrode | 135 |
| 6.2.3 | KP _i -buffer spectra..... | 136 |
| 6.2.4 | QFR WT IR absorbance spectra..... | 137 |
| 6.2.5 | Hydrogen/deuterium isotope exchange bands in the IR spectrum..... | 138 |
| 6.2.6 | Electrochemically induced FTIR difference spectra of QFR enzyme variants E180Q and E66Q in D ₂ O buffer | 139 |
| 6.2.7 | Baseline instabilities during FTIR data acquisition | 140 |
| 6.2.8 | Disturbing effect of water vapor in the sample compartment on FTIR spectra | 141 |
| 6.2.9 | Heme redox titrations of QFR WT with ^{13}C -labeled heme propionates..... | 142 |

| | |
|---|-----|
| 6.2.10 Identification of a spectral artifact at 1292 cm^{-1} due to the mediators..... | 143 |
| Glossary, Interconversion of Energy Units, and Abbreviations | 145 |
| Danksagung | 147 |
| Curriculum Vitae | 149 |

LIST OF FIGURES

| | |
|--|----|
| Figure 1.1: Scheme of the mitochondrial aerobic respiratory chain. | 2 |
| Figure 1.2: Graphical scheme of the redox Bohr effect. | 5 |
| Figure 1.3: Scheme of anaerobic respiration in <i>Wolinella succinogenes</i> | 7 |
| Figure 1.4: Classification scheme of SQORs (types A to E). | 8 |
| Figure 1.5: Three-dimensional structure of the <i>W. succinogenes</i> QFR dimer. | 9 |
| Figure 1.6: “E-pathway” hypothesis of coupled transmembrane ET and PT in QFR. | 11 |
| Figure 1.7: Schematic view of the three relevant heme propionate vibrations. | 13 |
| Figure 1.8: Chemical structure of the heme <i>b</i> group. | 14 |
| Figure 2.1: Electrostatic model of intermediate heme redox states in enzymatic electron transfer of QFR. | 26 |
| Figure 2.2: Scheme of the “three-electrode” array in the electrochemical cell. | 27 |
| Figure 2.3: A schematic view of the spectroelectrochemical cell. | 28 |
| Figure 2.4: Basic scheme of a Michelson interferometer. | 31 |
| Figure 3.1: Simulated heme redox titrations. | 42 |
| Figure 3.2: Ionized bases interacting with heme <i>b</i> groups of QFR. | 44 |
| Figure 3.3: Graphical representation of significant occupancy changes. | 48 |
| Figure 3.4: Change of the total charge in the course of simulated heme reduction. | 49 |
| Figure 3.5: The pK _a of Glu C180 depends on the heme redox states. | 51 |
| Figure 3.6: Side-chain orientation of Glu C180 in simulated heme reduction. | 53 |
| Figure 3.7: Conformational change of Glu C180. | 54 |
| Figure 3.8: Electrochemically induced FTIR difference spectra in the mid-IR range. | 59 |
| Figure 3.9: Electrochemically induced FTIR difference spectra of QFR WT in H ₂ O and D ₂ O. | 62 |
| Figure 3.10: FTIR difference spectra of QFR WT and variants above 1720 cm ⁻¹ | 73 |
| Figure 3.11: FTIR double-difference spectra of QFR WT and enzyme variants. | 75 |
| Figure 3.12: The pH-dependence of the FTIR difference spectra above 1715 cm ⁻¹ | 77 |
| Figure 3.13: Electrochemically induced FTIR difference spectra of unlabeled and ¹³ C-labeled QFR. | 78 |
| Figure 3.14: Electrochemically induced FTIR difference spectra of unlabeled QFR at pH 7 with intermediate step. | 80 |
| Figure 3.15: Electrochemically induced FTIR difference spectra of ¹³ C-labeled QFR at pH 7 with intermediate step. | 81 |
| Figure 3.16: Detail of FTIR difference spectra of unlabeled and ¹³ C-labeled QFR at pH 7. | 83 |
| Figure 3.17: FTIR double-difference spectra of “unlabeled-minus- ¹³ C-labeled” QFR at pH 7. | 84 |
| Figure 3.18: The pH-dependence of the heme <i>b</i> midpoint potentials of <i>W. succinogenes</i> QFR WT and E180Q. | 86 |

| | |
|---|-----|
| Figure 4.1: Oxidation-reduction potentials of the constituents of the ET chain of <i>W. succinogenes</i> QFR..... | 92 |
| Figure 6.1: Simulated heme b_D and b_P redox titrations of QFR with 1 or 2 electrons on the system of FeS clusters..... | 131 |
| Figure 6.2: Analogous to Figure 3.4, but based on model X (no water molecules)..... | 132 |
| Figure 6.3: Analogous to Figure 3.5, but based on model X (no water molecules)..... | 132 |
| Figure 6.4: Analogous to Figure 3.7, but based on model X (no water molecules)..... | 133 |
| Figure 6.5: Calibration and preparation of the Ag/AgCl reference electrode..... | 135 |
| Figure 6.6: IR absorbance spectra of KP_i -buffer in H_2O and D_2O | 136 |
| Figure 6.7: Electrochemically induced FTIR difference spectra of KP_i -buffer and mediators at pH 7..... | 136 |
| Figure 6.8: IR absorbance spectra of QFR WT in H_2O and D_2O | 137 |
| Figure 6.9: Characteristic $^1H/^2H$ isotope exchange bands in QFR WT FTIR difference spectra..... | 138 |
| Figure 6.10: Electrochemically induced FTIR difference spectra of QFR E180Q in D_2O at pD 7.4..... | 139 |
| Figure 6.11: Electrochemically induced FTIR difference spectra of QFR E66Q in D_2O at pD 7.4..... | 140 |
| Figure 6.12: Baseline instabilities and technical difficulties in FTIR difference spectroscopy..... | 140 |
| Figure 6.13: The disturbing effect of water vapor in the sample compartment of the FTIR spectrophotometer..... | 141 |
| Figure 6.14: Heme redox titration curves of QFR WT enzyme with ^{13}C -labeled heme propionates at pH 7..... | 142 |
| Figure 6.15: Identification of a mediator-related difference signal at 1292 cm^{-1} | 143 |

LIST OF TABLES

| | |
|---|----|
| Table 2.1: List of mediators for electrochemical measurements | 17 |
| Table 2.2: List of chemicals | 18 |
| Table 2.3: List of laboratory equipment..... | 18 |
| Table 3.1: The electrostatic interaction energies of model W of QFR. | 38 |
| Table 3.2: Significant occupancy changes between the different modeled heme redox states. | 47 |
| Table 3.3: Summary of (tentative) IR-band assignments of <i>Wolinella succinogenes</i> QFR..... | 70 |
| Table 3.4: QFR WT and E180Q heme <i>b</i> midpoint potentials at various pH values. | 85 |
| Table 3.5: Summary of the redox Bohr-parameters, E_{m0} and $E_{m(\text{bases})}$, and pK_{red} and pK_{ox} | 87 |

1 INTRODUCTION

1.1 The “Chemiosmotic Hypothesis”

The process of adenosine triphosphate (ATP) synthesis from adenosine diphosphate (ADP) and inorganic phosphate (P_i) is of central relevance to the entire field of bioenergetics, as ATP is the ubiquitous energy carrier of all known living cells. ATP synthesis is the central function of aerobic and anaerobic respiration as well as photosynthesis and takes place, for instance, in the inner mitochondrial membrane (oxidative phosphorylation), in the bacterial plasma membrane, and in the thylakoid membrane of chloroplasts (photosynthetic phosphorylation), respectively. A gradient of the electrochemical potential $\tilde{\mu}$ of sodium ions (Na^+) or protons (H^+) can serve as an energy source for active transport of molecules across biological membranes, but in bioenergetics, the main use of a gradient of $\tilde{\mu}_{H^+}$ is the biological synthesis of ATP out of ADP and P_i .

The “chemiosmotic hypothesis”, which was put forward by Peter Mitchell, states that redox energy (the free energy of electron transport) is intermediately stored in the form of a difference in the electrochemical proton potential $\tilde{\mu}_{H^+}$ across the inner mitochondrial membrane (Mitchell, 1961 and 1979). Consequently, Mitchell suggested that this difference $\Delta\tilde{\mu}_{H^+}$ could be the driving force for ATP synthesis.

For example, in the beginning of the electron transport chain in mitochondria, oxidation of nutrients provides reduction equivalents NADH and $FADH_2$, from which electrons are transferred, via the mitochondrial electron transport chain, ultimately to reduce oxygen to water (Saraste, 1999).

The energy released during these electron transfer reactions, as catalyzed by a series of membrane-bound protein complexes (see Figure 1.1), is transiently stored in the form of an electrochemical proton potential across the membrane. These membrane protein complexes differ considerably in composition and function in the systems mentioned above.

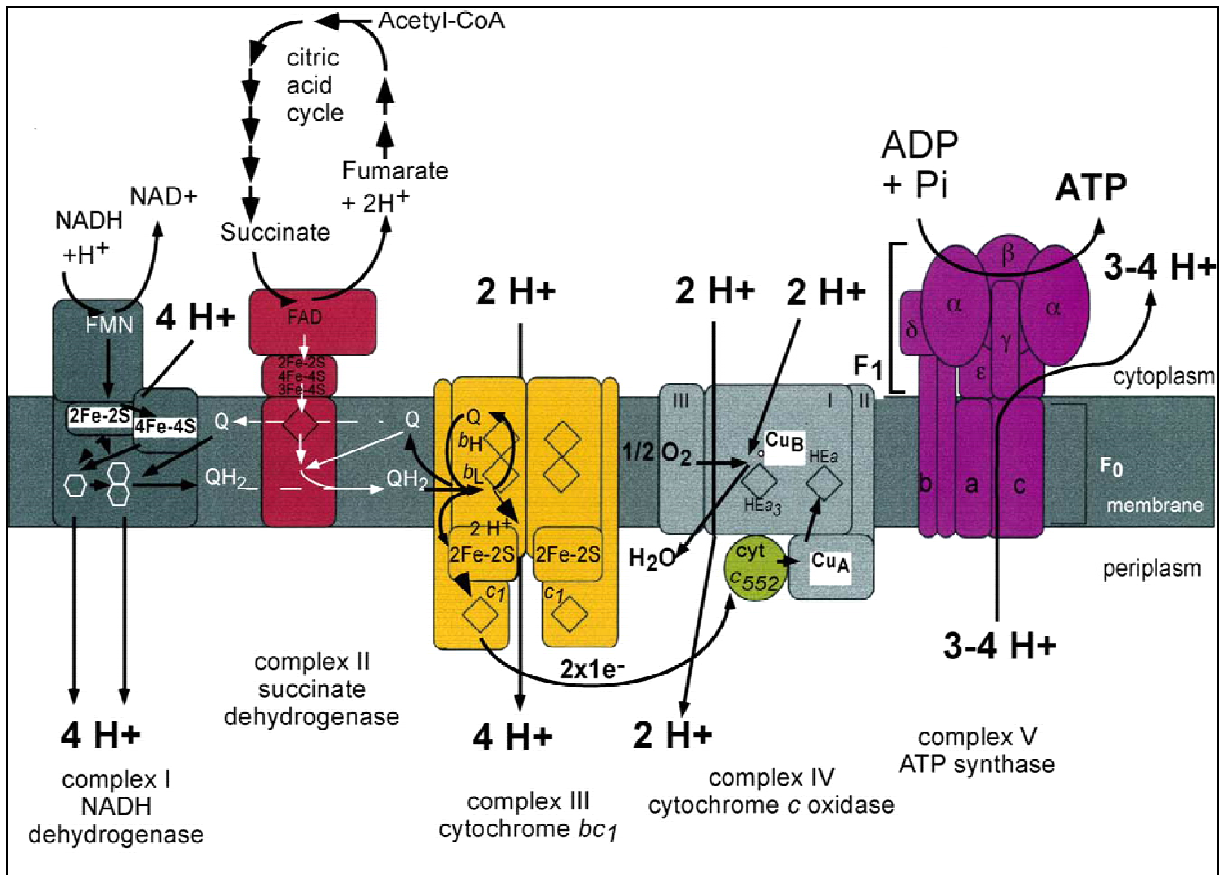


Figure 1.1: Scheme of the mitochondrial aerobic respiratory chain.

The redox activities of the respiratory complexes I, III and IV are responsible for the generation of the proton gradient, as indicated. The established gradient in electrochemical potential is then used by the ATP synthase to drive ATP synthesis. The figure was copied from ref. (Lancaster, 2002b).

The difference in electrochemical potential $\Delta\tilde{\mu}_{\text{H}^+}$ upon transporting one proton across the inner mitochondrial membrane has a chemical ($\Delta\text{pH} = \text{pH}_{\text{in}} - \text{pH}_{\text{out}}$) as well as an electrical component since the proton is a positively charged ion (which is then associated with a difference in electrical potential, $\Delta\varphi = \varphi_{\text{in}} - \varphi_{\text{out}}$); and thus $\Delta\tilde{\mu}_{\text{H}^+}$ equals:

$$\Delta\tilde{\mu}_{\text{H}^+} = RT \ln \frac{[\text{H}^+]_{\text{in}}}{[\text{H}^+]_{\text{out}}} + F(\varphi_{\text{in}} - \varphi_{\text{out}}) = -2.3 \cdot RT \cdot \Delta\text{pH} + F\Delta\varphi, \quad (1)$$

where R is the universal gas constant, F is Faraday's constant, and $[\text{H}^+]$ is the proton concentration, respectively proton activity, in- and outside the membrane boundary. With the definition of the proton potential $\Delta p \equiv \Delta\tilde{\mu}_{\text{H}^+} / F$, eq. (1) is written as

$$\Delta p \equiv \frac{\Delta\tilde{\mu}_{\text{H}^+}}{F} = -2.3 \frac{RT}{F} \Delta\text{pH} + \Delta\varphi \approx -(59\text{mV})\Delta\text{pH} + \Delta\varphi. \quad (2)$$

The transfer of a proton against the gradient is an endergonic process, and consequently the opposite process, which is equal to a discharge of the gradient, is exergonic.

This free energy of the discharge is used by ATP synthase to power the phosphorylation of ADP to ATP. More detailed descriptions of the chemiosmotic hypothesis are found for instance in refs. (Adam *et al.*, 1995; and Voet *et al.*, 1999).

1.2 The Redox Bohr Effect

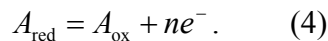
The so-called “Bohr effect” originally described the effect of protons on the binding of oxygen to hemoglobin and how it promotes the release of oxygen from hemoglobin in body tissues, as well as the release of CO₂ from the blood in the lungs (Bohr *et al.*, 1904). Thus, the effect is associated with the coupling of redox reactions and protonation changes, respectively pK_a changes, of amino acid residues or heme propionates and is usually referred to as “redox Bohr effect” in redox-enzymes (see also Figure 1.2). Several currently investigated systems are reviewed for instance in (Mills & Ferguson-Miller, 2003).

1.2.1 The Nernst Equation and the theory of the redox Bohr effect

A comprehensive derivation of the pH-dependent Nernst equation, which comprises proton dissociation constants for the reduced and oxidized states, is given in ref. (Dutton, 1978). A brief outline of this derivation shall be given here. The standard Nernst equation (derived by W. H. Nernst in 1889)

$$E_h = E_{mx} + \frac{RT}{nF} \ln \frac{[A_{ox}]}{[A_{red}]} \quad (3)$$

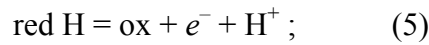
describes the “half-cell” reaction



A_{red} is the reduced species and A_{ox} the oxidized form, n is the number of transferred electrons e^{-} . $[A_{red}]$, for example, corresponds to the concentration, respectively activity, of the reduced species. E_h is the potential of the half cell, E_{mx} corresponds to the midpoint potential of the redox reaction where x indicates the ambient pH, R is the universal gas constant (8.3145 J·K⁻¹·mol⁻¹), F is the Faraday constant (96,485.3415 C·mol⁻¹), and T is the absolute temperature (K). The potentials refer to the standard hydrogen electrode SHE’ at pH 7.

Free electrons do not occur in redox reactions of the kind described above. Upon oxidation of the first compound, the electrons are chemically bound to the reduced reaction partner, which corresponds to the second half-cell reaction $B_{\text{ox}} + ne^- = B_{\text{red}}$. The midpoint potential E_m is the potential at which the concentrations/activities of the reduced and oxidized species of the half cell are equal. More positive values of E_m indicate a stronger oxidizing effect of the corresponding redox compound. Electrons always follow more positive potentials; and these differences in redox potential are the ultimate driving force for electron transfer in the membrane-bound respiratory systems, and thus also for ATP synthesis.

The pH-dependence is incorporated by considering a net release and binding of protons (H^+) during a simple $n = 1$ redox reaction:



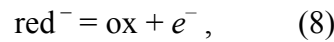
and the potential of the half cell (at $\sim 29^\circ \text{C}$, and with: $\ln \approx 2.3 \log_{10}$) can be described as:

$$E_h = E_{m0} + 0.06 \log \frac{[\text{ox}][\text{H}^+]}{[\text{red H}]}, \quad (6)$$

which yields

$$E_h = E_{m0} + 0.06 \log \frac{[\text{ox}]}{[\text{red H}]} - 0.06 \text{pH}. \quad (7)$$

This linear pH-dependence (7) is valid at ambient pH values above a $\text{p}K_{\text{ox}}$ for the oxidized form (i.e., $\text{ox} + \text{H} \rightleftharpoons \text{ox}$) and below a $\text{p}K_{\text{red}}$ for the reduced form (i.e., $\text{red H} \rightleftharpoons \text{red}^-$). Outside of this range, the redox reaction (i.e., E_m) will lose its pH-dependence since there will be no net exchange of H^+ anymore. At pH values well above $\text{p}K_{\text{red}}$ the redox entity is always deprotonated and the reaction can be written as:



and at pH values well below $\text{p}K_{\text{ox}}$ the redox reaction always occurs under protonated conditions:



Hence, the following dissociation constants K_{ox} and K_{red} can be defined based on (8) and (9):

$$K_{\text{ox}} = \frac{[\text{ox}][\text{H}^+]}{[\text{ox} + \text{H}]}, \quad K_{\text{red}} = \frac{[\text{red}^-][\text{H}^+]}{[\text{red H}]}. \quad (10a), (10b)$$

Considering the entire redox reaction, the midpoint E_{mx} is measured at the potential E_h where the *total* oxidized species equals the *total* reduced species of the redox couple:

$$E_h = E_{mx} + 0.06 \log \frac{[\text{ox}] + [\text{ox}^+ \text{H}]}{[\text{red}^-] + [\text{red H}]} \quad (11)$$

With the above defined dissociation constants (10a) and (10b), and E_{m0} as point of reference (corresponding to (9), $[\text{H}^+] \gg K_{\text{ox}}$ and K_{red}) the final expression for E_{mx} is obtained:

$$E_{mx} = E_{m0} - 0.06 \log \frac{(1 + K_{\text{ox}}/[\text{H}^+])}{(1 + K_{\text{red}}/[\text{H}^+])} \quad (12)$$

If $E_{m(\text{bases})}$ is chosen instead of E_{m0} as point of reference (corresponding to (8), $[\text{H}^+] \ll K_{\text{ox}}$ and K_{red}), an expression analogous to (12) can be derived.

Equation (12) will be used to fit the experimental data concerning the redox Bohr effect and hence to obtain the parameters E_{m0} , and $\text{p}K_{\text{ox}}$ and $\text{p}K_{\text{red}}$.

Figure 1.2 shows a graphical scheme of the different chemical reactions involved in the redox Bohr effect and how the release and uptake of protons and electrons, respectively, is coupled.

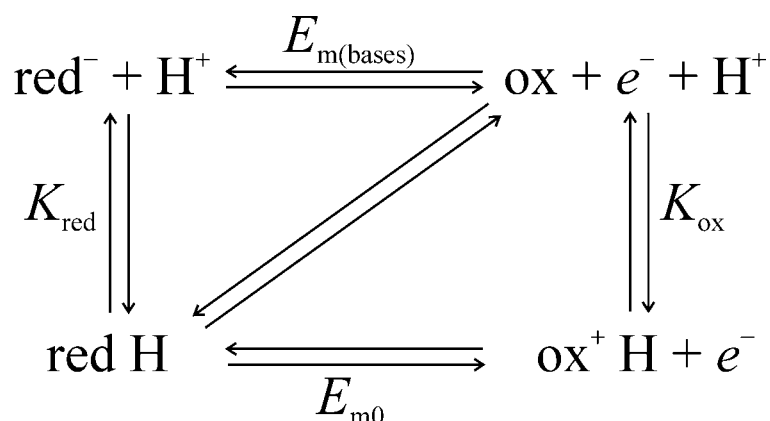


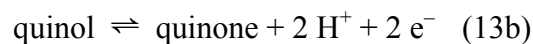
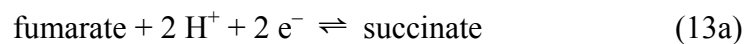
Figure 1.2: Graphical scheme of the redox Bohr effect.

Vertical arrows indicate reactions, which involve proton exchange in either the fully reduced or oxidized state; horizontal arrows indicate pure redox reactions of the protonated (9) or deprotonated (8) species. The diagonal line indicates the coupled reaction (5). A third dimension has to be considered in this scheme if conformational changes are involved in the process.

1.3 Anaerobic Fumarate Respiration in *Wolinella succinogenes*

Respiratory systems of aerobic and anaerobic bacteria can serve as model systems for the understanding of aerobic respiration in mitochondria, since it is commonly accepted that mitochondria evolved from bacterial ancestors. Furthermore, the bacterial systems are favorable with respect to protein production, and the creation of mutants and the subsequent production of enzyme variants are much easier in bacteria than for mitochondrial systems.

The enzyme quinol:fumarate reductase (QFR) of the anaerobic ϵ -proteobacterium *Wolinella succinogenes* is a diheme-containing membrane protein complex, which couples the two-electron reduction of fumarate to succinate (reaction 13a) to the two-electron oxidation of quinol to quinone (reaction 13b). QFR is also able to catalyze the reverse reaction *in vitro* (Lemma *et al.*, 1991) and can thus also operate as a succinate:quinone reductase (SQR).



The *W. succinogenes* QFR is involved in anaerobic respiration (see Figure 1.3) with various electron donor substrates, such as NADH, formate or molecular hydrogen, and with fumarate as the terminal electron acceptor (Kröger, 1978; and Lancaster, 2004). The free energy associated with the electron transfer reactions is responsible for the generation of a transmembrane electrochemical proton potential via the concerted enzymatic activities of QFR, the formate dehydrogenase, and the hydrogenase. The proton potential in turn is driving the ATP synthase, which phosphorylates ADP to yield high-energetic ATP. Hence, the electron transfer is coupled to ADP phosphorylation by the ATP synthase.

Figure 1.3 shows the anaerobic bacterial analogue to the mitochondrial system shown above in Figure 1.1:

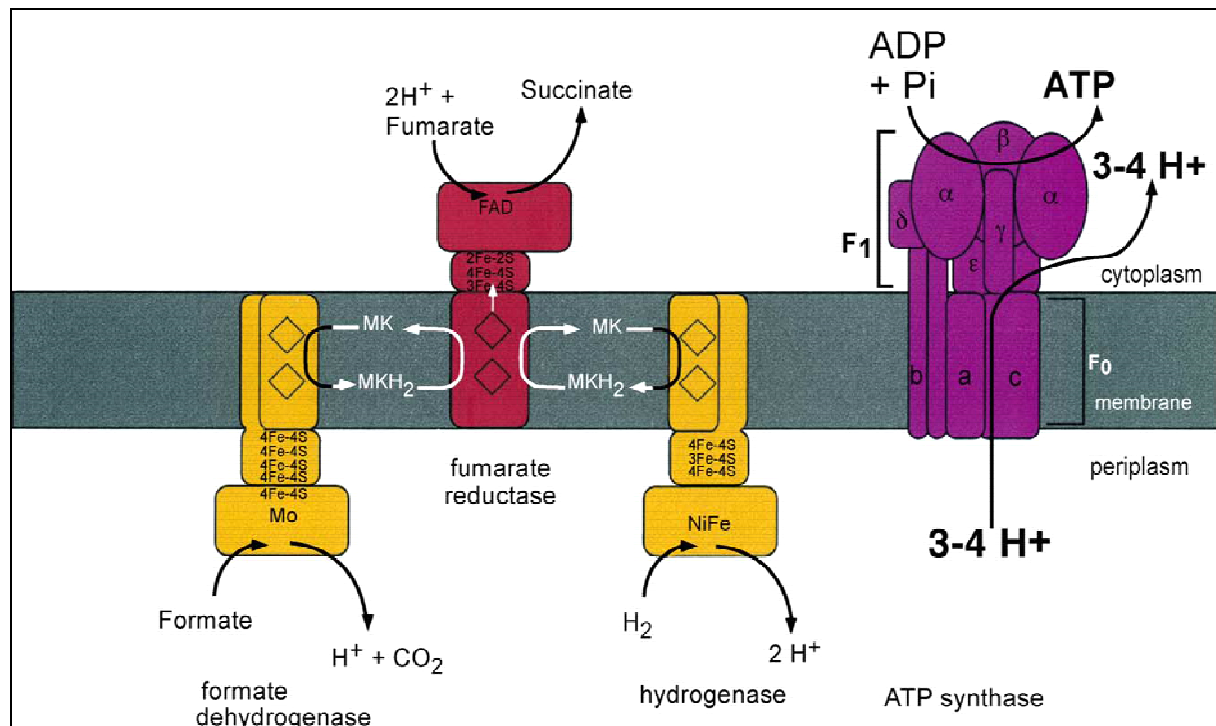


Figure 1.3: Scheme of anaerobic respiration in *Wolinella succinogenes*.

The enzymatic reactions are the same as described above in the text. The MK/MKH₂ indicates the menaquinol, which is the native quinone in this species. The figure was copied from ref. (Lancaster, 2002b).

1.4 Classification of SQORs

Together with the SQRs (also known as respiratory “complex II”), which catalyze the reverse reaction as part of the aerobic respiratory chain (Saraste, 1999) and the citric acid cycle, QFRs form the enzyme superfamily of succinate:quinone oxidoreductases (SQORs; EC 1.3.5.1; Hägerhäll, 1997; Ohnishi *et al.*, 2000; and Lancaster, 2003a). According to the composition of their hydrophobic domain and the respective heme content (Hägerhäll & Hederstedt, 1996; and Hederstedt, 1999) SQORs are classified in five types, i.e., types A to E (cf. references Lancaster, 2001 and 2002a for a more detailed description) as illustrated in Figure 1.4. Following this scheme, the QFR from *Wolinella succinogenes*, as well as the SQR from the Gram-positive bacterium *Bacillus subtilis*, are type B enzymes with one large hydrophobic subunit and two heme groups. These heme groups are termed “proximal” (b_P) and “distal” (b_D) based on their relative proximity to the hydrophilic subunits.

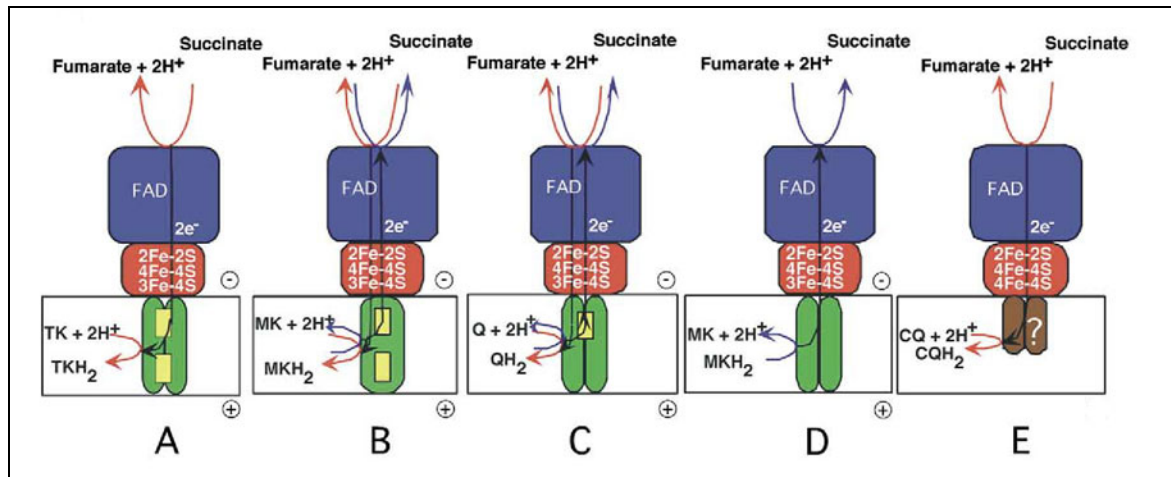


Figure 1.4: Classification scheme of SQORs (types A to E).

The scheme is based on the composition of the hydrophobic subunits and their respective heme content. The hydrophilic subunits A and B are shown in blue and red, respectively, and the hydrophobic subunits C and D in green. The heme groups are shown as yellow rectangles. Red and blue arrows indicate the directions of the reactions catalyzed by the SQR and QFR enzymes, respectively. The white rectangles around the hydrophobic subunits indicate the respective cytoplasmic or inner mitochondrial membrane (with positive and negative sides as indicated in the figure). The negative side corresponds to the cytoplasmic (“inside”) and the positive to the periplasmic (“outside”) side in bacteria; and in mitochondria, the negative side corresponds to the mitochondrial matrix (“inside”) and the positive to the intermembrane space (“outside”). In the case of type E, the orientation of the enzyme is not yet as clearly established as for the other types. The figure is copied from ref. (Lancaster, 2003c).

1.5 The Structure and Function of the Quinol:Fumarate Reductase from *W. succinogenes*

The crystal structure of *W. succinogenes* QFR in the oxidized state has been determined at 2.2 Å resolution (Lancaster *et al.*, 1999). The enzyme comprises two hydrophilic subunits (A and B, with molecular masses of 73 kDa and 27 kDa, respectively) and one hydrophobic, membrane-integrated subunit C (with a molecular mass of 30 kDa). The larger hydrophilic subunit A incorporates a covalently bound flavin adenine dinucleotide (FAD), the smaller hydrophilic subunit B contains three canonic iron-sulfur clusters ([2Fe-2S], [4Fe-4S], and [3Fe-4S]), and the hydrophobic subunit C harbors a distal and a proximal heme *b* group. Figure 1.5 shows the crystal structure of QFR.

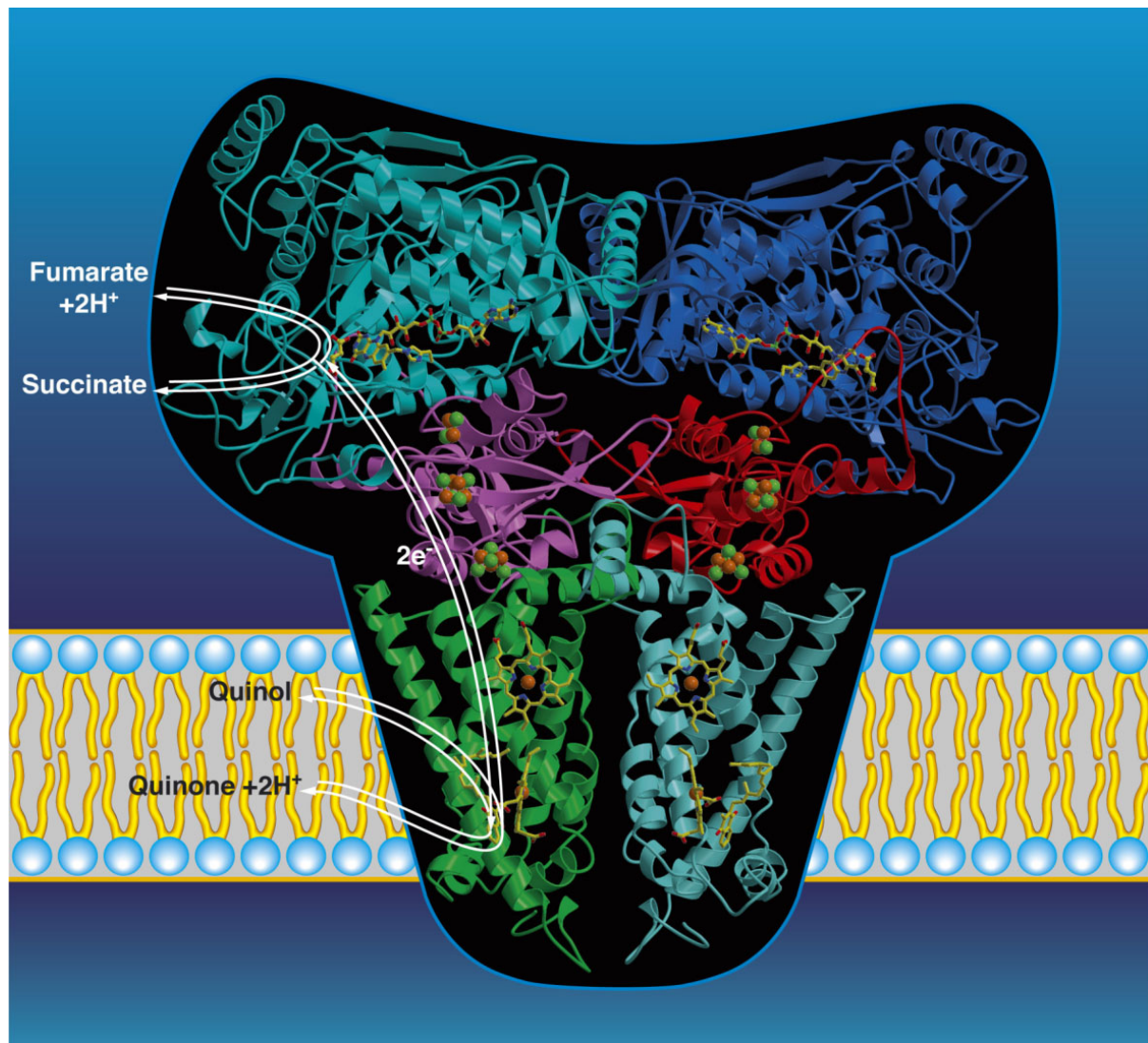


Figure 1.5: Three-dimensional structure of the *W. succinogenes* QFR dimer.

The QFR dimer is a heterotrimeric complex of subunits A, B, and C. The C α traces of the two A subunits are shown in *turquoise* and *blue*, those of the two B subunits in *purple* and *red*, and those of the two C subunits in *green* and *light blue* (the atomic structures of the six prosthetic groups per heterotrimer are superimposed for better visibility). From top to bottom, these are the covalently bound FAD, the [2Fe-2S], the [4Fe-4S], and the [3Fe-4S] iron-sulfur clusters, the proximal and the distal heme groups, b_P and b_D . Atomic color coding is as follows: C, N, O, P, S, and Fe are displayed in *yellow*, *blue*, *red*, *light green*, *green*, and *orange*, respectively. The position of the bound quinone was recently determined crystallographically (C. R. D. Lancaster, *unpublished*).

1.5.1 Coupled transmembrane electron and proton transfer in QFR: The “E-pathway” hypothesis

The site of menaquinol oxidation is located close to the periplasmic side of the membrane in the vicinity of amino acid residue Glu C66 (where “C” indicates the C subunit), which has been shown to be selectively essential for menaquinol oxidation (Lancaster *et al.*, 2000). The functional role and location of Glu C66 indicate that the two protons, which are

liberated during menaquinol oxidation, are released on the periplasmic side of the membrane (Lancaster *et al.*, 2000) and would thus lead to the generation of a transmembrane proton potential, as two protons are invariably bound from the cytoplasm upon fumarate reduction (Lancaster *et al.*, 2001). Hence, the catalytic reaction of *Wolinella succinogenes* QFR should contribute to the generation of a transmembrane electrochemical proton potential. However, as discussed previously (Lancaster *et al.*, 2000), experimental measurements on inverted vesicles and proteoliposomes containing QFR indicated repeatedly that the enzymatic reaction of QFR is an electroneutral process (Geisler *et al.*, 1994; Kröger *et al.*, 2002; and Biel *et al.*, 2002). In order to reconcile this apparent contradiction, the so-called “E-pathway” hypothesis of coupled transmembrane electron and proton transfer, which is illustrated in Figure 1.6, was proposed (Lancaster, 2002b). It states that the transmembrane transfer of two electrons via the two QFR heme *b* groups upon menaquinol oxidation is strictly coupled to a compensatory co-transfer of one proton per electron from the periplasmic to the cytoplasmic side of the membrane. This proton transfer occurs via a pathway, which is transiently open during the reduction of the hemes and closed in the oxidized state of the enzyme. The two most prominent constituents of the “E-pathway” were suggested to be the ring C propionate of the distal heme *b_D* and amino acid residue Glu C180.

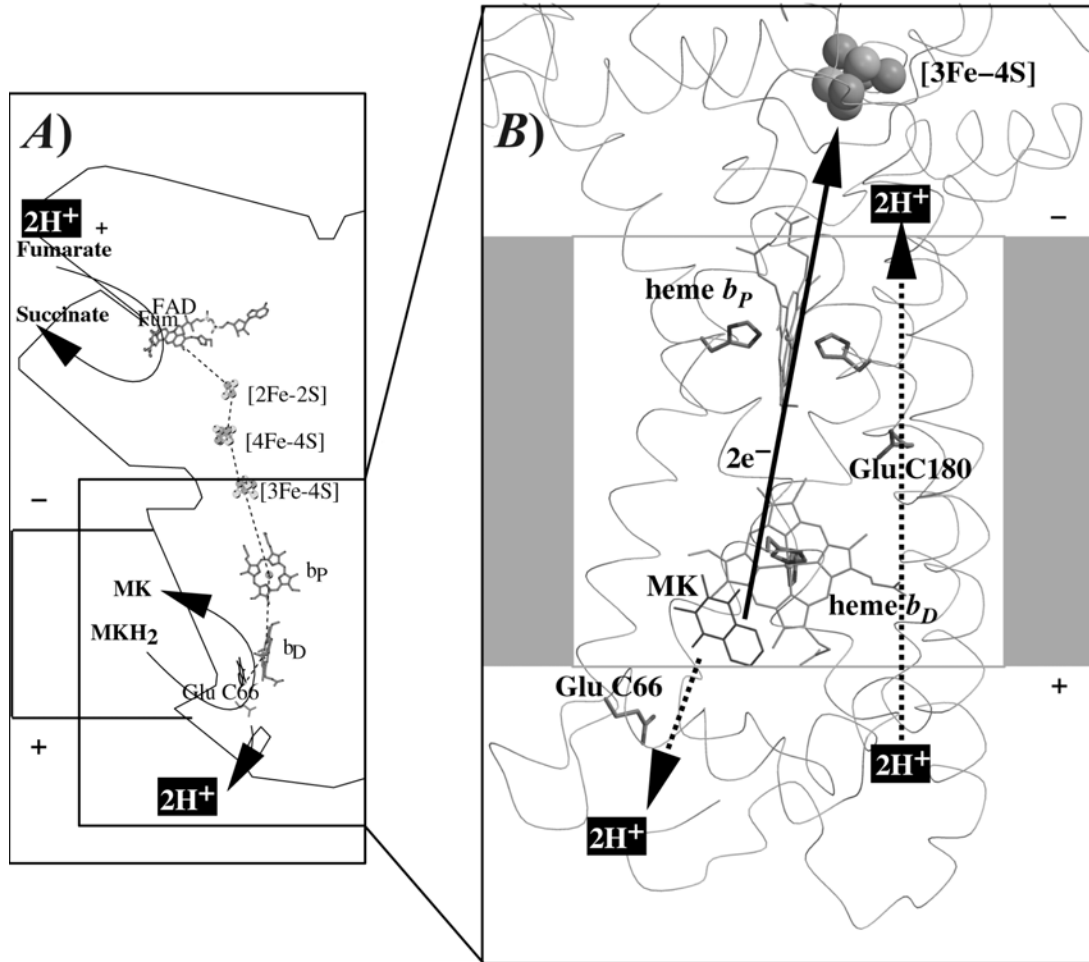


Figure 1.6: “E-pathway” hypothesis of coupled transmembrane ET and PT in QFR.

The negative side of the indicated membrane is the bacterial cytoplasm; the positive side corresponds to the periplasm. (A) Hypothetical establishment of a transmembrane electrochemical potential (without an “E-pathway”) as suggested by the essential role of Glu C66 for menaquinol oxidation by *W. succinogenes* QFR (Lancaster *et al.*, 2000). Figure 1 A features the prosthetic groups of the *W. succinogenes* QFR dimer (coordinates as in 1QLA; Lancaster *et al.*, 1999). Also indicated are the side chain of Glu C66 and a tentative model of menaquinol (MKH₂) binding. The position of bound fumarate (Fum) is taken from PDB entry 1QLB (Lancaster *et al.*, 1999). (B) Hypothetical co-transfer of one proton per electron across the membrane (“E-pathway” hypothesis; Lancaster, 2002b). The two protons that are liberated upon menaquinol oxidation are released towards the periplasmic side of the membrane via residue Glu C66. In compensation, coupled to electron transfer via the two heme groups, protons are transferred from the periplasm via the ring C propionate of the distal heme *b_D* and residue Glu C180 to the cytoplasm, where they counterbalance the two protons which are bound during fumarate reduction. In the oxidized state of the enzyme the “E-pathway” has to be inactive to prevent discharging of the proton potential (Lancaster, 2003a).

A part of this mechanism of coupled electron and proton transfer in QFR very likely involves a redox Bohr effect of the low-potential “distal” and the high-potential “proximal” heme *b* groups of QFR (as assigned in chapter 3.1.3 below).

The mechanistic details of redox Bohr effects can be of complicated nature as the effect can be considerably delocalized (Louro *et al.*, 1996) and protonatable groups other than simply the heme propionates might be involved. In the case of the QFR from *W.*

succinogenes, the circumstances for investigating redox Bohr effects are favorable since the amino acid sequence as well as the crystal structure of the enzyme is known (Lancaster *et al.*, 1999). Furthermore, a mutagenesis system for *W. succinogenes* QFR has been established (Simon *et al.*, 1998) which allows the investigation of specific enzyme variants.

As a part of this work, the pH-dependence of the heme *b* midpoint potentials of the *W. succinogenes* QFR wild-type enzyme and variant E180Q was investigated with the help of electrochemically induced VIS difference spectroscopy. Midpoint potential values for QFR WT hemes at pH 7 were previously measured and described (Lancaster *et al.*, 2000). A redox Bohr effect was measured for the high- and low-potential heme of both enzyme types in this study. The observed differences between WT and E180Q will be discussed with respect to the mechanism of the proposed “E-pathway” hypothesis.

1.6 Heme Propionate ¹³C-Labeling of QFR WT for FTIR Spectroscopy

As described above, the propionates of the heme groups can be involved in redox-coupled intra-protein proton transfer via the redox Bohr effect. For the proposed “E-pathway” hypothesis of coupled transmembrane electron and proton transfer in the quinol:fumarate reductase from *Wolinella succinogenes*, the participation of the ring C propionate of the distal heme group *b_D* in proton translocation was suggested to be essential for the enzymatic mechanism (Lancaster, 2002b). The orientation of this propionate in the structure of QFR (Lancaster *et al.*, 1999), as well as an observed redox Bohr effect on the distal heme group *b_D* (cf. chapter 3.2.3), and results from electrostatic calculations concerning the protonation state of the ring C propionate of the distal heme *b_D* (cf. chapter 3.1.2) indicate that it might act as a proton donor/acceptor in the proposed “E-pathway”.

In principle, electrochemically induced FTIR difference spectroscopy is the appropriate method to detect reaction-induced protonation and/or environmental changes of the heme propionates experimentally. An unequivocal assignment of potential signals though is difficult, as other protein vibrations and contributions from similar chemical groups such as Asp or Glu side chains heavily obscure the frequency range of the respective vibrations (see Figure 1.7). Thus, it is necessary to employ labeling methods, such as ¹³C-labeling of the heme propionates, to assign the propionate contributions in the difference spectra. The

expected signals arise from the protonated and deprotonated heme propionate species, as indicated in Figure 1.7.

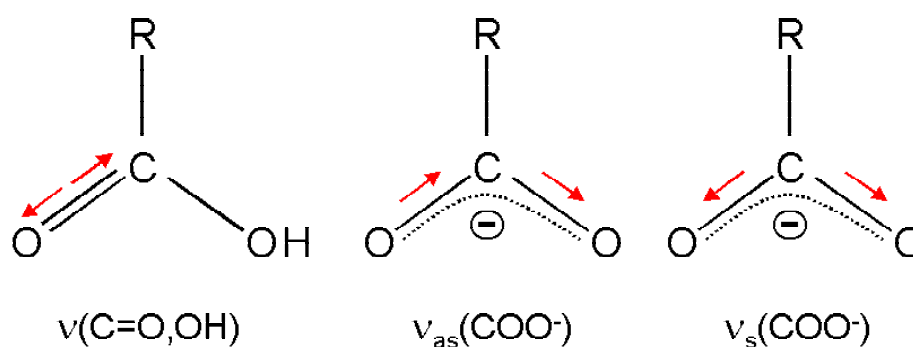


Figure 1.7: Schematic view of the three relevant heme propionate vibrations.

On the left, the carbonyl stretching vibration of the protonated carboxyl group (which absorbs between approximately 1700 cm^{-1} and 1665 cm^{-1}) is shown; in the middle, the antisymmetric vibration of the deprotonated form (between 1620 cm^{-1} and 1540 cm^{-1}); and on the right, the corresponding symmetric vibration (between 1420 cm^{-1} and 1300 cm^{-1}). The *red arrows* indicate the motion of the individual atoms. All vibrations shown are sensitive to the ^{13}C isotope exchange and a maximal downshift of 30 to 40 wavenumbers upon isotopic labeling of the heme propionate group is expected (Herzberg, 1962; Behr *et al.*, 1998).

The ^{13}C -labeling of the propionate groups was achieved by genetically modifying the pathway of heme biosynthesis of *W. succinogenes* (this work was accomplished by Mauro Mileni, MPI of Biophysics). This approach was similar to a method previously presented for the cytochrome *c* oxidase from *Paracoccus denitrificans* (Behr *et al.*, 1998). A *W. succinogenes* mutant was created, which is not able to synthesize δ -aminolevulinic acid, a precursor of the heme biosynthesis, by interrupting the C5 pathway. The heme biosynthesis in anaerobic bacteria is reviewed in ref. (Michal, 1999). Instead, the medium for the auxotroph *W. succinogenes* cells contained ^{13}C -labeled 1- ^{13}C - δ -aminolevulinic acid for heme assembly. Thus, the heme groups of the QFR enzyme contained two ^{13}C -labeled carboxyl groups specifically at the propionates (see Figure 1.8).

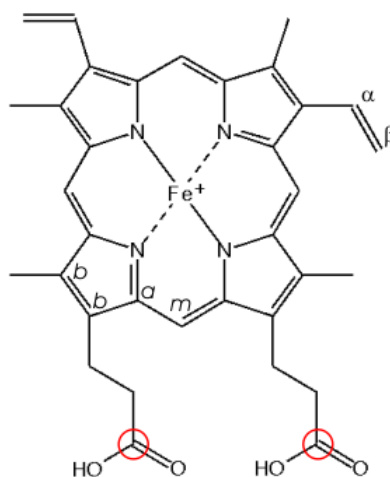


Figure 1.8: Chemical structure of the heme *b* group.

The *red circles* indicate the positions of the introduced ^{13}C atoms in the labeled hemes. In addition, the indices of the heme-carbon atoms in the porphyrin ring system and in the vinyl substituents are shown, as they will be used in the following text.

1.7 Goals of this Work and Motivation of the Employed Methods

The main goal of the presented work was to obtain a more detailed insight into the correlation between the structure and function of the fumarate reductase (QFR) from the obligate anaerobic ϵ -proteobacterium *Wolinella succinogenes*, and in particular to investigate the coupling mechanism of (transmembrane) electron and proton transfer, which takes place in this QFR (Lancaster *et al.*, 2000; and Lancaster, 2002b). This membrane bound enzyme is part of the anaerobic respiratory chain of *Wolinella succinogenes* and couples the reduction of fumarate to succinate to the oxidation of menaquinol to menaquinone. (The QFR enzyme is related to the succinate dehydrogenase – or respiratory complex II – which catalyzes the reverse reaction in mitochondrial aerobic respiration.)

The problem mentioned above should be addressed by two complementary approaches. The first technique was computer-assisted electrostatic calculations on the basis of the crystallographic structure of QFR in order to identify functionally relevant groups (such as amino acid side chains, cofactors and prosthetic groups) within the enzyme, and to gain insight into the coupling mechanism of electron and proton transfer processes. As a prerequisite for the calculations, the software should be adapted to the QFR model, and appropriate sets of parameters should be established to yield reliable results.

The “Multiconformation Continuum Electrostatics” (MCCE) software used in this work provides the possibility to simulate different environments for the protein with respect to external pH values and redox potential (E_h), and to perform redox and pH titrations in order to study the interactions of (redox) active groups within the used QFR model. Furthermore, different scenarios of intermediate (static) redox states of the enzyme should be chosen and implemented in the calculations to probe the subsequent response of the protein (e.g., protonation or conformational changes of side chains).

The theoretical calculations should be complemented by the second technique, which was electrochemically induced FTIR and VIS difference spectroscopy. The setup available at the Institute of Biophysics (Johann Wolfgang Goethe-University, Frankfurt) provides the possibility to perform experiments, which combine FTIR and VIS spectroscopy, and protein electrochemistry. A specially designed electrochemical cell is filled with the protein of interest in a buffered aqueous solution. Inside this cell, an external adjustable electrical potential can be applied to the sample and is measured via a three-electrode array. Thus, different redox states of the sample can be addressed and redox transitions can be monitored.

In order to perform the desired experiments, adequate experimental conditions should be established. This includes the choice of an appropriate surface modification for the gold grid working electrode of the setup, the optimization of the mixture of redox mediators, and the general experimental parameters of FTIR and VIS difference spectroscopy for this specific target, namely the QFR enzyme.

VIS and FTIR absorbance spectra, which belong to specific redox states of the protein, can directly be converted into characteristic difference spectra that can yield information about the chemical groups that contribute to the signal change (for instance by changing their protonation state, and thus being of potential importance for redox-coupled proton translocation within the protein). With the help of the additional VIS spectrophotometer, the redox behavior of the two heme *b* groups of QFR should be monitored and electrochemical redox titrations should be performed to obtain reliable midpoint potentials of the proximal and distal heme groups of QFR WT and enzyme variants at various pH values.

A further central aspect of the project was to investigate mechanistically interesting enzyme variants of QFR as a tool for the spectral interpretation of the wild-type data and subsequent FTIR band assignment.

Since both methods, theoretical and experimental, deal with equilibrium states of the enzyme, the results should be compared to mutually support a thorough analysis and interpretation of the data obtained from both techniques (and also to validate the theoretical predictions with experimental data). As a particularly promising synergetic possible result of the two techniques, an assignment of the distal and proximal heme positions to the observed high and low heme *b* midpoint potentials should be achieved.

2 MATERIALS AND METHODS

2.1 Materials

2.1.1 List of mediators

| Mediator | E_m [mV] vs. Ag/AgCl | Solvent | Company |
|--------------------------------|------------------------|---------------|---------|
| tetrachlorobenzoquinone | 72 | diethyl ether | Aldrich |
| 2,6-dichlorophenolindophenol | 9 | ethanol | Sigma |
| ruthenium hexaminchloride | -8 | water | Aldrich |
| anthraquinone-2,6-disulphonate | -23 | water | Fluka |
| 1,2-naphtoquinone | -63 | ethanol | Aldrich |
| anthraquinone | -108 | ethanol | Fluka |
| trimethylhydroquinone | -108 | ethanol | Aldrich |
| 5-hydroxy-1,4-naphtoquinone | -158 | ethanol | Fluka |
| duroquinone | -198 | ethanol | Fluka |
| menadione | -220 | acetone | Sigma |
| 2-hydroxy-1,4-naphtoquinone | -333 | ethanol | Aldrich |
| anthraquinone-2-sulphonate | -433 | ethanol | Aldrich |
| neutral red | -515 | ethanol | Sigma |
| benzyl viologen | -568 | water | Sigma |
| methyl viologen | -628 | water | Sigma |

Table 2.1: List of mediators for electrochemical measurements

The substances are sorted according to their standard redox potential E_{m7} (at pH 7).

2.1.2 List of chemicals

| Substance | Company |
|---|---|
| mercaptopropionic acid | Fluka, Switzerland |
| K ₂ HPO ₄ and KH ₂ PO ₄ (anhydrous) | Carl Roth GmbH & Co., Karlsruhe, Germany |
| KCl | Merck, Darmstadt, Germany |
| <i>n</i> -dodecyl- β -D-maltoside (LM) | Glycon Biochemicals, Luckenwalde, Germany |
| sodium borate | Merck, Darmstadt, Germany |
| cacodylic acid - sodium salt, trihydrate | Fluka, Switzerland |
| hydrochloric acid | Merck, Darmstadt, Germany |
| D ₂ O (99.9% purity) | Deutero GmbH, Kastellaun, Germany |

Table 2.2: List of chemicals

2.1.3 List of laboratory equipment

| Device | Company |
|---|--|
| modified Bruker IFS 25 FTIR spectrometer (including UV/VIS spectrometer) | as provided by Institute of Biophysics (Frankfurt University) |
| potentiostat | as provided by Institute of Biophysics |
| spectroelectrochemical cell | as provided by Institute of Biophysics |
| gold mesh (for working electrode) | Buckbee-Mears, St. Paul, USA |
| table centrifuge “4 K 10” | Sigma, Steinheim, Germany |
| table centrifuge “Labofuge 200” | Heraeus, Hanau, Germany |
| table centrifuge “5415C” | Eppendorf, Hamburg, Germany |
| precision balances | Sartorius, Göttingen, Germany |
| Centrisart I filtration tubes | Sartorius, Göttingen, Germany |
| Vivaspin 500 μ l concentrators | Vivascience, Hannover, Germany |

Table 2.3: List of laboratory equipment

2.2 Electrostatic Calculations

2.2.1 The “Multiconformation Continuum Electrostatics” method

The employed method of multiconformation continuum electrostatics (MCCE) has been developed and advanced by M. R. Gunner and coworkers. A comprehensive description of MCCE is given in refs. (Alexov & Gunner, 1997 and 1999; and Gunner & Alexov, 2000). The MCCE method, which was implemented locally at the MPI of Biophysics by C. R. D. Lancaster, allows the determination of the equilibrium conformational and ionization states of all protein side chains, non-solvent exposed water molecules, ions, ligands, cofactors, and prosthetic groups at a given pH and redox potential (E_h). It makes use of several pre-selected atomic positions and ionization states for amino acid side chains or heme propionates, cofactors, prosthetic groups, buried waters, and ligands. Thus, the use of MCCE permits the consideration of multiple positions for hydroxyl and water protons; alternative side chain rotamers for residues with strong electrostatic interactions are based on a “heavy atom rotamer library” (Dunbrack & Karplus, 1994; Dunbrack & Cohen, 1997). Every individual side-chain conformation and, for practical reasons, also the ionization state of a residue, as well as the reduced or oxidized state of a cofactor (or prosthetic group) is characterized as a “conformer”. In this way, the entirety of conformers represents all allowed states of the protein, which are incorporated into the calculations.

With the help of MCCE, tables of energies for all electrostatic and non-electrostatic self and pairwise interactions of all conformers can be constructed. An individual protein microstate is characterized by selecting one particular conformer for every residue, cofactor and water molecule of the protein, which is present in the investigated structural model. Thus, the total number of possible microstates is very high if several hundreds or more conformers are being considered in the calculations. Facing a vast number of microstates, MCCE uses “Monte Carlo sampling” in order to efficiently determine the probability for every conformer in the Boltzmann distribution for a given set of the parameters E_h and pH. It has previously been demonstrated that Monte Carlo sampling yields microstate populations, which approach a Boltzmann distribution (Beroza *et al.*, 1991). Further details on the employed Monte Carlo sampling procedure are given in refs. (Alexov & Gunner, 1997 and 1999; and Georgescu *et al.*, 2002).

Simulated redox titrations are performed by setting a fixed pH value prior to an individual Monte Carlo sampling run; for pH titrations a fixed potential E_h is set. In a similar

way, possible intermediate steps of electron transfer via the heme groups (see Figure 2.1) can be simulated by keeping the oxidation state of the hemes and the other cofactors fixed throughout the Monte Carlo sampling. Subsequently, the found protein microstates can be analyzed with respect to the effect that the fixed charge distribution has on the occupancy of the individual conformers (i.e., the protonation state of an acidic residue in terms of occupancy of the ionized and neutral conformer as well as the side-chain conformation).

2.2.1.1 Description of the individual steps of the complete MCCE calculation

1. All hydrogen atoms are removed from the used coordinate file (in addition, all surface waters and ions are removed automatically). Then, protons with no degrees of freedom are placed, and protons with no partial charges are placed in their torsion minima. Non-surface exposed waters in the coordinate file are addressed in atomic detail.

2. The program “DelPhi” (Nicholls & Honig, 1991) is used to calculate the electrostatic potential of the protein by solving the Poisson-Boltzmann equation (PBE) by using a finite difference method. The PBE represents the classical treatment of electrostatic interactions in solution (Honig & Nicholls, 1995):

$$\nabla \cdot [\varepsilon(\mathbf{r}) \nabla \cdot \phi(\mathbf{r})] - \varepsilon(\mathbf{r}) \kappa(\mathbf{r})^2 \sinh[\phi(\mathbf{r})] + 4\pi\rho^f(\mathbf{r})/kT = 0, \quad (14)$$

with the dimensionless electrostatic potential $\phi(\mathbf{r})$ measured in units of kT/q (k is the Boltzmann constant, T the absolute Temperature, and q the proton charge), ε is the dielectric constant, and ρ^f is the fixed charge density (in proton units). The term κ^2 equals $\kappa^2 = 1/\lambda^2 = 8\pi q^2 l / ekT$, with the Debye length λ , and the ionic strength l of the bulk solution. All variables (ϕ , ε , κ , and ρ) are functions of the position vector \mathbf{r} . When no mobile ions are present, the second term of eq. 14, which accounts for salt effects, vanishes ($\kappa = 0$), and eq. 14 becomes equal to the Poisson equation, which applies for the presented calculations.

In this computational study, the protein interior was assigned a dielectric constant of $\varepsilon = 4$, and a value of $\varepsilon = 80$ was chosen for water (Gilson & Honig, 1986). The assigned partial charges for the amino acid side chains were taken from the PARSE charge set (Sitkoff *et al.*, 1994). The partial charges of the heme groups and their His ligands, and also the reference midpoint potentials of the hemes were the same as in ref. (Gunner & Honig, 1991). The partial charges that were assigned to the three iron-sulfur centers were extracted from

(Stephens *et al.*, 1996) for the [3Fe-4S] center, from (Li *et al.*, 1998) for the [2Fe-2S] center, and from (Jensen *et al.*, 1994) for the [4Fe-4S] center, and are listed in APPENDIX 6.1.1. For comparison, uniform charge distributions for the iron sulfur clusters were tested. These did not have a significant influence on the obtained results. For the reference oxidation-reduction potentials of the iron-sulfur centers in solvent, typical experimental values for the different types of clusters in ferredoxins (reviewed in ref. Beinert, 2000) were chosen and adjusted by -0.5 V, which is given as a typical difference for the midpoints of synthetic clusters and native clusters in proteins (Mouesca *et al.*, 1994). For the performed simulated heme reduction, the used reference values are irrelevant since the redox states of the three clusters were kept fixed throughout the entire procedure of Monte Carlo sampling (see also APPENDIX 6.1.2 and 6.1 for an analysis of the influence of the FeS-redox states on the determined heme *b* midpoint potentials).

If a pair of residues is found which exhibits an interaction energy of greater than ± 2.1 Δ pK units, the corresponding residues will be provided with additional conformers based on the “heavy atom rotamer library” (Dunbrack & Karplus, 1994; and Dunbrack & Cohen, 1997). This procedure is sensible since those residues are more likely to change their conformation when the respective interacting residue undergoes a change of charge.

3. The different conformers for all amino acid residues, cofactors or prosthetic groups are generated. Arg and Lys side chains are provided with one neutral and one charged conformer. His residues obtain four neutral and two ionized conformers. Two basic His conformers are created by rotation of the side chain around the CB—CG bond. Each of the two cases is further divided into two neutral forms (either atom ND1 or NE2 is deprotonated) and one ionized form. Asn and Gln have two conformers with the terminal N and O atoms in exchanged positions. Asp, Glu and Tyr are supplied with one charged and two neutral (with the hydrogen atom placed in the torsion minimum) conformers. In addition, residues with hydroxyl groups (Ser, Thr, and the neutral forms of Asp, Glu and Tyr) are each provided with an extra conformer, which is capable of donating a hydrogen bond to all surrounding acceptors. All other amino acid residues (Ala, Cys, Gly, Ile, Leu, Met, Phe, Pro, Trp, and Val) are not provided with conformers. The ring C and D propionates of the heme groups are provided with conformers analogously to Asp and Glu residues. Water molecules obtain conformers, which donate and accept hydrogen bonds, as well as an additional conformer which does not interact with the protein, hence corresponding to bulk water. The conformers

for the reduced and oxidized species of cofactors and prosthetic groups are created in the same step.

4. One DelPhi run is performed for every single conformer, which has been generated in the previous step to calculate the electrostatic interaction energy $\Delta G_{crg}(i,j)$ between all pairs of conformers (i,j) . In each run there is only partial charges on one single conformer (other ionized residues are assigned net charges of ± 1 , and 0 for neutral conformers) and the electrostatic potential is computed with respect to the atoms of all other conformers in the structural model. In the same step, the interaction energy of an individual conformer with the polar backbone and side chains without conformers is computed and summed in a single value $\Delta G_{pol}(i)$. Finally, in step four, the reaction field energy (or desolvation penalty) $\Delta \Delta G_{rxn}(i)$ of each conformer is calculated in a second set of DelPhi runs, in which all residues are in their original positions except for the conformer whose reaction field energy is currently computed.

5. The self-energy (torsion) $\Delta G_{torsion}(i)$ and pairwise (Lennard-Jones interaction) non-electrostatic energies are computed for all generated conformers. The pairwise Lennard-Jones energies $\Delta G_{nonel}(i,j)$ are then added to the respective pairwise electrostatic energies $\Delta G_{crg}(i,j)$ which were computed in the previous step. Non-electrostatic pairwise interaction energies $\Delta G_{nonel}(i)$ between the conformers and rigid parts of the protein are added to the pairwise polar interaction energies $\Delta G_{pol}(i)$ of every conformer.

6. In the final step, the Monte Carlo sampling is carried out to determine the Boltzmann distribution of microstates and thus the occupancy of every included conformer as a function of the parameters E_h and pH. The results of Monte Carlo sampling are given in occupancy tables so that the most probable side-chain orientation or ionization state of a particular residue of interest can be extracted. The Monte Carlo sampling is based on the previously calculated microstate energies. The energy $\Delta G(n)$ of any microstate n is calculated as:

$$\Delta G(n) = \sum_{i=1}^M \delta_n(i) \left\{ \gamma(i) [2.3k_B T(\text{pH} - \text{pK}_{sol}(i))] + (\Delta \Delta G_{rxn}(i) + \Delta G_{torsion}(i) + \Delta G_{pol}(i) + \Delta G_{nonel}(i)) \right\} \\ + \sum_{i=1}^M \delta_n(i) \sum_{j=i+1}^M \delta_n(j) [\Delta G_{crg}(i,j) + \Delta G_{nonel}(i,j)]. \quad (15)$$

With: $k_B T = 0.43 \Delta pK$ units = 0.59 kcal/mol (at room temperature); M the total number of conformers; $\delta_n(i) = 1$ for conformers which are present in microstate n , and $\delta_n(i) = 0$ for conformers which are absent; $\gamma(i) = -1$ for acids, $\gamma(i) = 1$ for bases, and $\gamma(i) = 0$ for neutral groups. The $pK_{sol}(i)$ is the pK_a of an ionizable group i in solution, and $\Delta\Delta G_{rxn}(i)$ is the difference of the reaction field energy for residue i in solution and embedded in the protein, and $\Delta G_{torsion}(i)$ is the torsion energy of residue i . The terms $\Delta G_{pol}(i)$ and $\Delta G_{none}(i)$ are the electrostatic and non-electrostatic (Lennard-Jones) interaction energies between conformer i and the backbone, respectively the residues with no conformers. $\Delta G_{crg}(i,j)$ and $\Delta G_{none}(i,j)$ are the pairwise electrostatic and non-electrostatic interaction energies between conformer i and conformer j . The summation of the individual energy terms concerning pairwise interactions is chosen such that every interaction is only counted once in the sum.

The so called “intrinsic pK ” (pK_{int} ; Tanford & Kirkwood, 1957) is defined as the pK_a of a titrating group in the protein which it would adopt if all other ionizable groups would be in their neutral state:

$$pK_{int} = pK_{sol} - c_a(\Delta pK_{desolv} + \Delta pK_{pol}). \quad (16)$$

The parameter c_a is -1 if the site is an acid, and $+1$ for a base. The second and third term of equation (16) correspond to $\Delta\Delta G_{rxn}$ and ΔG_{pol} , respectively.

2.2.2 Structural model of QFR and coordinates

The structural model that was used in this work was based on the crystal structure of the oxidized QFR dimer of 260 kDa (PDB access code: 1QLA) determined at pH 6.0 as it has been described earlier (Lancaster *et al.*, 1999). Due to the large size of the protein complex, it was necessary to restrict the calculations to the coordinates of subunits B and C and the respective prosthetic groups of one QFR monomer. No membrane model was included in the calculations, since it is not likely that the inclusion of a membrane model would significantly affect the results, as has been discussed earlier for other membrane protein complexes (cf. ref. Lancaster *et al.*, 1996 and refs. therein; and Rabenstein *et al.*, 1998). The omission of the majority of crystallographic water molecules was advisable since their number is too great to be entirely incorporated in the multiconformation calculations without increasing the necessary computing time disproportionately. As a sensible compromise and in order to take advantage of the capability of the MCCE method to explicitly take into account water molecules (and especially different water conformers), a set of 21 water molecules which

were found in the crystal structure within a radius of 9 Å around the heme propionates of the two heme *b* groups and amino acid residue Glu C180, was included in the QFR model. A similar approach of omitting all crystallographic water molecules, except for a small set of water molecules, which are ligated to the metal binding sites, has been applied in a recent electrostatic study on the bovine heart cytochrome *c* oxidase (Popović & Stuchebrukhov, 2004). The QFR model including the 21 water molecules will be referred to as “model W” in the following, and the model without water molecules will be addressed as “model X”. In order to test the influence of the water molecules on the results, the calculations were performed both on model W and on model X for comparison.

Due to the absence of a crystallographically defined model for menaquinone (MK) or menaquinol (MKH₂) in the coordinate files of *W. succinogenes* QFR, which were available at the beginning of the project, no quinone species was included in the calculations. Since the *in vitro* activity of wild-type QFR enzyme is essentially restricted to the region between pH 5 and pH 9 (C. R. D. Lancaster, *unpublished*), this pH range is the focus of the results presented and discussed in this study.

The performed electrostatic calculations on the *Wolinella succinogenes* QFR model considered a total of 140 protonatable residues: 24 Arg, 30 Lys, 8 non-ligated His, 29 Asp, 27 Glu, 16 Tyr, 4 heme propionates, and 2 N-termini of subunits B and C. For these 140 residues, 711 (677) neutral and 348 (343) ionized conformers are created for model W (the numbers in parentheses refer to model X). For the 21 selected water molecules in model W, 310 conformers are generated. The remaining 269 (247) conformers are built for non-protonatable amino acid residues such as Ser and Thr, which are not provided with heavy atom rotamers but only different hydrogen atom positions. Ionizable amino acid residues (in three-letter code) will be distinguished with a superscript “⁺” or “⁻” or “⁰”, depending on the side chain charge (e.g., Glu⁰ for a neutral and Glu⁻ for an ionized glutamate conformer). Individual conformers are specified explicitly (with arbitrarily chosen lower case letters) only if the relevant conformer differs from the side-chain orientation in the crystal structure (PDB entry 1QLA) or if it is necessary to distinguish the specific conformers.

The MCCE calculations were performed on a Silicon Graphics O2 (SGI) Workstation, running IRIX 6.5.9 as operating system.

2.2.3 Simulated redox potential titrations

For simulating cofactor redox potential (E_h) titrations at a fixed pH, first a range of ambient redox potentials was chosen. Subsequently, Monte Carlo simulations were performed for each potential value E_h to determine the ionization states of all titratable groups in the QFR model at the specific value. The occupancy data of the reduced heme species were fitted with the standard Nernst equation (see eq. (3) in chapter 1.2.1) in order to deduce the midpoint potentials of the distal and proximal heme b groups. The experimental data (absorbance differences) that are shown for comparison in the results section were normalized to match the simulated curves. The simulated data are depicted as a sum of two single heme titration curves.

2.2.4 Simulated heme reduction

The exact order of individual electron transfer steps of electrons along the chain of cofactors and prosthetic groups of QFR is not known. For simulating heme reduction, one of the possible scenarios for intermediate states of electron transfer via the heme b groups of QFR was chosen. The order, which seems to be most probable, is described as follows: The reference redox state was chosen to be the oxidized state ($b_D^{ox} b_P^{ox}$), i.e. both, the distal (b_D) and the proximal (b_P) heme b groups were oxidized (the three iron sulfur clusters in enzyme subunit B remained oxidized for all presented simulations). The second intermediate state and first step of simulated heme reduction was to consider the distal heme b group, which is closest to the menaquinol binding site (Lancaster *et al.*, 2000), to be reduced and the proximal heme to remain oxidized ($b_D^{red} b_P^{ox}$). Thus, the first of two electrons has been transferred from the menaquinol to the nearest prosthetic group in the structure of QFR (Lancaster *et al.*, 1999). In the second step, the electron is transferred from the distal heme to the proximal heme. This leaves the distal heme oxidized and the proximal heme reduced ($b_D^{ox} b_P^{red}$). The third step introduces a second electron, which is transferred to the distal heme leaving both hemes reduced ($b_D^{red} b_P^{red}$). The considered steps of electron transfer are shown in Figure 2.1 and are in line with the arrangement of the prosthetic groups of QFR as it was found in the crystal structure of QFR (Lancaster *et al.*, 1999; and Lancaster *et al.*, 2000).

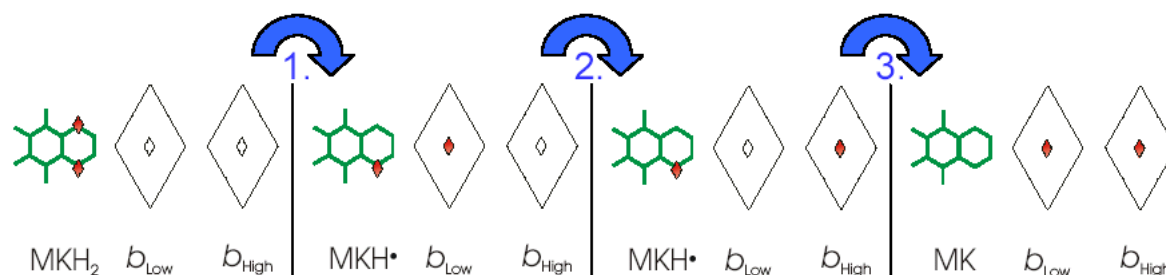


Figure 2.1: Electrostatic model of intermediate heme redox states in enzymatic electron transfer of QFR.

The state “Both hemes oxidized” was chosen to be the reference. In the second state, the low-potential distal heme is reduced, and in the third state, the electron is transferred to the high-potential proximal heme. In the “final” state, both hemes are reduced. MKH_2 symbolizes the menaquinol molecule, which was not included in the QFR model.

These initial steps of electron transfer in the catalytic reaction of QFR (i.e., menaquinol oxidation by fumarate reduction) have been simulated by pre-selecting the respective redox states of the two involved heme groups of the cytochrome *b* (QFR subunit C) and subsequent calculation of the corresponding ionization states and side-chain orientations of the individual groups of the QFR model as a function of pH. The presented calculations were carried out at a fixed potential of +25 mV (the standard midpoint of the fumarate/succinate redox couple at pH 7; Ohnishi *et al.*, 2000).

2.3 Electrochemically Induced VIS and FTIR Difference Spectroscopy

2.3.1 Electrochemistry

The Nernst equation, which has been introduced in chapter 1.2.1, describes how the redox potential E depends on the concentrations of the reduced and oxidized reaction partners. Differences in the electrochemical potential of two redox-active compounds cannot be measured directly. Instead, a reference electrode is required against which the potentials are measured (differences between potentials are independent on the specific reference, but the absolute value varies with the reference). To measure the exact potential differences, it is essential to keep the electrical currents in the electrochemical cell as low as possible, since the electric resistance of the system would create a voltage, which obscures the potential difference of interest. If the currents were very low in a “two-electrode” (working and reference electrode) setup, the system of electrodes and protein-buffer solution (the

“electrolyte”) would require a very long time to equilibrate. Thus, a “three-electrode” array is chosen, in which an additional counter electrode is incorporated (see Figure 2.2).

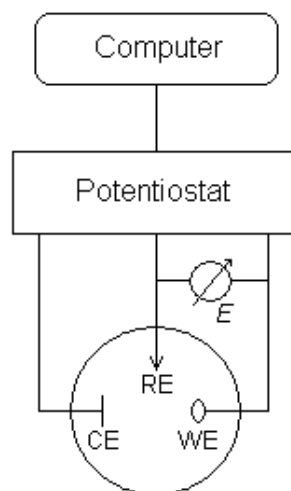


Figure 2.2: Scheme of the “three-electrode” array in the electrochemical cell.

CE is the counter, RE the reference, and WE the working electrode. E is the electrical potential measured between WE and RE. The potentiostat controls the applied potential and is controlled itself by a computer.

If a voltage is applied between the working and the reference electrode, the electric current can flow via the counter electrode, whereas the reference electrode (with a high electric resistance) stays current-free. This guarantees that the voltage, which arises across the electrolyte, is minimal. Thus, the electrical potential between working and reference electrode is hardly affected by the resistance of the electrolyte, which is further reduced due to the presence of a conducting salt in the solution.

2.3.1.1 The electrochemical cell

The electrochemically induced FTIR difference spectroscopy was performed in an ultra-thin-layer spectroelectrochemical cell (see Figure 2.3) that was designed for combined FTIR and UV/VIS spectrometry (Moss *et al.*, 1990; and Mäntele, 1996). The optical path length of this cell is variable and was of the order of 10 μm . The thin layer is essential for FTIR spectroscopy, but it additionally guarantees fast equilibration in the cell, since the layer is too thin for the establishment of a concentration gradient of reduced and oxidized species in the solution. Instead, the sample can be fully oxidized or reduced, directly following the applied electrode potential.

For the experiments, the spectroelectrochemical cell was filled with 8 μl of protein solution and the respective optical path length was checked spectroscopically after inserting the IR cuvette into the sample compartment. The applied potentials were measured with an Ag/AgCl reference electrode, which was connected to the electrochemical cell via a 3 M KCl salt bridge, but all values subsequently quoted are potentials versus the standard hydrogen electrode at pH 7 (SHE'). The preparation and calibration of the Ag/AgCl reference electrode are described in the APPENDIX 6.2.2. Finally, a thin platinum plate served as a counter electrode, which was in electrical contact with the sample (via the electrolyte in the buffer) but situated outside the IR beam.

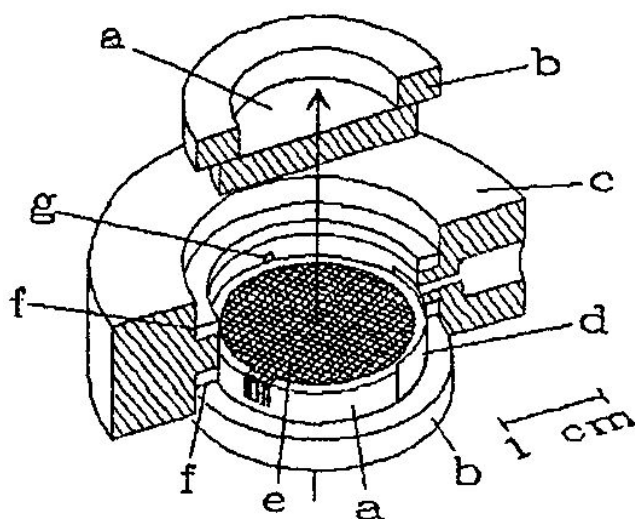


Figure 2.3: A schematic view of the spectroelectrochemical cell.

In detail: a) CaF_2 window, b) Plexiglas ring, c) PVC body, d) Pt counter electrode, e) Au grid working electrode, f) rubber O-ring, g) capillary connection to Ag/AgCl reference electrode. The figure was taken from ref. (Moss *et al.*, 1990).

2.3.1.2 Surface modification of the gold grid working electrode

The surface of the gold grid working electrode had to be chemically modified prior to the experiment in order to prevent irreversible protein adsorption. Thus, the electrode was treated with mercaptopropionic acid (Gries *et al.*, 1997). The gold grid was placed in ethanol, which contained 2 mM mercaptopropionic acid, for one hour, and was subsequently put in an ultrasonic bath for 15 minutes to obtain a monolayer of the surface modifier on the gold mesh.

2.3.1.3 Redox mediators

For fast redox reactions inside the spectroelectrochemical cell, a mixture of fifteen redox mediators was added to the protein solution (tetrachlorobenzoquinone; 2,6-dichlorophenolindophenol; ruthenium hexamminchloride; 1,2-naphthoquinone; trimethylhydroquinone; menadione; 2-hydroxy-1,4-naphthoquinone; anthraquinone-2-sulphonate; benzyl viologen; methyl viologen; neutral red (cf. Hellwig *et al.*, 1998 and refs. therein); 5-hydroxy-1,4-naphthoquinone; duroquinone; anthraquinone; and anthraquinone-2,6-disulphonate (Allen & Holmes, 1986). With the aid of this mixture, a (midpoint) potential range from roughly -0.4 V to 0.3 V (vs. SHE') was densely covered. The total concentration of each mediator substance in the experiment was approximately 40 μ M. At this concentration level, an enhanced equilibration speed is achieved. Yet it is low enough to avoid any disturbing spectral contributions on behalf of the mediator substances, which was confirmed in control measurements containing the mediators but no protein sample (data shown in APPENDIX, Fig 6.7).

2.3.2 Infrared spectroscopy

Infrared spectroscopy probes the vibrational modes of molecules. The transitions, which are observed around room temperature, usually occur between the ground state and the first excited vibrational level (with a change of the vibrational quantum number n of $\Delta n = \pm 1$). A fundamental requirement for the interaction of infrared light and a molecular vibration is the change of the electrical dipole moment of the molecule in the course of the vibration. Vibrations, which do not affect the dipole moment, are not IR-active. If the polarizability of the molecule is changed during the specific vibration, this vibration will be Raman-active. The strong selection rule that a Raman-active mode is not IR-active and vice versa, which applies quite well to small molecules, can be violated in larger systems. Consequently, many vibrations are Raman- and IR-active at the same time.

The energy E of the absorbed light is equal to the energy difference between the ground state and the first excited vibrational level; $E = h \cdot c / \lambda$ (with h : Planck's constant; c : speed of light, and λ : wavelength). The absorbance "Abs" or extinction E_λ at a particular wavelength λ is defined by Lambert-Beer's law:

$$E_{\lambda} = \log \frac{I_0(\lambda)}{I(\lambda)} = \varepsilon_{\lambda} \cdot c \cdot d, \quad (17)$$

where I_0 and I is the light intensity before and after passing the sample, respectively; ε_{λ} is the molar extinction coefficient; c the sample concentration; and d the thickness of the sample layer. The optical absorbance is a dimensionless quantity and is usually given in “OD” (optical density).

The difference spectra according to Lambert-Beer’s law, eq. (17), are subtracted as follows:

$$\Delta \text{Abs} = \log \frac{I_{\text{final}}(\lambda)}{I_{\text{initial}}(\lambda)}, \quad (18).$$

Vibrational spectra are traditionally plotted against the inverse of the wavelength λ , which is called the wavenumber $\tilde{\nu} = 1/\lambda = \nu/c$ (in units of cm^{-1} ; with ν : frequency). IR stretching vibrations are indicated with the symbol “ ν ”, whereas bending vibrations are indicated with a “ δ ”. The IR spectrum is roughly divided into three regions: the near-infrared (from 12,990 to 4,000 $\text{cm}^{-1} \equiv 770 \text{ nm}$ to 2.5 μm), the mid-infrared (from 4,000 to 400 $\text{cm}^{-1} \equiv 2.5$ to 25 μm), and the far-infrared (400 to 10 $\text{cm}^{-1} \equiv 25$ to 1000 μm). This is not a strict definition, and the values might change in different textbooks. The three regions are representative of different types of molecular vibrations. In the presented work, the focus lay on the mid-IR region, and in particular on the region between 2,000 and 1,000 cm^{-1} .

2.3.2.1 Fourier transform infrared spectroscopy

Ordinary dispersive IR spectroscopy is not suited for performing difference spectroscopy on proteins, as it is not fast and not precise enough. Those limitations can be overcome by using the so-called technique of Fourier transform infrared (FTIR) spectroscopy. The heart of every FTIR spectrophotometer is an interferometer, which is very often realized as a Michelson interferometer, as it is schematically shown in Figure 2.4.

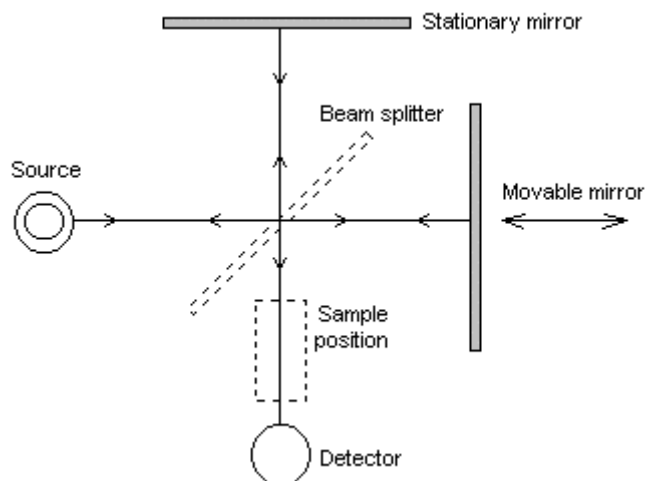


Figure 2.4: Basic scheme of a Michelson interferometer.

The device includes a (IR) light source, a beam splitter, a fixed and a movable mirror, the sample, and a detector (additional equipment, which is required for data acquisition and processing, and controlling the interferometer, is not included in this scheme). The figure was copied from the “Division of chemistry Homepage” of the Sheffield Hallam University, School of Science and Mathematics, Sheffield, UK (<http://www.shu.ac.uk/schools/sci/chem/tutorials/molspec/irspec3.htm>).

Behind the beam splitter, the two beams, which were reflected by the two mirrors, superimpose and interfere with each other. Then the IR-beam passes the sample, and the corresponding interferogram is sampled as a function of the position of the movable mirror. The absorbance spectrum and the interferogram are in principle identical, but a mathematical operation, called “Fourier transformation” (FT), is required to interchange between the two. In general, the FT determines the basic frequencies, which are included as components in an arbitrary continuous waveform (Herres & Gronholz, 1985). The FT is an integral operation, but since the distance x over which the movable mirror travels is finite, and since the interferogram is discretely sampled, Fourier *sums* instead of *integrals* are used for practical reasons as an approximation:

$$S(k \cdot \Delta\nu) = \sum_{n=0}^{N-1} I(n \cdot \Delta x) \exp(i2\pi n k / N), \quad (19)$$

where the continuous variables x and ν (in the FT integral) have been replaced by the discrete variables $n \cdot \Delta x$ and $k \cdot \Delta\nu$, respectively. S corresponds to the spectrum, and I to the interferogram. N is the number of (equidistant) points at which the interferogram is sampled. Mathematical algorithms are available, which allow very fast FT on standard personal computers.

Their main advantages of FTIR spectroscopy with respect to the conventional dispersive method are summarized in three points (Herres & Gronholz, 1985): a), the

“Jacquinot” or throughput advantage, which describes the higher throughput of IR radiation in FTIR spectroscopy, since circular apertures can be used instead of the linear slits in dispersive instruments; b), the “ Fellgett” or multiplex advantage, since all IR frequencies are detected simultaneously; and c), the “Connes” advantage of high wavenumber accuracy, which is achieved since the IR interferogram is digitized at the zero-crossings of the interferogram of a laser beam, which travels parallel to the IR beam.

2.3.2.2 FTIR spectroscopy in the context of coupled ET and PT in QFR

Proton transfer within a protein usually occurs via networks of hydrogen bonds, which are established by ionizable amino acid side chains (e.g., Asp or Glu), heme propionates, and internal water molecules. Especially with respect to protonated Asp or Glu side chains, the combined technique of electrochemistry and FTIR difference spectroscopy (Mäntele, 1993) is ideally suited to investigate their possible involvement in the enzymatic redox reaction (for recent reviews see refs. Fabian & Mäntele, 2002; and Barth & Zscherp, 2002). The technique is sensitive enough to monitor the redox reaction on the level of single IR-active chemical bonds. In addition, no groups other than protonated aspartic (Asp) or glutamic (Glu) acid side chains (Venjaminov & Kalnin, 1990), and a FAD carbonyl $\nu(\text{C}_4=\text{O})$ vibration in the oxidized state (Hellwig *et al.*, 2000; and Wille *et al.*, 2003) are expected to absorb in the relevant frequency range above 1710 cm^{-1} . The changes in absorbance, which occur during the redox reaction, are very small compared to the total IR bulk absorption. Thus, it is essential to compute difference spectra, which then exclusively contain contributions of the affected vibrations. The majority of protein FTIR difference bands arises from the electrochemically induced redox changes in the vicinity of the redox-active sites (i.e., cofactors, prosthetic groups or substrates).

In general, IR the absorption as well as the corresponding IR difference spectra of such large systems as entire proteins are usually very diverse and complicated. In order to achieve a reliable band assignment for at least some of the observed bands, there are two powerful techniques, which are also commonly used in a combined approach: One is isotopic labeling of the sample with, for example, ^{13}C , ^{15}N or ^{18}O atoms or to perform a hydrogen/deuterium ($^1\text{H}/^2\text{H}$) isotope exchange via D_2O buffers. The main object of these techniques is to change the physical mass of the labeled entity while maintaining its chemical properties. This altered mass is then reflected in shifted vibrational frequencies that can be observed in the IR spectra. The other technique is site-directed mutagenesis, which is used to

modify the functional group of an amino acid residue, and thus also modify its spectroscopic properties. In addition, the employed electrochemical cell allows monitoring individual redox-active groups by setting the appropriate electric reference potentials.

The combined method of FTIR spectroscopy and electrochemistry employed here as well as the mentioned strategies for IR band assignment are well established approaches and have previously been applied to several other membrane-bound enzymes, e.g., bacterial reaction centers (Leonhard & Mäntele, 1993), cytochrome *c* oxidase (Hellwig *et al.*, 1996, 1998 and 1999a), *ba*₃ oxidase (Hellwig *et al.*, 1999c), NADH:ubiquinone oxidoreductase (Hellwig *et al.*, 2000), cytochrome *bo*₃ (Hellwig *et al.*, 1999b and 2001), and cytochrome *bc*₁ complex (Baymann *et al.*, 1999; and Ritter *et al.*, 2003).

2.3.2.3 Experimental details of FTIR spectroscopy of QFR

All IR difference spectra in the range of 1800 cm⁻¹ to 1000 cm⁻¹ were recorded using a modified Bruker IFS 25 FTIR spectrometer that has been described by W. Mäntele and coworkers in previous reports (see for instance refs. Mäntele, 1993 and 1996). To suppress the disturbing influence of water vapor absorption, the sample compartment of the spectrometer has continuously been ventilated with dehumidified air (Hellwig *et al.*, 2000).

The protein samples had to be highly concentrated (~1.5 mM) in order to keep the signals of interest above the noise level. Concentrations below this level were sufficient for heme redox titrations in the VIS range, but not for resolving the small signals of protonated Glu or Asp side chains above 1700 cm⁻¹. Even higher concentrations cannot properly be pipetted as the protein-buffer solution is too viscous and does not contain enough water anymore. The high protein concentration is mainly necessary for two reasons: IR transmission experiments require a short optical path length because of the intense water absorption at around 1648 cm⁻¹ (i.e., the H-O-H bending mode with an extinction coefficient $\epsilon = 18 \text{ l}\cdot\text{mol}^{-1}\cdot\text{cm}^{-1}$; Mäntele, 1996). Due to limited detector sensitivity, the thickness of the water layer should not exceed 10 μm to keep the absorbance around 1648 cm⁻¹ below 1 OD (in D₂O the situation is less critical since the corresponding absorbance band is shifted to ~1210 cm⁻¹; see APPENDIX, Fig. 6.6). Furthermore, the extinction coefficients of $\nu(\text{COOH})$ modes are considerably small ($\epsilon = 200\text{--}400 \text{ l}\cdot\text{mol}^{-1}\cdot\text{cm}^{-1}$; Venyaminov & Kalnin, 1990), and the ratio of solvent to protein concentration is about 40,000.

Difference spectra were obtained by applying an initial potential for which all the cofactors of QFR were either fully reduced or fully oxidized. Before recording the respective

single-beam spectrum after performing a potential step, the protein had to be given some time to equilibrate. Thanks to the various mediators, the very thin layer of the protein solution and the gold grid surface modification of the working electrode, equilibration times were rather short (of the order of one to three minutes), which is necessary for good baseline stability. Furthermore, a triangular apodization function and a “zero filling factor” of 2 were applied. The “zero filling” of the raw data is used to interpolate the spectrum (and thus to increase the digital resolution – if a genuine resolution of 4 cm^{-1} is employed, the data spacing is 2 cm^{-1} after FT). The “zero filling” also reduces the error, which occurs due to the discrete sampling of the true interferogram (“picket-fence” effect; Herres & Gronholz, 1985). A noise level of below 5×10^{-5} is estimated by inspecting the baseline above $\sim 1750\text{ cm}^{-1}$, where no noticeable signals are expected and found. The noise level is considerably higher in the region of strong solvent absorption, as can be seen by sequentially recording baselines. None of the presented data was smoothed or subjected to any spectral deconvolution (if not mentioned otherwise) after data acquisition. The only method employed to enhance the signal-to-noise ratio was to average multiple single beam spectra. Each single beam spectrum is the result of the co-addition of 128 interferograms with a spectral resolution of 4 cm^{-1} . All measurements were performed at 5° C , and all graphs were prepared with the software Origin 7 (OriginLab Corp., USA).

2.3.3 VIS spectroscopy and heme redox titrations of QFR

VIS spectroscopy involves higher energies of the light quanta than in the infrared range, since electronic and not vibrational transitions are excited. The energy of the excited state subsequently decays via emission of radiation (where the energy of the light quantum is equal to the energy difference of the electronic states) or can stimulate chemical reactions or dissipate radiation-less by inducing molecule vibrations.

The expected VIS absorbance of the hemes is due to redox induced charge transfer between the electronic systems of the central iron and the porphyrin ring or the ligands. For the hemes, a ground state S_0 and three excited states S_1 to S_3 are considered; and the corresponding transitions are of the type $\pi\text{-}\pi^*$. The two dominant contributions in the spectra are caused by $S_0 \rightarrow S_1$ (α -band) and $S_0 \rightarrow S_3$ (Soret-band) transitions.

The VIS spectra in the range of 400 nm to 700 nm were measured with the same setup as described above, namely the VIS spectrophotometer, which is incorporated in the modified

Bruker IFS 25 FTIR setup. Similar to the FTIR, VIS difference spectra were obtained by applying an initial potential at the electrode for which both, the high- and the low-potential heme *b* groups, b_H and b_L , of QFR were either fully reduced or fully oxidized. Then a single-beam spectrum was measured and taken as a reference for subsequent potential steps that covered the potential range between fully reduced and fully oxidized. For the titration experiments, the protein samples were typically given three to ten minutes (depending on the direction of the reaction, the mediator concentration and the pH) to equilibrate between the potential steps (typically 25 mV). Again, all experiments were performed at 5° C. The titration curves were generated on the basis of the redox-dependence of the amplitudes of the Soret- and α -band at 428 nm and 561 nm, respectively. In order to obtain values for the midpoint potentials of heme b_H and heme b_L , the data points were fitted using a Nernst equation (eq. (3) in chapter 1.2.1) with $n = 1$ by relating the amplitude of the VIS difference bands to the concentration of the oxidized and reduced heme species as a function of the redox potential (see APPENDIX 6.2.1). For the investigation of the redox Bohr effect, the midpoint potentials of the high- and low-potential hemes of QFR were plotted against the pH and the resulting curves were fitted and analyzed with eq. (12), which was introduced in chapter 1.2.1. All fitting procedures and the data presentation were performed with the software Origin 7.

2.3.4 Sample preparation

Site-directed mutagenesis, cell growth of *Wolinella succinogenes* wild-type and mutants, and purification of the respective enzymes are described for WT QFR in ref. (Lancaster *et al.*, 1999), for variant E180Q in (Lancaster, C. R. D., Sauer, U. S., Groß, R., Haas, A. H., Mäntele, W., Simon, J., and Madej, M. G., *manuscript in preparation*), for variant E66Q in (Lancaster *et al.*, 2000), and for variant E270Q in (Lancaster, C. R. D., Groß, R., and Simon, J., *manuscript in preparation*). For electrochemically induced FTIR spectroscopy between pH 5.5 and pH 8, the QFR was washed and concentrated in 100 mM potassium phosphate (KP_i) buffer containing 100 mM KCl as supporting electrolyte and 1 mM *n*-dodecyl- β -D-maltoside ($cmc = 0.17$ mM; VanAken *et al.*, 1986) as detergent. Above pH 8, a 100 mM sodium borate buffer, containing 100 mM KCl and 1 mM *n*-dodecyl- β -D-maltoside, was chosen. Below pH 4.9, the QFR was measured in sodium cacodylate buffer (which is toxic as it contains arsenic compounds!). This buffer was prepared with cacodylic

acid - sodium salt, and the pH was adjusted with concentrated hydrochloric acid. Furthermore, as described above, the buffer contained 100 mM KCl and 1 mM LM.

Samples with protein concentrations of up to 1.5 mM were prepared for the spectroscopic experiments. For the necessary washing cycles, Centriscart I filtration tubes with a cut-off weight of 100 kDa and a volume of 2 ml were used. The final sample volume was adjusted in Vivaspin 500 µl concentrators, also with a 100 kDa cut-off. Samples in D₂O were prepared in an analogous way. The 100 mM standard solutions of K₂HPO₄ and KH₂PO₄ (both anhydrous), which also contained 100 mM KCl, were made with D₂O of 99.9% purity. By titrating the two standard buffer solutions against each other, an observed pH_{obs} of 7 was set that corresponds to a pD value of 7.4 (pD = pH + 0.4; Glasoe & Long, 1960). Finally, the detergent was added to the buffer. The samples were then repeatedly concentrated and washed with D₂O buffer until the calculated water content of the protein solution was well below 0.1 %. Following the same ¹H/²H isotope exchange strategy as for the cytochrome *c* oxidase from *Paracoccus denitrificans* (Hellwig *et al.*, 1996), the extent of ¹H/²H exchange was estimated to be of the order of 80 %, which is in line with previous studies on other membrane-bound redox enzymes.

2.3.5 Heme propionate ¹³C-labeling

The *W. succinogenes* QFR with ¹³C-labeled heme propionates was obtained from M. Mileni (see chapter 1.6), and the experimental details are to be published (Mileni, M., Haas, A. H., Mäntele, W., Simon, J., and Lancaster, C. R. D., *manuscript in preparation*).

3 RESULTS

3.1 Electrostatic Calculations

In the context of rationalizing the “E-pathway” hypothesis, the effect of transmembrane electron transfer (via the distal and proximal heme groups of QFR) on the protonation states of residues in the vicinity of the hemes was computationally investigated in this study. If the “E-pathway” hypothesis is valid, then transmembrane electron transfer via the heme groups is predicted to be associated with transmembrane proton transfer. This, in particular, should be reflected in changed ionization states of titratable residues that are actively involved in the suggested proton transfer. Other electron transfer-associated proton transfer events in the enzyme, such as those at the active sites of menaquinol oxidation and fumarate reduction, have not been investigated.

The second aspect of the electrostatic calculations was to investigate the electrochemistry of the heme groups of QFR (via simulated E_h and pH titrations) and the assignment of the low- and high-potential hemes to the distal and proximal positions in the structure of QFR. This is also of relevance to the catalytic mechanism and the general understanding of the enzyme, since all other prosthetic groups of QFR are already characterized by their oxidation-reduction potentials and their unique position in the structure (Lancaster *et al.*, 1999, and Lancaster, 2004).

Finally, the presented results based on electrostatic calculations are compared and discussed with respect to available experimental results.

3.1.1 Electrostatic interactions of the hemes and their propionates with the protein

The interaction energies of every conformer of the QFR model with all others were calculated, yielding a symmetric interaction matrix with $n \times n$ entries (n being the total number of conformers). Model W comprises 1638 conformers (1267 for model X). Table 3.1 contains a list of 37 conformers interacting with the proximal and distal heme b groups and their propionates which were chosen according to the following criteria: All conformers which are listed have both an interaction energy with one of the hemes or their propionates of $\pm 2 \Delta pK$ units or greater as well as a minimum occupancy of 5 % at pH 7 in the oxidized state

of the QFR model. The entries are ordered according to the z-coordinate of the residues since this coordinate approximately coincides with the membrane normal (with the hydrophobic region ranging from $z = -25 \text{ \AA}$ to $z = -55 \text{ \AA}$; C. R. D. Lancaster, *unpublished*). The initial state was defined to be the state in which all heme groups are oxidized. For practical reasons, Table 3.1 also contains three conformers “b”, “d”, and “f” of water molecule W33, and a second ionized conformer “k” of Glu⁻ C180. As will be explained later in the text, conformer “k” of Glu⁻ C180 is necessary for the discussion, and the three conformers of W33 are strongly interacting with conformer “k” of Glu⁻ C180.

Table 3.1: The electrostatic interaction energies of model W of QFR.

(A) All interaction energies in the oxidized state $b_D^{ox} b_P^{ox}$ are given in ΔpK units. Entries above $\pm 2 \Delta pK$ units are highlighted: positive values in *gray* and negative values in *black*. Residues are specified by residue name, protein chain, residue number in the chain, and conformer. Entries of value “0.0” have been omitted for clarity. The five rows and columns containing entries for hemes (Hem) and propionates (Paa⁻ X 1, Pdd⁻ X 1, Hem⁺ X 1, Hem⁺ X 2, and Paa⁻ X 2) are highlighted with *bold frames* and *bold numbers*. All entries are sorted with respect to the z-coordinate of the conformer. The *horizontal* and *vertical black bars* indicate the separation of strong interactions within the upper left quadrant and within the lower right quadrant, respectively. (B) The z-coordinate of the conformers in Angstrom (\AA), starting with the [4Fe-4S] center on the cytoplasmic side and ending with Glu C166 close to the periplasmic side of the membrane (the z-axis is normal to the membrane plane). The z-coordinates of the following residue atoms (nomenclature as in the PDB file) were quoted: CZ (Arg), CG (Asp), CD (Glu), NZ (Lys), CD (Gln), OG (Ser), OH (Tyr), FE (Hem), CGA (Paa), CGD (Pdd), FE1 [4Fe-4S], FE1 [3Fe-4S], and OH (HOH). Additional entries are the contributions of the loss of reaction field energy ($\Delta\Delta G_{rxn}$) and pH-independent polar interactions (ΔG_{poi}) to the intrinsic pK_{int} value of the specific conformer. The used solution pK_{sol} values were: 12.5 (Arg), 4.75 (Asp), 4.75 (Glu), 6.5 (His), 10.8 (Lys), 8.0 (Ntr), and 4.75 (Paa, Pdd). The calculated and employed solution solvation energies in ΔpK units were: -9.9 (Arg⁺), -12.6 (Asp⁻), -13.1 (Glu⁻), -8.9 (His⁺), -13.6 (Lys⁺), -10.4 (Ntr⁺), -12.4 (Paa⁻, Pdd⁻), -7.0 (Hem⁺), -26.6 [4Fe-4S], and -30.6 [3Fe-4S]. The last row, respectively column of the table features the conformer occupancy at pH 7.

Both oxidized hemes feature strong (negative) stabilizing, interactions of comparable magnitude (around $-3.4 \Delta\text{pK}$ units) with respect to their accompanying ionized propionates. In addition, the proximal heme shares several (positive) destabilizing interactions with ionized Lys and Arg residues (see Figure 3.2). The strongest individual destabilizing interaction of $+2.1 \Delta\text{pK}$ units is due to Lys⁺ C193, and the additional destabilizing interactions below the threshold of $2.0 \Delta\text{pK}$ units are due to Arg⁺ C189, Lys⁺ C100, and Arg⁺ C99. No further strong stabilizing interactions of larger magnitude than the threshold of $-2.0 \Delta\text{pK}$ units (except the mentioned two propionates) exist for the proximal heme b_P .

The distal heme b_D has fewer destabilizing interactions and only Arg⁺ C162 (see Figure 3.2) exceeds the threshold with $+2.1 \Delta\text{pK}$ units. Instead, b_D has an additional, strongly stabilizing interaction of $-2.6 \Delta\text{pK}$ units with conformer “l” of Glu⁻ C180. This conformer also stabilizes the oxidized species of the proximal heme, but only by $-1.1 \Delta\text{pK}$ units. Also conformer “k” of Glu⁻ C180 stabilizes the two oxidized hemes, but to a lesser extent compared to conformer “l”. It is conformer “k” which corresponds to the conformation of Glu C180 in the crystal structure 1QLA (see Figure 3.6 below for a detailed picture).

The arrangement of the conformers in Table 3.1 with respect to their z-coordinates also reflects the higher number of possible interaction partners for the proximal heme and its propionates in the structure of QFR. Furthermore, Table 3.1 can be subdivided in two parts, which do not have any strong interactions in common that would exceed the threshold of $\pm 2 \Delta\text{pK}$ units. This is indicated by the black cross, which divides the interaction table into four quadrants. The strongest “link” between the two groups is amino acid residue Glu C180. The two ionized conformers “k” and “l” stabilize the proximal oxidized heme by -0.9 and $-1.1 \Delta\text{pK}$ units, respectively.

Similarly to Glu and Asp side chains, several conformers are generated by MCCE for the four heme propionates. As a result of the calculations, all four propionates adopt a single conformation (i.e., 100 % occupancy in the oxidized state at pH 7). By comparison it was identified that the orientations of the respective four heme propionate conformers do not differ from the original X-ray crystal structure. In the oxidized state, the two propionates of the proximal heme are fully ionized, and they both meet the criteria to appear in Table 1. In the case of the distal heme, the ring D propionate is also fully ionized, whereas the ring C propionate is in its neutral, fully protonated state. The neutral species is not engaged in strong electrostatic interactions exceeding $\pm 2 \Delta\text{pK}$ units, and is consequently not listed in Table 3.1. Inspection of the electrostatic interaction energies of the *ionized* conformer of the distal ring C

propionate shows that it *would* strongly interact with the oxidized distal heme, the ionized ring D propionate of the distal heme, and also with the ionized Glu C180.

The described protonation pattern of the four heme propionates does not change in the neutral pH range throughout the course of the simulated steps of heme reduction. The three ionized heme propionates are all strongly stabilized by several favorable interactions with positively charged residues (see Table 3.1). The two propionates of the proximal heme are also subjected to some large destabilizing interactions, particularly with each other (+7.0 Δ pK units), but also with the oxidized [3Fe-4S] cluster and with the ionized Asp⁻ C27.

3.1.2 Protonation states of residues interacting with the hemes

In the oxidized state at pH 7, all conformers of ionizable residues which display strong interactions with the hemes and their propionates (listed in Table 3.1) have an occupancy of very close or identical to 100 % with the exception of Arg⁺ B167 and Glu⁻ C180. Residue Arg B167 is also fully ionized but the conformer of Arg⁺ B167, which is strongly interacting with the ring D propionate of the proximal heme, only accounts for 72 % of the total occupancy. Another ionized conformer, whose side chain is tilted by roughly 90 degrees and is pointing away from the ring D propionate of the proximal heme, covers the remaining 28 %. Glu C180 is only partially ionized in the oxidized state at pH 7, and the contribution of the relevant “1” conformer to the total occupancy is 49 %. The role and protonation state of residue Glu C180 will be discussed in detail later in the text. The conformers with high occupancy are in detail:

- a) for the proximal heme and its propionates: Arg⁺ B167, Arg⁺ B232, Asp⁻ C27, Lys⁺ C100, Arg⁺ C99, Lys⁺ C193, and Arg⁺ C189, and
- b) for the distal heme and its propionates: Glu⁻ C180, Tyr⁰ C172, and Arg⁺ C162.

All of the residues mentioned above, except for Glu⁻ C180 and Tyr⁰ C172, are in their original conformation as deduced by X-ray crystallography (Lancaster *et al.*, 1999). The different conformations of Glu⁻ C180 have already been introduced above (see also Figure 3.6); and in the case of Tyr⁰ C172 the phenol ring is slightly tilted compared to the original orientation in the crystal structure.

3.1.3 Comparison of simulated and experimental E_h titrations and heme assignment

Figure 3.1 shows the results of the simulated E_h titrations at pH 7 for model W and model X, as well as a comparison with experimental QFR wild-type data measured at pH 7 (Lancaster *et al.*, 2000). The experimentally derived midpoint potentials, which are included in Figure 3.1, are -149 mV for the low-potential and -9 mV for the high-potential heme. Furthermore, Figure 3.1 shows the simulated data for model X, and the obtained oxidation-reduction potentials are -149 mV for the low- and -48 mV for the high-potential heme. For model W, the midpoint potentials, which were found, are -125 mV for the low- and -12 mV for the high-potential heme. Thus, the net effect of inclusion of the water molecules in model W was an increase of the midpoint potentials by $+24$ mV for the low- and $+36$ mV for the high-potential heme.

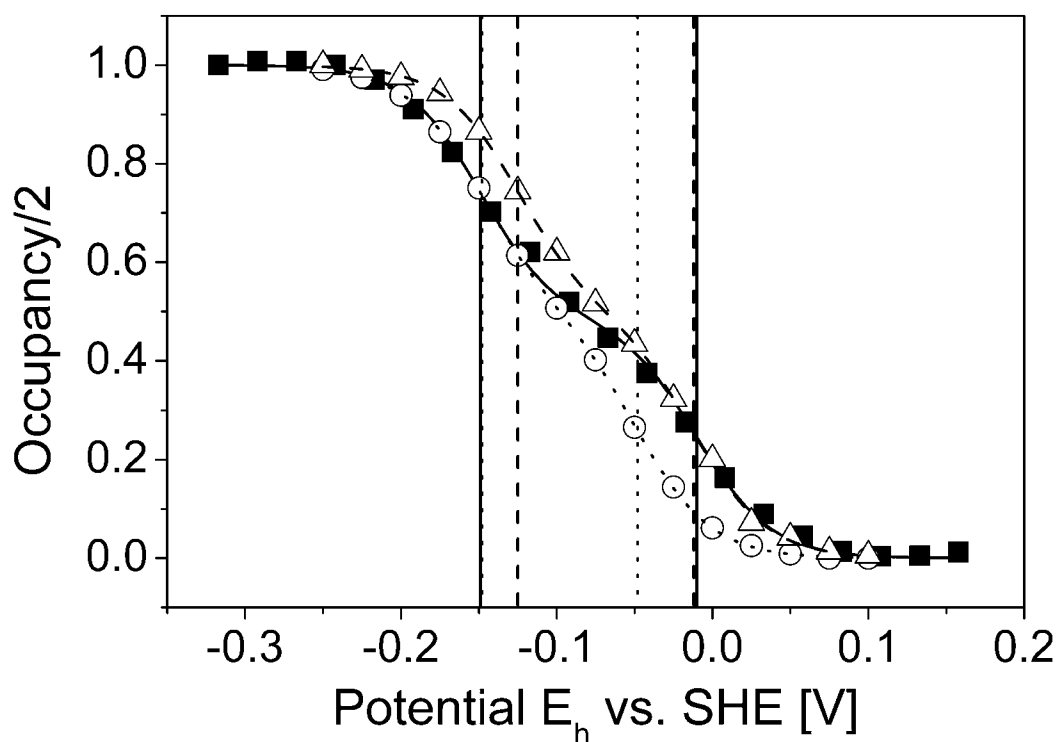


Figure 3.1: Simulated heme redox titrations.

The figure shows the data of simulated and experimental (Lancaster *et al.*, 2000) redox titrations of hemes b_p and b_D at pH 7. The *black squares* represent the experimental data, *open circles* are simulated data using model X, and *open triangles* show simulated data for model W. The three fitted Nernst-curves are also included: experimental (*solid*); simulation, model X (*dotted*); and simulation, model W (*dashed*). The *vertical lines* (same labeling as for the Nernst-curves) indicate the positions of the individual oxidation-reduction potentials as they were obtained by the Nernst-fit: 1) low-potential heme: -149 mV (experiment), -149 mV (simulation, model X), and -125 mV (simulation, model W); and 2) high-potential heme: -9 mV (experiment), -48 mV (simulation, model X), and -12 mV (simulation, model W). The low-potential heme corresponds to heme b_D and the high-potential to b_p .

Since the obtained midpoint potentials are directly related to the heme coordinates, the lower midpoint potential could be assigned to the distal heme position, and the higher midpoint potential to the proximal position in the structure as a result of this study. Previous tentative assignments of the low- and high-potential heme to the distal and proximal position in a related enzyme have been made (Hägerhäll *et al.*, 1995) but were partly based on assumptions, thus leaving some uncertainty (see discussion).

The way in which the protein environment modulates the two different midpoint potentials such that the two values differ by 113 mV for model W (and 101 mV for model X) is reflected in part *B*) of Table 3.1 and ultimately in the sum of all mutual electrostatic interactions. The relevant properties are the loss of reaction field energy $\Delta\Delta G_{rxn}$ and the direct electrostatic interactions with the surrounding ionized bases, which were mentioned in paragraph 3.1.2 and which are listed in Table 3.1. These residues are responsible for the most part of the difference in destabilization of the oxidized state of the two hemes. The oxidized form of the high-potential proximal heme is more destabilized than the low-potential distal heme because of four basic residues, namely Arg⁺ C99, Lys⁺ C100, Arg⁺ C189, and Lys⁺ C193 in the vicinity of the heme propionates of the proximal heme. In contrast to the proximal heme, the distal heme is only significantly destabilized by Arg⁺ C162. The orientation of the heme groups of QFR with respect to the relevant ionized basic residues in the structure is shown in Figure 3.2.

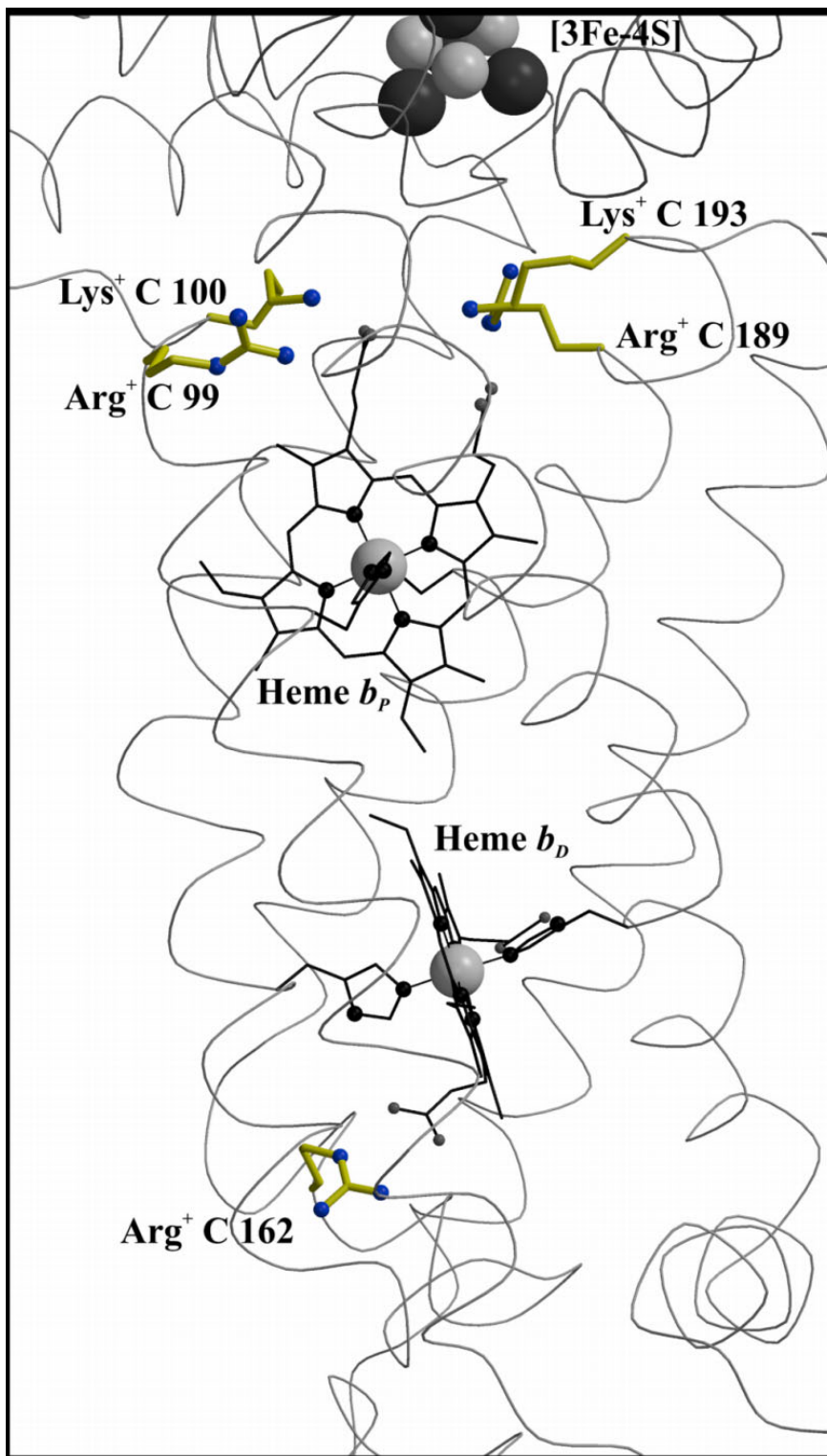


Figure 3.2: Ionized bases interacting with heme b groups of QFR.

The figure shows a detail of the QFR structure, including the positions of the proximal heme b_p and the distal heme b_D and the buried bases (Arg C99, Lys C100, Arg C189, and Lys C193 for b_p , and Arg C162 for b_D , respectively), which are fully ionized in the oxidized state, and thus destabilize the oxidized heme species. The coordinates were taken from PDB entry 1QLA (Lancaster *et al.*, 1999).

An explanation of the total difference in midpoint potential between the high- and low-potential heme requires the addition of all energetic contributions listed in Table 3.1 *A* and *B*. For the oxidized proximal heme, the respective results in part *B*) of Table 3.1 are: $\Delta\Delta G_{rxn} = 4.8$ Δ pK units and $\Delta G_{pol} = -1.0$ Δ pK units, and for the oxidized distal heme: $\Delta\Delta G_{rxn} = 3.4$ Δ pK units and $\Delta G_{pol} = 0.2$ Δ pK units. As mentioned above, the most dominating direct electrostatic interactions ΔG_{crg} with the hemes are listed in Table 3.1 *A*. Yet the sum of many smaller energetic contributions (< 2 Δ pK units) from other interacting conformers not present in Table 3.1 *A* might be of considerable influence. Thus, the sum of all interaction energy terms of the two oxidized hemes has to be calculated individually. In addition, every interaction energy value must be weighted with the product of the occupancies of the respective pair of conformers in the oxidized state at pH 7. The numbers, which were obtained for all mutual interactions ΔG_{crg} , were -0.6 Δ pK units for the proximal and -2.6 Δ pK units for the distal heme. (If only the conformers included in Table 3.1 were taken into account, the respective numbers were -0.1 Δ pK units for the proximal and -3.3 Δ pK units for the distal heme.) Thus, the total sum for the oxidized proximal heme is $\Delta\Delta G_{rxn} + \Delta G_{pol} + \Delta G_{crg} = (4.8 - 1.0 - 0.6 =) 3.2$ Δ pK units, and $\Delta\Delta G_{rxn} + \Delta G_{pol} + \Delta G_{crg} = (3.4 + 0.2 - 2.6 =) 1.0$ Δ pK units for the oxidized distal heme. Hence, the oxidized form of the proximal heme is destabilized by 2.2 Δ pK units more than the oxidized form of the distal heme. This difference in energy corresponds to a difference in potential of 132 mV, which essentially accounts for the midpoint potential difference value of 113 mV found in the simulated redox titration of the hemes (see Figure 3.1). Thus, the consideration of the *oxidized* states alone is sufficient to explain the midpoint potential difference of the proximal and distal heme. The remaining deviation of about 19 mV is due to additional differential contributions of the *reduced* heme species, which have been left aside in the estimation above.

Comparison of the different energy terms for the proximal and distal hemes shows that the oxidized species of the proximal heme b_P is more stabilized than the distal heme group b_D due to permanent polar interactions ΔG_{pol} with the backbone and polar residues. This contribution of ΔG_{pol} partly counterbalances the effect of the desolvation energy $\Delta\Delta G_{rxn}$ and the charge-charge interactions ΔG_{crg} , as both latter terms are more favorable with respect to the oxidized distal heme b_D . Otherwise, the midpoint potential difference of the two heme groups would be even larger than the observed 113 mV.

3.1.4 Nonstandard protonation states of residues in the QFR model at pH 7

Most ionizable residues in the QFR model adopt standard protonation states at pH 7. Only a limited number of protonatable residues were found to adopt nonstandard protonation states in the oxidized state as well as in the other simulated redox states at pH 7. Nonstandard protonation states at pH 7 were considered to be Lys⁰, Arg⁰, His⁺, Asp⁰, Glu⁰, Paa⁰, Pdd⁰, and Tyr⁻. Since most residues are provided with several conformers, it should be noted that the quoted residue occupancies in this paragraph are given for the sum of the occupancies of the conformer fraction, which belongs to a nonstandard protonation state. As a threshold, a value of 5 % was chosen to qualify for significant nonstandard protonation. The following residues of interest in the context of this study (with their occupancies in parentheses) were identified among the entirety of residues in model W in the oxidized state at pH 7: The ring C propionate of the distal heme, called Pdd⁰ X2 (100 %), Glu⁰ C180 (42 %), and Glu⁰ C66 (100 %). Other residues with nonstandard protonation states were His⁺ B128 (60 %), His⁺ B187 (79 %), His⁺ B123 (99 %), His⁺ B22 (64 %), Lys⁰ C213 (53 %), and Lys⁰ C251 (11 %). The only residue quoted here, which will significantly (by more than 5 %) change its protonation state at pH 7 with respect to the other simulated heme redox states, is Glu C180 and will be discussed below in detail.

3.1.5 Simulated heme reduction and its effect on conformer occupancy

As a result of the simulated heme reduction in QFR, the influence of the different heme redox states on the ionization state of the ionizable groups of the enzyme as well as the general contribution of conformers was analyzed. Table 3.2 shows a list of conformers that change their occupancy at pH 7 by more than 5 % in the course of the simulated heme reduction. As for Table 3.1, the conformers are sorted according to their z-coordinate (i.e., the membrane normal).

| Occupancies in states: | | | z-coor- dinate (Å) |
|--|---|--|--------------------------|
| $b_D^{red} b_P^{ox}$ minus $b_D^{ox} b_P^{ox}$ | $b_D^{ox} b_P^{red}$ minus $b_D^{red} b_P^{ox}$ | $b_D^{red} b_P^{red}$ minus $b_D^{ox} b_P^{red}$ | |
| | Arg ⁺ B 167g -0,13 | | -14,5 |
| | Arg ⁺ B 167e 0,13 | | -18,8 |
| Water W 110o -0,06 | Water W 110c -0,06 | | -17,0 |
| | | | -17,0 |
| | Arg ⁺ C 99i -0,08 | | -20,7 |
| | Arg ⁺ C 99f 0,08 | | -23,0 |
| | Water W 131g 0,09 | | -21,6 |
| | Water W 132c -0,07 | | -23,5 |
| | Water W 132e 0,11 | | -23,5 |
| Lys C 213a 0,08 | Lys C 213a -0,14 | | -31,1 |
| Lys ⁺ C 213b -0,08 | Lys ⁺ C 213b 0,14 | | -31,1 |
| | Thr C 33b 0,06 | | -31,5 |
| | Thr C 33c -0,07 | | -31,5 |
| | Thr C 214a 0,05 | | -32,2 |
| | Thr C 214b -0,07 | | -32,2 |
| Water W 11b 0,07 | Water W 11b 0,07 | | -37,8 |
| Water W 11f 0,07 | Water W 11f -0,08 | | -37,8 |
| Water W 33b -0,06 | | | -37,8 |
| Water W 33e -0,06 | | | -37,8 |
| Water W 33f -0,07 | | | -37,8 |
| Glu C 180a 0,10 | | | -39,4 |
| Glu C 180b 0,08 | | | -39,4 |
| Glu C 180c 0,11 | Glu C 180c 0,06 | | -39,4 |
| | Glu C 180e 0,06 | | -39,4 |
| Glu ⁻ C 180k -0,09 | | | -39,4 |
| Glu C 180f 0,20 | Glu C 180f -0,12 | Glu C 180f 0,09 | -41,4 |
| Glu C 180g 0,06 | | | -41,4 |
| Glu ⁻ C 180l -0,49 | Glu ⁻ C 180l 0,07 | Glu ⁻ C 180l -0,07 | -41,4 |
| | Ser C 49c -0,06 | Ser C 49c 0,06 | -51,0 |
| | Thr C 227a -0,06 | Thr C 227a 0,08 | -51,8 |
| | Thr C 227b 0,06 | Thr C 227b -0,08 | -51,8 |
| Ser C 160a -0,07 | Ser C 160a 0,08 | Ser C 160a -0,06 | -60,3 |
| Ser C 160b 0,07 | Ser C 160b -0,07 | Ser C 160b 0,06 | -60,3 |

Table 3.2: Significant occupancy changes between the different modeled heme redox states.

Significant changes of conformer occupancy (> 5 %) at pH 7 were calculated as differences of occupancies: “occupancy in final state” minus “occupancy in initial state”. Conformers are sorted according to descending z-coordinates in Ångstrom (Å).

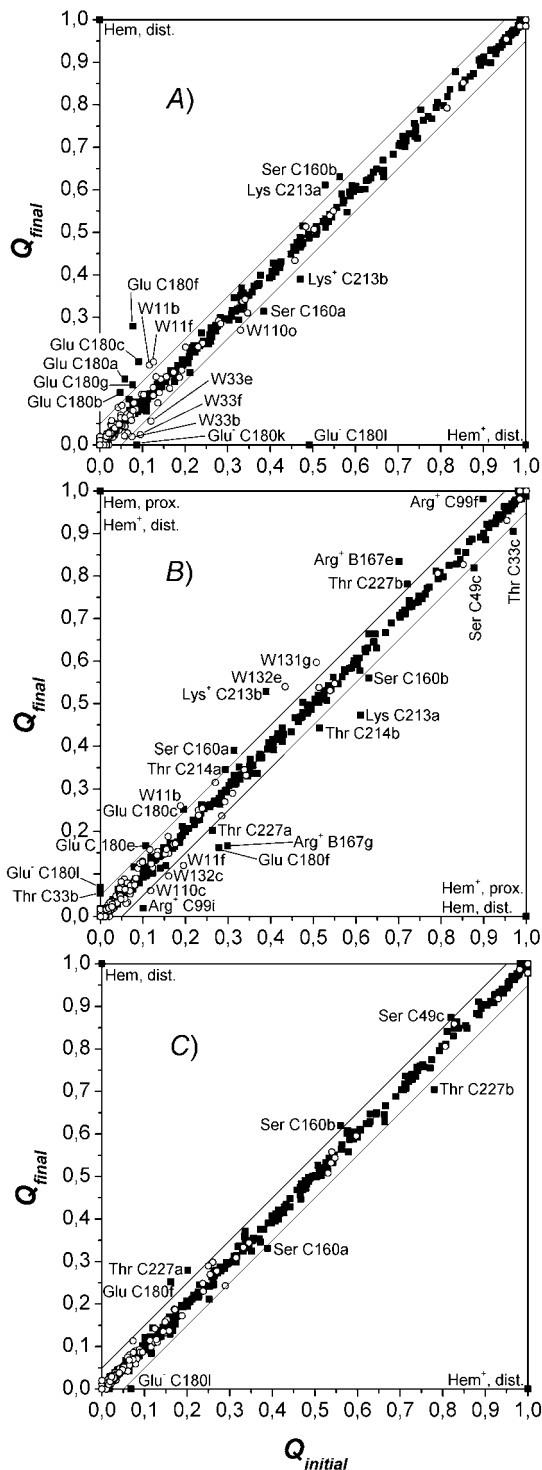


Figure 3.3: Graphical representation of significant occupancy changes.

A—C The figure shows a plot of “occupancy in final state” (Q_{final}) against “occupancy in initial state” ($Q_{initial}$) for all conformers of model W at pH 7. Occupancy deviations by more than 5 % off the diagonal are considered significant, the corresponding conformers are labeled. Conformers represented by points close to the diagonal do not experience significant conformational changes, whereas conformers below the diagonal decrease their occupancy, and conformers above the diagonal raise their occupancy upon the respective electron transfer step. *Black squares* represent protein conformers; *open circles* are water conformers. Abscissa in (A) $Q_{initial} = Q(b_D^{ox} b_P^{ox})$, ordinate in (A) $Q_{final} = Q(b_D^{red} b_P^{ox})$; abscissa in (B) $Q_{initial} = Q(b_D^{red} b_P^{ox})$, ordinate in (B) $Q_{final} = Q(b_D^{ox} b_P^{red})$; abscissa in (C) $Q_{initial} = Q(b_D^{ox} b_P^{red})$, ordinate in (C) $Q_{final} = Q(b_D^{red} b_P^{red})$.

A different way of presenting the results, which are summarized in Table 3.2, is to plot the occupancy of every conformer in a subsequent state against the occupancy of the same conformer in the preceding state (see Figure 3.3). The further an entry is off the diagonal, the greater the change of the respective conformer occupancy was for the considered step. This representation also allows displaying all conformers in one plot.

The adjustment of ionization states as a consequence of the changed redox states is also reflected in a change of the total charge of the QFR model. The sum of all changes gives the total change of charge, but separate contributions can be assigned to individual groups or side chains in the protein. To visualize the obtained results, the difference of the total charge of model W between the four individual redox states of the heme *b* groups (“after” the corresponding step of electron transfer) as a function of pH is shown in Figure 3.4 A–C. The results show that the largest changes of the total charge between the four considered heme redox states occur at intermediate pH values around the maximum at pH 8 (for step 1 and 2, Figure 3.4 A and B) and pH 9 (for step 3, Figure 3.4 C). In order to analyze the origin of the curves, which reflect the change of the total charge of QFR, the contributions of individual residues were checked and the two dominant ones were included in Figure 3.4. The two residues that exhibit the largest changes in ionization state between pH 5 to 11 were identified to be the amino acid residues Glu C180 and Glu C66. The obtained results show that the major contribution to the change of the total charge at physiologically relevant pH values (i.e., around pH 7) is due to amino acid residue Glu C180.

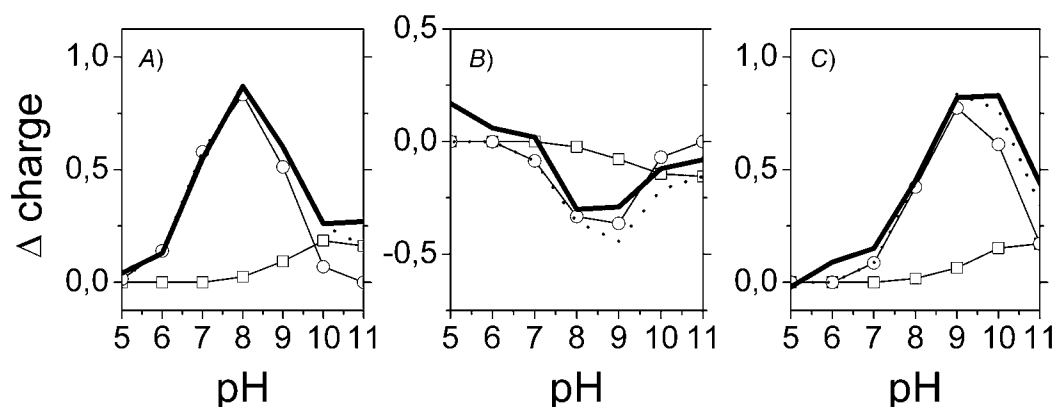


Figure 3.4: Change of the total charge in the course of simulated heme reduction.

A–C Comparison of the change of the total charge of model W (*bold solid line*) as a function of pH for the three considered electron transfer steps with the summed contribution of two individual residues (*bold dotted line*), which are in detail: Glu[−] C66 (*open squares*), and Glu[−] C180 (*open circles*). The data show the sum of the occupancies of the respective deprotonated, charged species. The change of charge in panel (A) is calculated as the difference of the total charge in state $b_D^{red} b_P^{ox}$ minus $b_D^{ox} b_P^{ox}$, in (B) $b_D^{ox} b_P^{red}$ minus $b_D^{red} b_P^{ox}$, and in (C) $b_D^{red} b_P^{red}$ minus $b_D^{ox} b_P^{red}$.

Panel *A* of Figure 3.4 shows that upon reduction of the distal heme, which represents the first step of electron transfer following the oxidized state, Glu C180 contributes strongest between pH 6 and 10. The total charge at pH 7 is increased by +0.55 in units of proton charge, and a comparison with the corresponding result for Glu C180 clearly states that this particular residue is by far the dominating reason for the observed increase. This can be interpreted in terms of a partial proton uptake of Glu C180 upon reduction of the distal heme. A similar behavior is observed for Glu C66, although the relevant contribution only occurs at higher pH values (i.e., above pH values that are of physiological relevance) with a much lower magnitude.

In the second step, depicted in Figure 3.4 *B*, the proximal heme is reduced and the distal heme is re-oxidized. Yet the protonation state of Glu C180 at pH 7 does not change significantly upon electron transfer to the proximal heme.

Upon re-reduction of the distal heme by the second electron (with the proximal heme still being reduced), shown in Figure 3.4 *C*, the protonation state of Glu C180 again does not feature a significant change, i.e., Glu C180 remains protonated at pH 7.

To underline the above findings, the sum of the occupancy changes of the two identified residues, Glu C180 and Glu C66, was compared with the change of total charge, showing that the course of the change of the total charge is well reproduced by the sum of the two residues alone. The protonation state of Glu C180 is substantially increased upon heme reduction, and the residue is predominantly protonated at pH 7 as long as at least one heme group is reduced. The same analysis based on the data obtained with model X exhibits very comparable results, which are shifted to lower pH values by about 1 pH unit (data shown in APPENDIX, Figures 6.2 to 6.4).

3.1.6 Simulated pH titrations of Glu C180 as a function of the heme redox states

Figure 3.5 shows simulated pH titrations of amino acid residue Glu C180 (i.e., the cumulative occupancy of all neutral Glu⁰ C180 conformers) for the different redox states of model W that were considered in this study. In the oxidized state, the pK_a of Glu C180 is lowest with a value of pK_a = 6.9. When the distal heme is reduced, the pK_a increases by 2.1 ΔpK units to pK_a = 9.0. In a second step, the electron is shifted to the proximal heme, which has a comparatively minor effect on the pK_a, shifting it to pK_a = 8.2. Upon re-reduction of the distal heme with the proximal still reduced, the pK_a increases by 2.0 ΔpK units to a value at 10.2. All four quoted pK_a values were obtained by fitting the data points with a simple

Henderson-Hasselbalch equation (see ref. de Levie, 2003 for a recent evaluation of the origin and history of the H.-H. equation). Analysis of the electrostatic interaction energies and respective conformer occupancies in the different modeled redox states directly shows that the main influence on the pK_a of Glu C180 is due to the charge on the heme groups. There are two ionized conformers of Glu C180, namely conformers “k” and “l” of Glu^- C180, which exhibit relevant occupancies and electrostatic interactions with the oxidized heme groups (see Table 3.1). Figure 3.6 shows the position and orientation of the two ionized conformers “k” and “l” of Glu^- C180 together with the two heme groups and the two water molecules (waters W11 and W33) in detail. The electrostatic interaction energy of conformer “k” of Glu^- C180 and the proximal heme b_P is $-1.1 \Delta pK$ units, and $-2.6 \Delta pK$ units for the distal heme b_D (see Table 3.1). The respective interactions for conformer “l” of Glu^- C180 are $-0.9 \Delta pK$ units for the proximal heme b_P , and $-1.2 \Delta pK$ units for the distal heme b_D (see Table 3.1). The quoted interaction energies also explain the observation that the reduction of the distal heme b_D has a slightly stronger influence on the pK_a of Glu C180 than the reduction of the proximal heme b_P (see Figure 3.5).

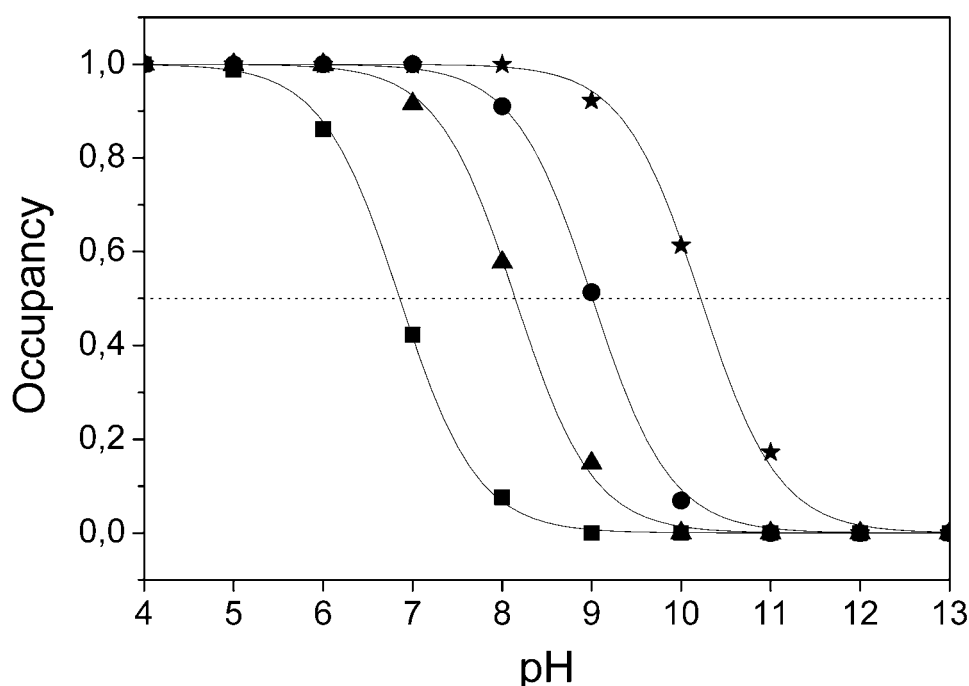


Figure 3.5: The pK_a of Glu C180 depends on the heme redox states.

The pH titration curves of Glu^0 C180 (sum of all neutral conformers) are shown as a function of the four considered heme redox states. *Squares*: both hemes oxidized, *circles*: distal heme reduced, *triangles*: proximal heme reduced, and *stars*: both hemes reduced. The *solid lines* represent fitting curves according to a simple Henderson-Hasselbalch equation. The corresponding pK_a 's are 6.9 in the oxidized state $b_D^{ox} b_P^{ox}$, 9.0 for $b_D^{red} b_P^{ox}$ (distal heme reduced), 8.2 for $b_D^{ox} b_P^{red}$ (proximal heme reduced), and 10.2 for $b_D^{red} b_P^{red}$ (both hemes reduced).

The difference between, for example, the lowest and highest pK_a values (corresponding to the fully oxidized state and the state with both hemes reduced, respectively) is 3.3 pH units. The above stated heme interactions with the two ionized conformers “k” and “l” of Glu⁻ C180 and their respective occupancies yield an energetic difference between the respective redox states of 3.7 ΔpK units, which accounts for almost all of the observed total difference of 3.3 pH units. Again, in the case of model X, a similar behavior is observed but at lower pH values (by approximately 1 pH unit, data shown in APPENDIX, Figures 6.2 to 6.4).

3.1.7 Conformational change of Glu C180 mediated by waters W11 and W33

In addition to the original side-chain orientation of amino acid residue Glu C180, called “intermediate” conformation (corresponding to the orientation of conformer “k”), as it is found in the crystal structure 1QLA of QFR, one other conformation, termed “distal” (corresponding to “l”; see Figure 3.6), was identified to be relevant. The occupancy distribution of all Glu C180 conformers at pH 7 with respect to the two major conformations shows that the reduction of the distal and/or proximal heme favors the “intermediate” over the “distal” conformation.

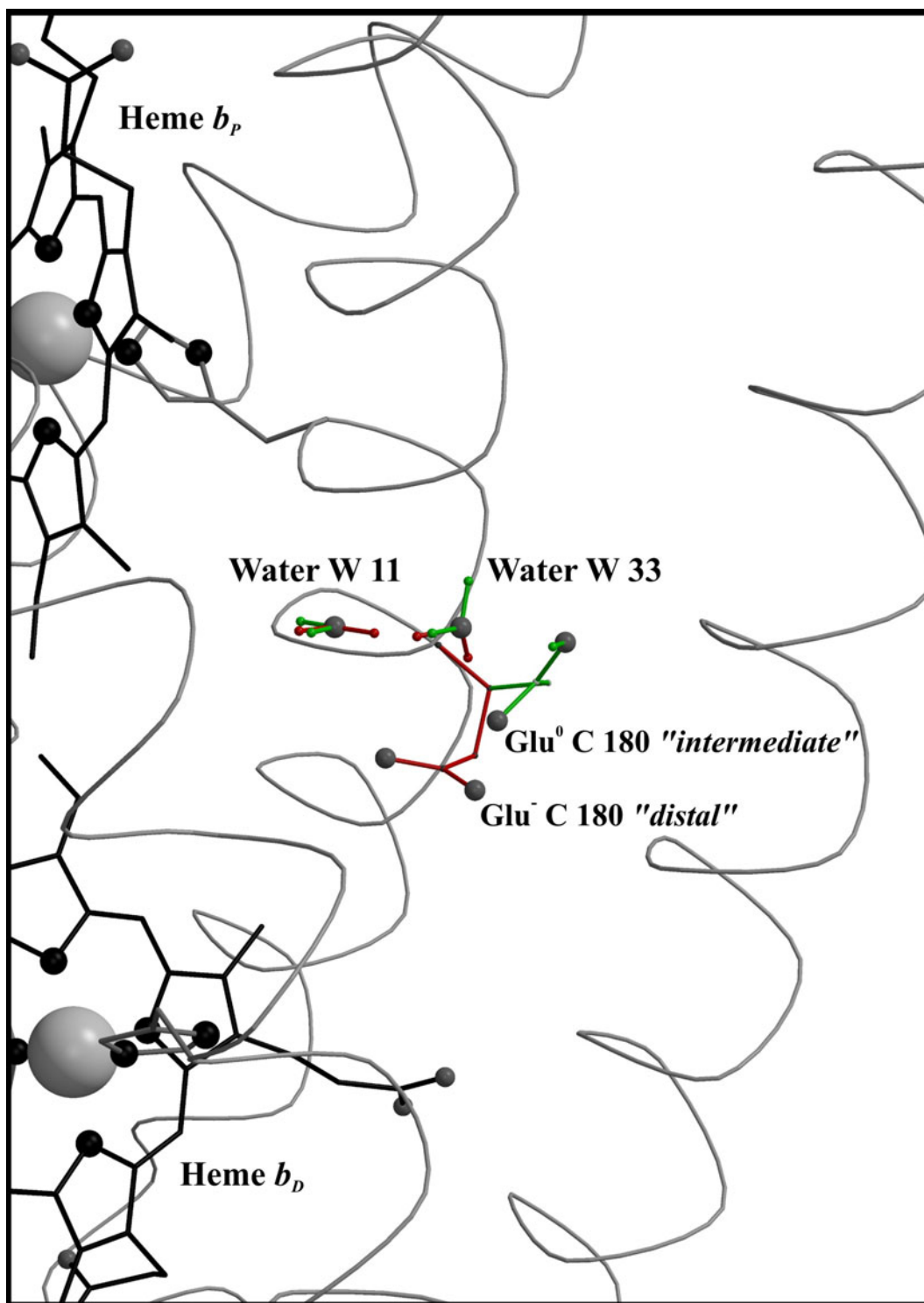


Figure 3.6: Side-chain orientation of Glu C180 in simulated heme reduction.

Conformation "intermediate" (in *green*, corresponding to the orientation of the ionized "k" conformer) and conformation "distal" (in *red*, corresponding to "l") of Glu C180 with respect to the heme groups and the two crystallographic water molecules W11 and W33. The figure also explains the terminology "intermediate" and "distal", since the "intermediate" conformation displays no preference in orientation with respect to the two hemes, whereas the "distal" conformation is oriented towards the distal heme group. *Green color* indicates an increase of occupancy upon first step of electron transfer; *red* indicates a decrease. For each of the waters, the two conformers, which undergo the strongest increase and decrease, respectively, in occupancy, are depicted exemplarily.

Figure 3.7 shows the sum of occupancies of all Glu C180 conformers, which are either in the “intermediate” or “distal” conformation, irrespective of the protonation state of the conformers, as a function of the modeled heme redox states. To complement this, Figure 3.7 also shows the progression of the protonation state of Glu C180, i.e., the sum of all protonated and deprotonated conformers, respectively. Upon reduction of the distal heme, the occupancy of the “intermediate” conformation increases at the expense of the “distal” from 0.35 to 0.58. The conformational change upon reduction of the distal heme is accompanied by proton uptake of Glu C180, and the residue remains strongly protonated during the subsequent electron transfer steps as long as the heme groups are reduced.

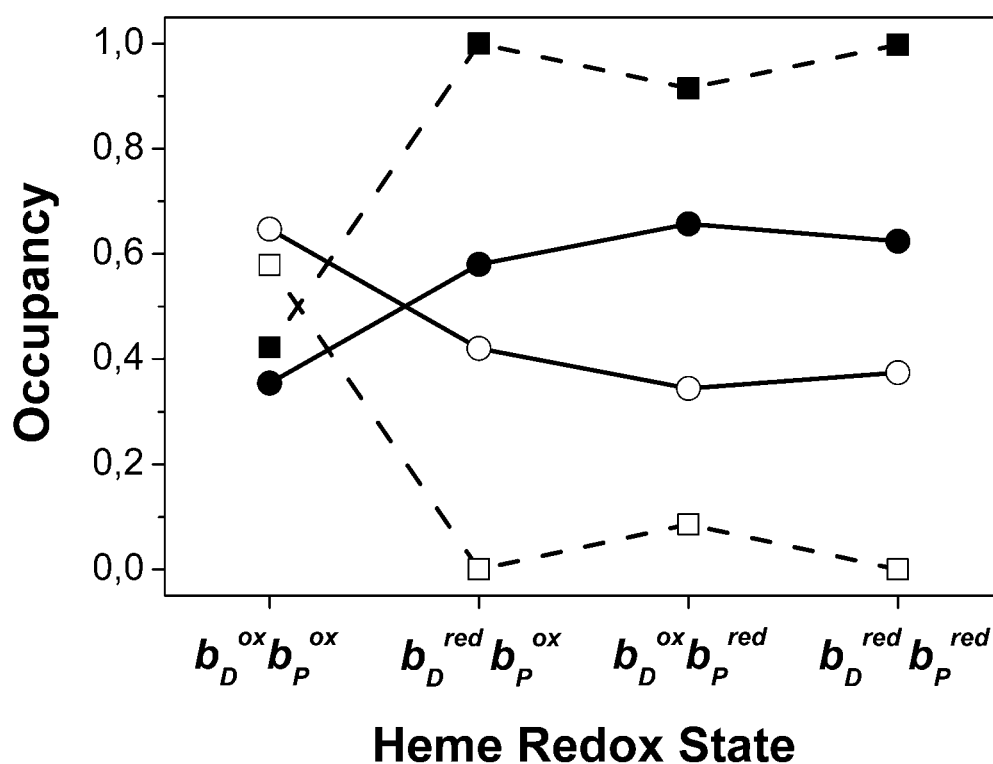


Figure 3.7: Conformational change of Glu C180.

Summed occupancies of all conformers in the conformation “intermediate” (*full circles*) and “distal” (*open circles*), and summed occupancies of all protonated (*full squares*) and deprotonated (*open squares*) conformers at pH 7 as a function of the heme *b* redox state.

In the case of model X, there is no such effect to be detected as described above (see APPENDIX, Fig. 6.4), suggesting that the observed conformation change of Glu C180 is mediated by the water molecules W11 and W33 in the vicinity of the side chain (see Figure 3.6). The two water molecules are provided with several conformers (8 for W11 and 15 for W33), but only three conformers of W33 meet the criteria to be listed in Table 3.1 (all interactions of W11 with Glu C180 conformers are below ± 1 ΔpK unit). Just like Glu C180,

water molecules W11 and W33 undergo an alternation of their orientation with respect to the reduction of heme b_D . This is exemplified in Figure 3.6 for the first step of electron transfer.

3.2 FTIR and VIS Spectroscopy

Electrochemically induced FTIR difference spectroscopy was employed in this study to investigate the QFR from *W. succinogenes* with respect to coupled electron and proton transfer in the context of the proposed “E-pathway” hypothesis. The wild-type (WT) and particularly enzyme variant Glu C180 → Gln (abbreviated E180Q) were analyzed. Two additional variants, Glu C66 → Gln (E66Q), and Glu A270 → Gln (E270Q), were included in the study for comparison.

The largest difference signals observed in the presented study are of the order of 0.3 % to 0.5 % of the total IR absorption (approximately 1 OD at 1648 cm⁻¹), while the smallest difference signals that can be resolved (i.e., the tentative $\nu(\text{COOH})$ stretching vibrations) are of the order of approximately 0.01 % or even less. This high sensitivity can be achieved since the different protein states are electrochemically adjusted in the infrared cuvette using the same sample.

The results presented here concentrate on the role of amino acid residue Glu C180 and the heme *b* groups, *b_D* and *b_P*, and their propionates in the catalytic mechanism of *W. succinogenes* QFR. It has been the aim of this study to clarify the possible involvement of these particular groups in the coupling of transmembrane electron and proton transfer as it has been suggested in the context of the “E-pathway” hypothesis.

3.2.1 FTIR on QFR WT and enzyme variants

3.2.1.1 Electrochemically induced IR and VIS difference spectra

An important criterion for the quality of the induced redox reaction and the associated difference spectra is their reversibility. In our experiments, all induced redox processes appear to be fully reversible under the applied experimental conditions, since all collected difference spectra (for WT and variant enzymes) are completely symmetrical over the entire spectral range (symmetrical in the sense that exchanging final and initial state in the experiment results in a sign change of the accompanying difference spectrum; see Figure 3.8). This statement also includes the redox behavior of the two heme *b* groups of QFR, as shown in the inset of Figure 3.8a, which shows an “oxidized-minus-reduced” as well as the respective symmetrical “reduced-minus-oxidized” difference spectrum in the VIS range. The

peak/trough feature at 411 nm/428 nm (which is associated with the Soret-band) and the peak at 561 nm (which is associated with the α -band) directly reflect the redox dependency of the VIS absorption spectra of the heme *b* groups. By recording difference spectra at intermediate redox potentials between the reduced and oxidized state and plotting the absorbance changes of the Soret and α -band against the applied external electrode potential (Moss *et al.*, 1990), the midpoint potentials of the two heme *b* groups of QFR from *W. succinogenes* could be determined in this study (see also ref. Lancaster *et al.*, 2000). Because of the reversibility, oxidative and reductive titrations of the hemes yield the same values for the two heme midpoint potentials and no hysteresis was observed.

In the IR spectral range, data of QFR were recorded up to 1800 cm^{-1} , but there were no observable signals above $\sim 1750\text{ cm}^{-1}$ independent of the applied electrode potential and pH. The obtained “oxidized-minus-reduced” (and vice versa: “reduced-minus-oxidized”) difference spectra revealed numerous contributions in the entire spectral range between 1750 cm^{-1} and 1000 cm^{-1} . Figure 3.8 a–d shows electrochemically induced FTIR difference spectra of WT QFR, and the three variant enzymes (i.e., E66Q, E270Q, and E180Q) in aqueous KP_i -buffer at pH 7.

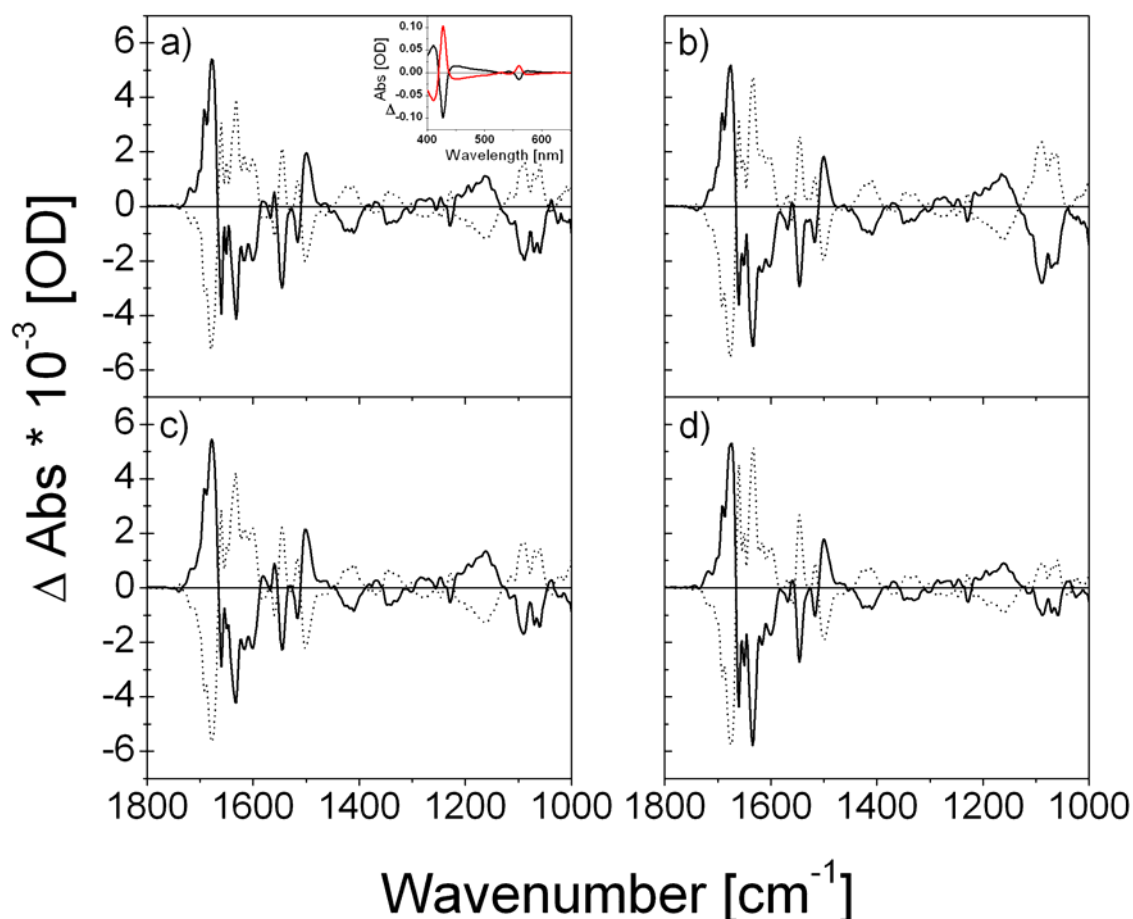


Figure 3.8: Electrochemically induced FTIR difference spectra in the mid-IR range.

Reversible “oxidized-minus-reduced” (*solid line*) and “reduced-minus-oxidized” (*dashed line*) FTIR difference spectra of QFR WT at pH 7, a); enzyme variant E66Q at pH 7, b); enzyme variant E270Q at pH 7, c); and enzyme variant E180Q at pH 7, d). Reference electrode potentials for the shown FTIR difference spectra were +0.21 V (full oxidative potential) and −0.37 V (full reductive potential). Positive bands belong to the final state, negative ones to the initial state. In a “reduced-minus-oxidized” difference spectrum all positive bands belong to the reduced state while all negative bands belong to the oxidized state (and vice versa). The inset of panel a) shows the corresponding VIS difference spectra of QFR WT at pH 7 (the *red solid curve* corresponds to a “reduced-minus-oxidized” difference spectrum, *black solid curve*: vice versa). The heme difference band associated with the Soret-band is located at 411 nm/428 nm and the respective one for the α -band at 561 nm.

All presented spectra were normalized to a level that represents the average maximal absorbance difference (ΔAbs) in the amide I range of all difference spectra that have been selected for presentation. Since the amplitude ratios of individual pairs of difference bands are not perfectly conserved in independent experiments (measuring the same type of enzyme, i.e., WT or a specific variant, at the same pH and reference potentials), scaling of the difference spectra for comparison is not straightforward but always a compromise, as it cannot satisfactorily be achieved on the basis of a single difference band. This applies as well for the heme difference bands in the VIS range, as the ratio of the difference bands originating from the Soret- and α -band, respectively, is not constant in all experiments. Thus, the scaling was

performed on the basis of the large absorbance changes in the amide I region as it has been done in other studies (e.g., Rich & Breton, 2001; Lübben *et al.*, 1999; and Foerstendorf *et al.*, 1996). The deviations between the different spectra are small compared to the overall absorbance differences and might be related to the individual protein concentration, sample layer thickness, and slightly different mediator concentration in the particular experiment.

The signal pattern in the region around 1648 cm^{-1} appears to be hardly affected by the strong water absorbance (see Figure 3.8 a–d), although an elevated noise level around 1648 cm^{-1} is inevitable (see APPENDIX, Figures 6.6 and 6.7). Yet the observed bands in the difference spectra in the amide I range are comparatively narrow and well reproducible. Thus, it is unlikely that the difference signals around 1648 cm^{-1} are not initiated by redox dependent absorbance changes of the QFR sample. In D_2O , the respective region of increased noise (i.e., the region of the D-O-D bending mode) can be found at around 1210 cm^{-1} in the IR absorbance spectrum (data shown in APPENDIX, Fig. 6.8).

3.2.1.2 Contributions of the amide I band and secondary structure elements

The most prominent spectral feature that can be observed for all investigated QFR samples (i.e., WT, E66Q, E270Q, and E180Q) in H_2O and D_2O buffer, is a series of large well-pronounced positive and negative bands between approximately 1700 cm^{-1} and 1475 cm^{-1} (see Figure 3.8 and Figure 3.9). For the basic assignment of IR bands, the spectral regions in which contributions of the protein are expected have to be considered. In the investigated IR range between 1800 cm^{-1} and 1000 cm^{-1} the amide I mode (primarily C=O stretching vibrations) of QFR contributes between approximately 1690 cm^{-1} and 1615 cm^{-1} and peaks at 1656 cm^{-1} (IR absorbance spectrum shown in APPENDIX, Fig. 6.8), which is indicative of predominantly α -helical secondary structure elements (Barth & Zscherp, 2002). The strong difference bands, especially at 1678 cm^{-1} and 1632 cm^{-1} , in the amide I region can be assigned to vibrations of the polypeptide backbone, and thus those difference bands indicate local structural reorganizations of the protein, which are triggered by the induced redox reaction (Mäntele, 1993). The positions of the two mentioned bands are indicative of turns and β -sheets (1678 cm^{-1}), and β -sheets (1632 cm^{-1}), see ref. (Barth & Zscherp, 2002).

3.2.1.3 Contributions of the amide II and III bands

Furthermore, the amide II mode (a combination of N–H bending and C–N stretching modes) is located between roughly 1580 cm^{-1} and 1510 cm^{-1} and peaks at 1550 cm^{-1} (data shown in APPENDIX, Fig. 6.8). The observed positions of the amide bands agree very well with values quoted in the literature (see for instance ref. Mäntele, 1996).

Signals originating from amide III contributions are expected between approximately 1400 cm^{-1} and 1200 cm^{-1} , and the respective modes are a superposition of C–N stretching and N–H bending with small contributions of C–C stretching and C–O in-plane bending vibrations (Barth & Zscherp, 2002).

The series of dominating difference bands mentioned above, which are depicted in Figure 3.8, lie well within the range of the amide I and amide II modes of the protein.

3.2.1.4 Effects of $^1\text{H}/^2\text{H}$ isotope exchange

Figure 3.9 shows that there are considerable differences between spectra taken in H_2O and in D_2O buffer due to the $^1\text{H}/^2\text{H}$ isotope exchange. The spectral differences, which are visible in Figure 3.9 for the QFR WT enzyme, are also found in the respective difference spectra of the variant enzymes in D_2O (data shown in APPENDIX, Figures 6.10 and 6.11).

Upon $^1\text{H}/^2\text{H}$ isotope exchange the difference spectra of QFR show pronounced deviations compared to the spectra in H_2O buffer (see Figure 3.9). In the amide I range, the sharp band at 1660 cm^{-1} in the reduced state decreases in amplitude upon $^1\text{H}/^2\text{H}$ exchange, and the small band at 1650 cm^{-1} increases. The two biggest bands in the difference spectra at 1678 cm^{-1} (oxidized state) and 1632 cm^{-1} (reduced state) are nearly unaffected by the isotope exchange, which is not unusual for amide I difference bands (Barth & Zscherp, 2002). Another pair of bands at 1617 cm^{-1} and 1601 cm^{-1} in the reduced state shows a decreased intensity in D_2O . Alternatively, an underlying band might be shifted to lower wavenumbers in D_2O . This could be due to Gln $\delta(\text{NH}_2)$ vibrations, which are expected between 1610 cm^{-1} and 1586 cm^{-1} in H_2O and which exhibit dramatic shifts to lower frequencies upon deuteration (to as much as 1163 cm^{-1} ; see Barth, 2000 and refs. therein).

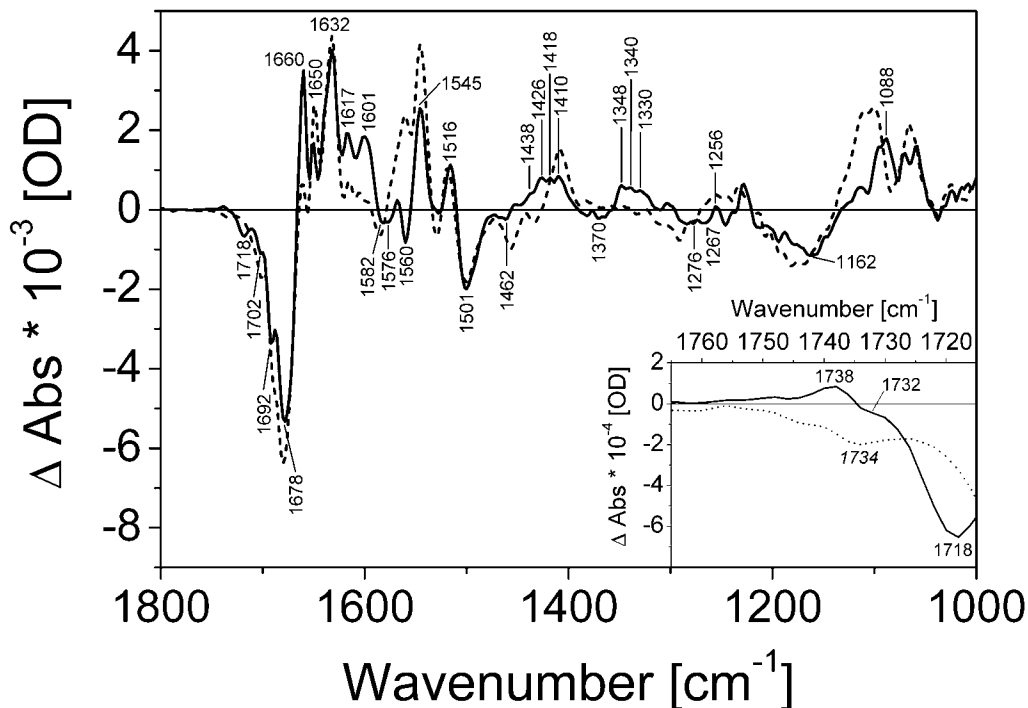


Figure 3.9: Electrochemically induced FTIR difference spectra of QFR WT in H₂O and D₂O.

The figure shows “Reduced-minus-oxidized” FTIR difference spectra of QFR WT at pH 7 (*solid line*) and at an observed pH_{obs} of 7 (which corresponds to pD 7.4; *dashed line*). The inset shows the same data in the wavenumber range from 1765 cm^{-1} to 1715 cm^{-1} . Reference electrode potentials for the shown FTIR difference spectra were +0.21 V (full oxidative potential) and -0.37 V (full reductive potential). The wavenumbers of the bands in H₂O are the same as assigned in the text, and they are indicated in the figure; the number in *italics*, which is visible in the inset, corresponds to the band position in D₂O.

Also the spectral features in the amide II range exhibit distinct alterations upon $^1\text{H}/^2\text{H}$ exchange. Genuine amide II vibrations should experience a drastic downshift upon deuteration, since the N- ^2H bending and C-N stretching modes are uncoupled. But such a downshift is not observed for QFR. In fact, the signal amplitudes in the reduced state increase upon deuteration. Thus, it is unlikely that the observed difference signals in the amide II region are due to genuine amide II vibrations.

A pronounced positive difference band appears in D₂O at 1560 cm^{-1} in the reduced state, where a small derivative-shaped feature is found in H₂O buffer. The difference band at 1545 cm^{-1} has drastically increased its amplitude in D₂O (alternatively, another band is shifted to this position in D₂O and adds to the intensity). Another small band in the region of the amide II band is found at roughly 1529 cm^{-1} in D₂O in the oxidized state, which is only weakly pronounced in H₂O.

Below 1490 cm^{-1} , the spectra show further subtle but reproducible differences between data obtained in H₂O and D₂O buffer, respectively. A negative difference band is present in

D₂O at 1456 cm⁻¹ in the “reduced-minus-oxidized” difference spectrum (see Figure 3.9), which is not found in H₂O. The most dominant deviation in this region (in terms of signal amplitude and sharpness of the band) is the increase of a positive difference band located at 1409 cm⁻¹ in D₂O. This might be due to the contribution of a signal in H₂O at 1427 cm⁻¹ or 1456 cm⁻¹, which is shifted to 1409 cm⁻¹ upon ¹H/²H exchange.

3.2.1.5 Contributions of the potassium phosphate buffer

Below 1200 cm⁻¹, the main spectral contributions are two broad bands with maximum intensity at 1162 cm⁻¹/1088 cm⁻¹ (see Figure 3.8), which are caused by the potassium phosphate buffer. The difference signals originate from PO modes of the deprotonated phosphate buffer, which reflect proton uptake of the protein (this might also include redox-induced protonation changes of the FAD prosthetic group of QFR or enzyme-bound quinone molecules) as well as proton uptake of the mediator molecules in the course of the redox reaction (Hellwig *et al.*, 1996 and 1999c; and Baymann *et al.*, 1999). In ref. (Hellwig *et al.*, 1999c), a shift of the mentioned buffer bands towards higher wavenumbers (22 cm⁻¹ for the band at 1160 cm⁻¹ and 10 cm⁻¹ for the one at 1088 cm⁻¹) upon ¹H/²H isotope exchange could be observed, which was attributed to a changed hydrogen-bonding strength to the contributing groups after ¹H/²H exchange. For the measurements on QFR enzyme, similar effects could be ascertained (see Figure 3.9).

3.2.1.6 Contributions of the FAD/FADH₂ couple

Several of the observed difference bands in the spectra could be related to the covalently bound FAD prosthetic group. In recent studies (Hellwig *et al.*, 2000; and Wille *et al.*, 2003), FAD in solution and bound to different flavoproteins has been investigated using the same technique of electrochemically induced FTIR difference spectroscopy; and a difference band at 1716 cm⁻¹ has been assigned to a FAD carbonyl $\nu(\text{C}_4=\text{O})$ vibration in the oxidized state.

In the case of QFR, a comparable signal is found at 1718 cm⁻¹ in the oxidized state of the enzyme (see Figure 3.8a and inset of Figure 3.9). In D₂O, the respective vibration is shifted to a lower frequency by approximately 10 cm⁻¹ as expected. The precise position is hard to define as the band merges with the flank of the strong difference signal in the amide I range (see Figure 3.9). Presently, this assignment is tentative and it cannot be ruled out that

the observed signal at 1718 cm^{-1} is due to protonated Asp or Glu side chains. Other contributions of FAD carbonyls are expected but they should be strongly obscured by the large difference signal in the amide I range.

Further FAD contributions of $\nu(\text{C}=\text{N})$ modes are expected between approximately 1600 cm^{-1} and 1530 cm^{-1} (Hellwig *et al.*, 2000; and Wille *et al.*, 2003). For QFR, various signals are found in this frequency range (see Figure 3.8), but since this range coincides with the amide II region, heme signals and contributions from individual amino acids (e.g., ionized Glu or Asp), tentative FAD signals cannot readily be identified at present. A strong signal of the neutral flavin in the oxidized state at 1550 cm^{-1} in free flavin (FMN) in solution, and at 1548 cm^{-1} in a NADH dehydrogenase fragment was assigned to a $\nu(\text{C}=\text{C})$ vibration (Hellwig *et al.*, 2000). In reference (Wille *et al.*, 2003), an analogous signal (of FAD in solution) in the oxidized state at 1548 cm^{-1} was assigned to a $\nu(\text{C}_{10a}=\text{N}_1)$ vibration. In the reduced-minus-oxidized FTIR difference spectrum of QFR WT (see Figure 3.9), no such signal is observed in the oxidized state. Instead, a difference signal at 1545 cm^{-1} , which is associated with the reduced state, is present. Although it cannot be ruled out that this signal is related to the quoted flavin $\nu(\text{C}=\text{C})$ vibration, this assignment seems to be unlikely since the respective signal in QFR WT is related to the reduced redox state of the enzyme. Alternatively, this signal can tentatively be attributed to a heme vibration (see below).

Another possible candidate for a FAD signal is the band at 1516 cm^{-1} , which can be observed in QFR enzyme types in the reduced state (see Figure 3.8). A similar spectral feature (at 1520 cm^{-1} for solvated FAD and between 1516 cm^{-1} and 1514 cm^{-1} in the protein-bound state; Wille *et al.*, 2003) was observed in the reduced state of FAD and was assigned to hydrogen in-plane bending motions of $\delta(\text{C}_6\text{-H})$ and $\delta(\text{C}_9\text{-H})$, and of $\delta(\text{N}_5\text{-H})$ and $\delta(\text{N}_1\text{-H})$ (Wille *et al.*, 2003). The latter pair of vibrations should be sensitive to $^1\text{H}/^2\text{H}$ isotope exchange, but the observed bands hardly change position upon deuteration. Thus, it was suggested that only the former pair is contributing to the observed signal; see ref. (Wille *et al.*, 2003). Also in the case of QFR, the band at 1516 cm^{-1} does not show pronounced $^1\text{H}/^2\text{H}$ exchange sensitivity. Alternatively, the discussed band could be related to Tyr or heme *b* vibrations (see below).

Furthermore, numerous contributions of ring modes of the isoalloxazine system of FAD are expected between approximately 1460 cm^{-1} and 1200 cm^{-1} for the reduced and oxidized states of FAD (Hellwig *et al.*, 2000). Corresponding signals are found in QFR but cannot be assigned unequivocally at present.

3.2.1.7 Contributions of the iron-sulfur clusters

The iron-sulfur clusters are not directly contributing to the IR signals in the discussed mid-infrared range since the involved atomic masses are too large. Instead, the corresponding vibrations contribute below 1000 cm^{-1} (Baymann *et al.*, 1999). Only indirect effects due to the protein environment are to be expected upon redox changes of the three iron-sulfur clusters of QFR enzyme.

3.2.1.8 Contributions of the heme *b* groups and their propionates

A multitude of heme vibrations, which partly overlap with the amide I, II and III regions, have been observed and assigned in many FTIR and Raman studies for the heme porphyrin ring, substituents, and propionates. Also in the case of QFR, the two heme *b* groups are expected to show significant contributions to the FTIR difference spectra, which reflect the induced redox-state changes of the hemes.

Protonated heme propionates, which might be of functional importance with respect to redox-coupled proton transfer within the QFR enzyme, are expected to contribute between 1700 cm^{-1} and 1665 cm^{-1} (Behr *et al.*, 1998). This region overlaps with the amide I vibrations and is dominated by the large negative difference signal at 1678 cm^{-1} (see Figure 3.9), which makes it difficult to assign tentative contributions of any protonated heme propionates. The small shoulders at 1692 cm^{-1} and 1702 cm^{-1} might reflect heme propionate protonation changes, but the shoulders are also present in D_2O at almost the same position, and the respective vibration should be $^1\text{H}/^2\text{H}$ sensitive. The deprotonated forms of the propionates exhibit antisymmetric $\nu_{\text{as}}(\text{COO}^-)$ vibrations (between 1620 cm^{-1} and 1540 cm^{-1}) and symmetric $\nu_{\text{s}}(\text{COO}^-)$ vibrations (between 1420 cm^{-1} and 1300 cm^{-1} ; Behr *et al.*, 1998). Tentative assignments of heme propionate bands are complicated since ionized Asp or Glu side chain contributions are expected at comparable frequencies (Venyaminov & Kalnin, 1990). QFR enzyme exhibits various signals in the respective regions, and the small signals in the oxidized state at 1560 cm^{-1} and around 1370 cm^{-1} are conceivable $\nu_{\text{as}}(\text{COO}^-)$ and $\nu_{\text{s}}(\text{COO}^-)$ heme propionate signals (see also chapter 3.2.2. and Fig. 1.7).

The strong absorbance at 1545 cm^{-1} in H_2O (1546 cm^{-1} in D_2O) in the reduced state (see Figure 3.9) is tentatively assigned to $\nu(\text{C}_b\text{C}_b)$, with labeling of the heme *b* atoms as in Fig. 1.8, and/or antisymmetric $\nu_{\text{as}}(\text{C}_a\text{C}_m)$ porphyrin modes of the heme *b* groups (Li *et al.*, 1990; and Berthomieu *et al.*, 1992). The band does not shift upon deuteration as expected for

this assignment (Berthomieu *et al.*, 1992), and the strong increase in intensity is probably due to an additional contribution at this frequency in D₂O. A corresponding symmetric mode to $\nu_{\text{as}}(\text{C}_a\text{C}_m)$, namely $\nu_{\text{s}}(\text{C}_a\text{C}_m)$, is expected between 1486 cm⁻¹ and 1458 cm⁻¹ (Li *et al.*, 1990; and Berthomieu *et al.*, 1992). The “reduced-minus-oxidized” difference spectrum of QFR enzyme features a small signal in the oxidized state at 1462 cm⁻¹ in H₂O, which might be obscured in D₂O by a stronger contribution at 1456 cm⁻¹ (possibly a shifted amide II vibration).

The $\nu(\text{C}_a\text{C}_b)$ vibration is expected in an adjacent frequency region between 1450 cm⁻¹ and 1435 cm⁻¹ (Hellwig *et al.*, 1999d). In the respective range in the QFR difference spectrum, a small shoulder is present in the reduced state around 1438 cm⁻¹, which is lost in D₂O (again, possibly due to a shifted amide II vibration).

Below 1400 cm⁻¹, two further significant heme porphyrin vibrations are expected: The $\nu(\text{C}_a\text{N})$ vibration between 1390 cm⁻¹ and 1320 cm⁻¹ (Hellwig *et al.*, 1999d), and the $\delta(\text{C}_m\text{H})$ mode between 1270 cm⁻¹ and 1150 cm⁻¹ (Berthomieu *et al.*, 1992). The QFR difference spectra exhibit small contributions of the oxidized state between 1390 cm⁻¹ and 1358 cm⁻¹ and of the reduced state between 1356 cm⁻¹ and 1312 cm⁻¹. Also the region below 1270 cm⁻¹ shows several bands belonging to either the reduced or oxidized state. But all contributions below 1400 cm⁻¹ are altered upon deuteration. Thus, an assignment to the respective heme vibrations is by no means unequivocal, and additional non-heme vibrations such as amide III, FAD, quinone, and several amino acid vibrations also have to be considered.

Finally, signals from the heme substituents are expected: The small positive band at 1615 cm⁻¹ in D₂O (see Figure 3.9) might be assigned to a heme vinyl $\nu(\text{C}_\alpha=\text{C}_\beta)$ stretching vibration in the reduced state (Schlereth & Mäntele, 1992; and Berthomieu *et al.*, 1992). In H₂O, the corresponding band is observed at 1617 cm⁻¹, but with a much higher intensity. This could indicate an additional contribution at this frequency, which is shifted to lower wavenumbers in D₂O (such as the Gln $\delta(\text{NH}_2)$ vibration mentioned above), or a decrease in extinction coefficient upon deuteration.

3.2.1.9 Contributions of quinones

The quinone content of a quinone-binding membrane protein largely depends on the individual sample preparation (see for example Sinning, 1989; Zhang *et al.*, 2002; and Ritter *et al.*, 2003). The QFR WT samples, which were used for the presented experiments, contained approximately 0.2 menaquinone (and/or methyl-menaquinone) molecules per QFR

monomer (Mileni, M., and Lancaster, C. R. D., *unpublished*). Yet, no distinct quinone signals could be identified in the redox-induced FTIR difference spectra. In principle, the strong difference signal around 1680 cm^{-1} and below in the amide I range could include significant $\nu(\text{C}=\text{O})$ and $\nu(\text{C}=\text{C})$ vibrations of the bound quinones in the oxidized state, but the obtained difference spectra of QFR lack the characteristic contributions of the menaquinone anion in the reduced state between approximately 1490 cm^{-1} and 1390 cm^{-1} , which presumably arise from coupled C—O and C—C modes (Breton *et al.*, 1991a, 1995 and 1996; and Brudler *et al.*, 1995) and which are found, for example, in light-induced Q_A^-/Q_A FTIR difference spectra of bacterial photosynthetic reaction centers (RC) with menaquinone as primary electron acceptor (see for instance ref. Breton *et al.*, 1991b). On the other hand, the quinone contributions do not necessarily appear as clearly in the FTIR difference spectra as in the case of the RCs. An example is found in (Zhang *et al.*, 2002), where a quinone binding cytochrome *bd* from *Escherichia coli* was investigated with electrochemically induced FTIR difference spectroscopy; this enzyme contains considerable amounts of menaquinone when expressed anaerobically. Thus, for a clear assignment of quinone vibrations in QFR, it would be necessary to do further measurements with enhanced quinone content of QFR and/or with labeled quinone molecules.

3.2.1.10 Contributions of the amino acid residues

The difference signals which are indicative of protonated Glu or Asp side chains appear above 1710 cm^{-1} in H_2O buffer (see Figure 3.10), and they are shifted to lower wavenumbers in D_2O buffer (see inset of Figure 3.9) as expected for this assignment (Venyaminov & Kalnin, 1990). Hence, upon $^1\text{H}/^2\text{H}$ isotope exchange, the signals begin to strongly overlap with the large difference band in the amide I region (see inset of Figure 3.9). The respective vibrations of the ionized forms of Asp and Glu are expected between 1580 cm^{-1} and 1560 cm^{-1} for the antisymmetric and between 1420 cm^{-1} and 1400 cm^{-1} for the symmetric mode (Venyaminov & Kalnin, 1990). In QFR, tentative Glu or Asp $\nu_{\text{as}}(\text{COO}^-)$ signals are found in the oxidized state at 1582 , 1576 and 1560 cm^{-1} in H_2O , and at 1585 cm^{-1} in D_2O . In the range of the symmetric $\nu_{\text{s}}(\text{COO}^-)$ mode in the “reduced-minus-oxidized” difference spectrum, only positive contributions are found in both buffer types. In principle, the symmetric modes should exhibit the same sign as the corresponding antisymmetric vibrations if a particular acidic group undergoes a redox-induced protonation change. On the

other hand, it cannot be ruled out that a specific vibration is canceled out by a different one of opposite sign.

Amino acid vibrations, which contribute in the amide I region, are Asn and Gln side chain vibrations. The sharp band observed in the reduced state at 1660 cm^{-1} in H_2O and at 1649 cm^{-1} in D_2O can tentatively be assigned to a Gln $\nu(\text{C}=\text{O})$ mode (cf. ref. Barth & Zscherp, 2002 and refs. therein). Also symmetric (1695 cm^{-1} to 1652 cm^{-1}) and antisymmetric (1663 cm^{-1} to 1614 cm^{-1}) Arg $\nu(\text{CN}_3\text{H}_5^+)$ vibrations can be expected in the amide I range (Barth & Zscherp, 2002). Since the respective vibrations are $^1\text{H}/^2\text{H}$ sensitive, Arg contributions could also be responsible for the differences observed in H_2O and D_2O in the QFR difference spectra in the amide I range and down to approximately 1585 cm^{-1} . Contributions of Arg vibrations could indicate electrostatic interactions between Arg residues and the heme *b* propionates (Berthomieu *et al.*, 1992). This is in line with the results from MCCE calculations on QFR (see chapter 3.1.2).

The strongest difference signal outside the amide I/II region in the “reduced-minus-oxidized” difference spectrum is the derivative-shaped pair of difference bands at $1516\text{ cm}^{-1}/1501\text{ cm}^{-1}$ in H_2O and $1519\text{ cm}^{-1}/1500\text{ cm}^{-1}$ in D_2O (see Figure 3.9). This spectral feature at 1516 cm^{-1} can tentatively be assigned to ring vibrations of protonated tyrosines (Tyr–OH; $\nu(\text{CC})$, $\delta(\text{CH})$) in the reduced state, and the signal at 1501 cm^{-1} in the oxidized state to the corresponding deprotonated Tyr ring vibrations (Tyr–O⁻; $\nu(\text{CC})$, $\delta(\text{CH})$; Venyaminov & Kalnin, 1990). The assignment is supported by the position of the respective vibrations in D_2O , which is barely shifted (see Figure 3.9). In addition, a small shoulder in the IR absorbance spectrum at 1516 cm^{-1} is observed in H_2O and D_2O (data shown in APPENDIX, Fig. 6.8). A similar signal in the IR absorbance and redox-induced FTIR difference spectrum of horse cytochrome *c* has been assigned to a Tyr residue (Moss *et al.*, 1990).

The two assigned tyrosine vibrations are accompanied by a series of related vibrations (summarized in ref. Barth & Zscherp, 2002). Additional smaller bands are expected for protonated tyrosines between 1621 cm^{-1} and 1614 cm^{-1} (Tyr–OH; $\nu(\text{CC})$, $\delta(\text{CH})$) and between 1602 cm^{-1} and 1594 cm^{-1} (Tyr–OH; $\nu(\text{CC})$). The QFR WT difference spectrum in the reduced state shows contributions at 1617 cm^{-1} and 1601 cm^{-1} in H_2O and at 1615 cm^{-1} , 1605 cm^{-1} , and 1597 cm^{-1} in D_2O . Another vibration of the neutral form is expected between 1270 cm^{-1} and 1235 cm^{-1} (Tyr–OH; $\nu(\text{C}-\text{O})$, $\nu(\text{CC})$), but the only positive contribution in the reduced state at 1256 cm^{-1} in H_2O is very small. For the respective deprotonated species, further contributions (Tyr–O⁻; $\nu(\text{CC})$) are expected between 1602 cm^{-1} and 1599 cm^{-1} , but no contribution with negative sign is found in this range. The respective vibrational mode might

be obscured by other vibrations and thus not detectable in the spectrum. A rather strong absorbance of the deprotonated Tyr is expected between 1273 cm^{-1} and 1269 cm^{-1} . (Tyr-O⁻; $\nu(\text{C-O})$, $\nu(\text{CC})$). The difference signal in this region (in the oxidized state) is indeed negative, but the band is very broad and the intensity too low for the expected contribution. Again, the respective vibration might be hidden under overlapping difference signals of opposite sign and is thus undetectable in the experiment.

Numerous Tyr residues in *W. succinogenes* QFR are conceivable as possible candidates (38 Tyr per QFR monomer), which could be involved in the induced redox reaction, but a proper assignment would require further mutagenesis studies.

In the reduced state of QFR, further contributions are found at 1426 cm^{-1} and 1418 cm^{-1} , that can tentatively be assigned to Pro $\nu(\text{CN})$ vibrations, which are sensitive to the backbone conformation of the protein (Barth & Zscherp, 2002). Another possible origin for the peak at 1426 cm^{-1} is a Trp ($\delta(\text{NH})$, $\nu(\text{CC})$, $\delta(\text{CH})$) vibration (Barth & Zscherp, 2002). This assignment is also in line with the observed $^1\text{H}/^2\text{H}$ sensitivity of the particular vibration, since the signal is lost in D₂O (and is possibly shifted to 1409 cm^{-1}). The positive peak at 1410 cm^{-1} is tentatively assigned to a Gln $\nu(\text{CN})$ vibration (Barth & Zscherp, 2002). Alternatively, the three bands mentioned above might indicate $\nu_s(\text{COO}^-)$ modes of Asp or Glu side chains (Venyaminov & Kalnin, 1990), although it is less likely to observe those modes in the reduced state.

At 1348 cm^{-1} , 1340 cm^{-1} , and 1330 cm^{-1} , three vibrations are found in the reduced state, which can tentatively be assigned to further Trp vibrations (Barth & Zscherp, 2002).

3.2.1.11 Table with tentative FTIR band assignments of QFR enzyme

All performed tentative assignments of IR vibrations are summarized in Table 3.3.

Table 3.3: Summary of tentative IR-band assignments of *Wolinella succinogenes* QFR.

Multiple assignments are given for several vibrations, which represent possible alternatives or additional contributions at the same wavenumber. QFR WT band affiliations (in H₂O buffer at pH 7) are given for the corresponding redox state, and are indicated for the reduced (red) and oxidized (ox) state, respectively. The subscripts “as” and “s” indicate antisymmetric and symmetric vibrations, respectively. Porphyrin and propionate are abbreviated as “porph.” and “prop.”, respectively. See text for references and details of the assignments.

| Wavenumber [cm ⁻¹] | redox state | tentative assignments |
|--------------------------------|-------------|---|
| 1738 | red | Glu C180; $\nu(\text{C}=\text{O})$ |
| 1732 | ox | Glu C180; $\nu(\text{C}=\text{O})$ |
| 1718 | ox | FAD; $\nu(\text{C}_4=\text{O})$ Asp/Glu; $\nu(\text{C}=\text{O})$ |
| 1702 | ox | heme prop.; $\nu(\text{C}=\text{O})$ Asn; $\nu(\text{C}=\text{O})$ |
| 1692 | ox | Arg; $\nu_{\text{as}}(\text{CN}_3\text{H}_5^+)$ heme prop.; $\nu(\text{C}=\text{O})$ Asn/Gln; $\nu(\text{C}=\text{O})$ |
| 1678 | ox | amide I; turns and β -sheets |
| 1660 | red | Gln; $\nu(\text{C}=\text{O})$ |
| 1650 | red | Arg; $\nu_{\text{s}}(\text{CN}_3\text{H}_5^+)$ |
| 1632 | red | amide I; β -sheets |
| 1617 | red | heme vinyl; $\nu(\text{C}_\alpha=\text{C}_\beta)$ Tyr—OH; $\nu(\text{CC})$ $\delta(\text{CH})$ Asn/Gln; $\delta(\text{NH}_2)$ |
| 1601 | red | Gln; $\delta(\text{NH}_2)$ Tyr—OH; $\nu(\text{CC})$ |
| 1582 | ox | Asp/Glu; $\nu_{\text{as}}(\text{COO}^-)$ |
| 1576 | ox | Asp/Glu; $\nu_{\text{as}}(\text{COO}^-)$ |
| 1560 | ox | heme prop./Asp/Glu; $\nu_{\text{as}}(\text{COO}^-)$ |
| 1545 | red | heme porph.; $\nu(\text{C}_b\text{C}_b)$ and/or $\nu_{\text{as}}(\text{C}_a\text{C}_m)$ |
| 1516 | red | FAD; $\delta(\text{C}_6\text{-H})$ and $\delta(\text{C}_9\text{-H})$ Tyr—OH; $\nu(\text{CC})$, $\delta(\text{CH})$ |
| 1501 | ox | Tyr—O ⁻ ; $\nu(\text{CC})$, $\delta(\text{CH})$ |
| 1462 | ox | heme porph.; $\nu_{\text{s}}(\text{C}_a\text{C}_m)$ |
| 1438 | red | heme porph.; $\nu(\text{C}_a\text{C}_b)$ |
| 1426 | red | Pro; $\nu(\text{CN})$ Trp; $\delta(\text{NH})$, $\nu(\text{CC})$, $\delta(\text{CH})$ |
| 1418 | red | Pro; $\nu(\text{CN})$ |
| 1410 | red | Gln; $\nu(\text{CN})$ |
| 1370 | ox | heme prop./Asp/Glu; $\nu_{\text{s}}(\text{COO}^-)$ |
| 1348 | red | Trp |
| 1340 | red | Trp |
| 1330 | red | Trp |
| 1276 | ox | Tyr—O ⁻ ; $\nu(\text{C}-\text{O})$, $\nu(\text{CC})$ |
| 1267 | ox | Tyr—O ⁻ ; $\nu(\text{C}-\text{O})$, $\nu(\text{CC})$ |
| 1256 | red | Tyr—OH; $\nu(\text{C}-\text{O})$, $\nu(\text{CC})$ |
| 1162 | ox | buffer; P=O |
| 1088 | red | buffer; P=O |

3.2.1.12 Influence of amino acid exchanges on FTIR difference signals in the range of $\nu(\text{COOH})$ modes

In the scope of this study, the most interesting spectral region is that of protonated Glu and Asp side chains, which is depicted in Figure 3.10. All four discussed enzyme types (WT, E66Q, E270Q, and E180Q) show contributions in their FTIR difference spectra in the range between 1760 cm^{-1} and 1720 cm^{-1} (same data as in Figure 3.8). QFR WT exhibits a derivative-shaped pair of difference bands with similar width and amplitude at $1738\text{ cm}^{-1}/1732\text{ cm}^{-1}$ in H_2O (see inset of Figure 3.10). In D_2O , at pD 7.4, the positive contribution in the reduced state is lost, and the signal is broadened and shifted to lower wavenumbers (approximately to 1734 cm^{-1} , see inset of Figure 3.9). Compared to WT QFR, the difference spectrum of the enzyme variants E66Q and E270Q exhibit a similar signal pattern with minor differences, which may be attributed to imperfect scaling and baseline variations (see Figure 3.10). In contrast, the replacement of residue Glu C180 by a glutamine leads to a completely different signal pattern. The shape of the difference band is reversed compared to the spectra of WT, E66Q, and E270Q, with peaks now at $1743\text{ cm}^{-1}/1735\text{ cm}^{-1}$. Upon $^1\text{H}/^2\text{H}$ exchange, the band structure of E180Q is also slightly broadened and shifted to lower wavenumbers (to 1738 cm^{-1} , data shown in APPENDIX, Fig. 6.10). For all enzyme types, the peak around 1718 cm^{-1} in H_2O is shifted to lower wavenumbers by approximately 10 cm^{-1} upon $^1\text{H}/^2\text{H}$ exchange (see Figure 3.9 plus inset; data for enzyme variants shown in APPENDIX, Figure 6.10 and 6.11).

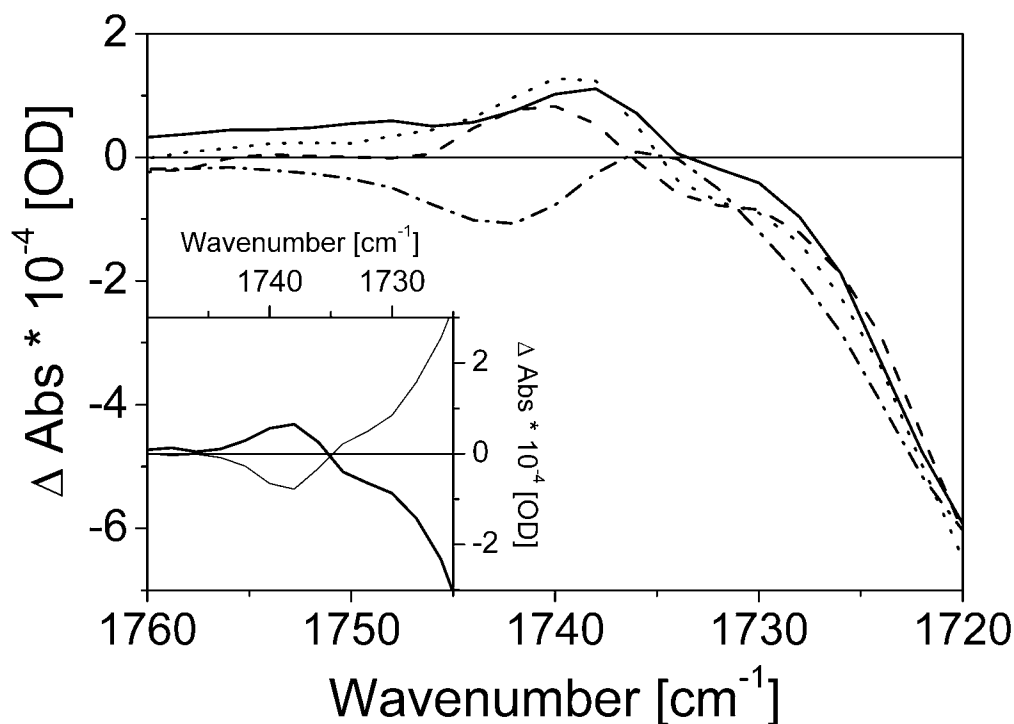


Figure 3.10: FTIR difference spectra of QFR WT and variants above 1720 cm^{-1} .

The figure presents a superposition of “reduced-minus-oxidized” FTIR difference spectra of QFR WT (*solid line*), E66Q (*dashed line*), E270Q (*dotted line*), and E180Q (*dashed-dotted line*) at pH 7. Reference electrode potentials for the shown FTIR difference spectra were +0.21 V (full oxidative potential) and -0.37 V (full reductive potential). The inset features the same data as in the big figure but with a slight baseline correction. In addition, the data is supplemented with the corresponding “oxidized-minus-reduced” FTIR difference spectrum (*thin line*).

In order to specify the spectral effects of the introduced mutations E66Q, E270Q, and E180Q, double-difference spectra of WT and the respective variant spectra were calculated. In theory, the bands that are visible in this type of double-difference spectra can solely be attributed to the spectral differences induced by the single mutation. But in practice, this would also imply perfect scaling of the corresponding difference spectra, which is not a straightforward task in some cases. In Figure 3.11, double-difference spectra for “WT-minus-E66Q, E270Q, and E180Q”, respectively, are shown, which correspond to the back and forward direction of the redox reaction. The double-difference spectrum of “WT-minus-E66Q” emphasizes the similarities of E66Q and WT spectra in the region above 1730 cm^{-1} . It is difficult to decide whether the deviation, which appears below 1730 cm^{-1} , is potentially significant, and is thus an effect of the mutated residue or simply an artifact due to imperfect scaling of the two sets of spectra. In principle, the characteristics of the double-difference spectra of “WT-minus-E66Q” and “WT-minus-E270Q” are very similar with respect to the frequency position of positive and negative residual difference signals. The small difference

signals that can be seen around 1740 cm^{-1} in Figure 3.11 a and b are due to slightly different positions of the peaks around 1740 cm^{-1} as can already be seen in Figure 3.10. Various reasons are conceivable for the slightly different peak positions: First of all, the limited spectral resolution of the FTIR spectrometer, which was 4 cm^{-1} (i.e., a data point separation of 2 cm^{-1}), has to be considered. Secondly, the signals of protonated carboxyl groups are pH sensitive (see also Figure 3.12). The QFR protein complex has many buffering groups itself, and different protein concentrations in the individual experiment might thus lead to small variations of the sample pH. This effect would be more pronounced in the vicinity of the isoelectric point of the QFR protein complex, which is pH 6.0 (Lancaster, 2003d). Furthermore, signals of COOH groups with lower frequencies are less isolated and instead more hydrogen-bonded, which also indicates higher solvent accessibility and thus a higher sensitivity for pH changes.

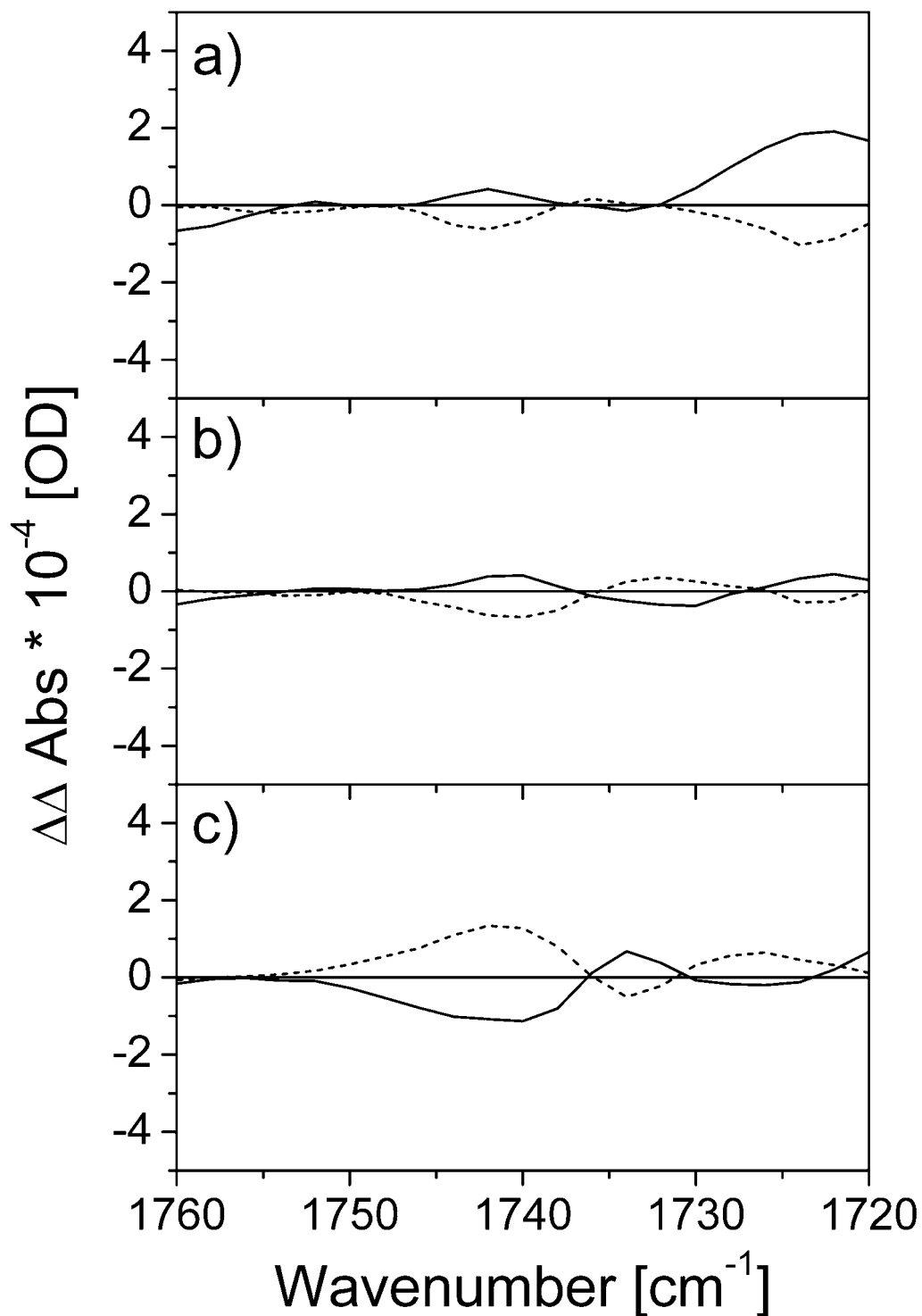


Figure 3.11: FTIR double-difference spectra of QFR WT and enzyme variants.

The “oxidized-minus-reduced” (*solid line*) and “reduced-minus-oxidized” (*dashed line*) FTIR double-difference spectra of a) “WT-minus-E66Q”, b) “WT-minus-E270Q”, and c) “WT-minus-E180Q” at pH 7. Reference electrode potentials for the shown FTIR double-difference spectra were +0.21 V (full oxidative potential) and -0.37 V (full reductive potential). The data shown here are based on the data presented in Figure 3.8, but with corrected baselines (i.e., where necessary, a constant of the order of the noise level was subtracted to guarantee zero-crossings of the pairs of double-difference spectra at the same wavenumber. This procedure is identical with setting the spectra to zero at wavenumbers around 1760 cm^{-1} and above where no further signals were observed.).

Inspection of the double-difference spectrum of “WT-minus-E270Q” (see Fig. 3.11 b) underlines the result that WT and variant spectrum are indeed very similar, making it unlikely that Glu A270 undergoes any environmental or protonation changes in the course of the induced reaction.

A double-difference spectrum of WT and E180Q (see Figure 3.11 c) unequivocally indicates the dramatic effect that the mutation E180Q has on the signal pattern of the electrochemically induced FTIR difference spectra of QFR in the spectral range of protonated carboxylic acid groups. Compared to the other two variants, the amplitude of the double-difference signal of “WT-minus-E180Q” above 1730 cm^{-1} is sufficiently above the noise level to be considered significant and the observed difference signal cannot be explained by the scaling difficulties mentioned above, baseline effects or pH variations.

3.2.1.13 The pH dependency of $\nu(\text{COOH})$ modes

Figure 3.12 shows the pH dependency of the QFR WT enzyme in the frequency range of protonated carboxyl groups between pH 5.5 and pH 8.8. With increasing pH, the positive peak around 1740 cm^{-1} diminishes and a broader negative band develops. At pH 6, the observed signals are minimal, and the biggest changes occur between pH 7.5 and pH 8.5. This pH-dependent behavior yields further support for the assignment of the respective difference bands found above 1725 cm^{-1} to protonated carboxylic acid groups of Glu and Asp side chains. It is also likely that multiple acidic residues are involved in the observed signal pattern, since different groups could contribute at different pH values. Also the spectral feature, which is centred around 1718 cm^{-1} at neutral pH, is affected by pH variation with respect to its position and intensity, and becomes smaller with increasing pH. This could be due to underlying signals (of Asp or Glu side chains) or could reflect a pH-dependence of the tentatively assigned FAD signal.

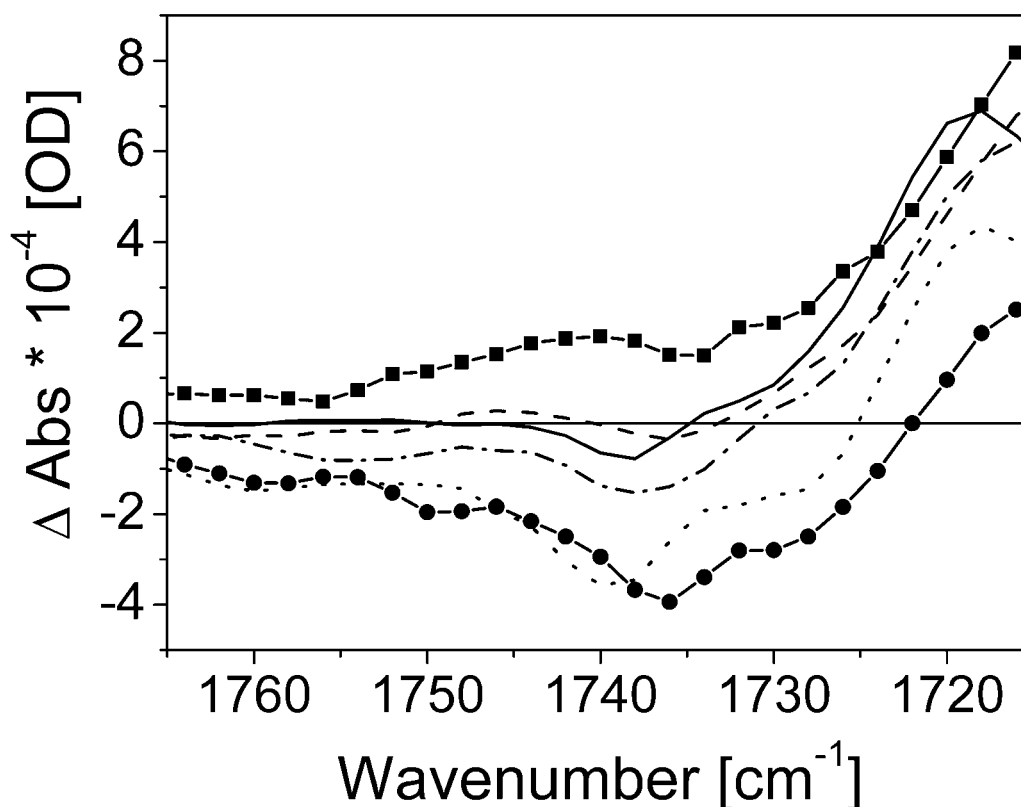


Figure 3.12: The pH-dependence of the FTIR difference spectra above 1715 cm^{-1} .

Superposition of “oxidized-minus-reduced” FTIR difference spectra of QFR WT at pH 5.5 (*squares*), pH 6 (*dashed line*), pH 7 (*solid line*), pH 7.5 (*dashed-dotted line*), pH 8.5 (*dotted line*), and pH 8.8 (*circles*). Reference electrode potentials for the shown FTIR difference spectra were $+0.21\text{ V}$ (full oxidative potential) and -0.37 V (full reductive potential).

3.2.2 FTIR difference spectroscopy on QFR with ^{13}C -labeled heme propionates

3.2.2.1 Midpoint potentials of labeled hemes at pH 7

As a first control and characterization of the ^{13}C -labeled QFR, the midpoint potentials of the heme *b* groups were determined at pH 7. The observed midpoint potentials for the high- and low-potential hemes were $+4\text{ mV}$ and -137 mV , respectively (the corresponding titration curves are shown in APPENDIX, Fig. 6.14). Thus, the values are approximately 10 to 15 mV higher than the average midpoints measured in the unlabeled WT. For the latter, the statistical basis was broader since more independent data were collected, and an experimental error of $\pm 10\text{ mV}$ was estimated from the data scattering at pH 7. For the ^{13}C -labeled enzyme, the value obtained for the high-potential proximal heme b_p lies within the error, and the value for the

low-potential distal heme b_D exceeds it by +5 mV. Thus, the influence of the ^{13}C -label on the heme midpoint potentials, if any, is minor.

3.2.2.2 Reversible FTIR difference spectra of the “full potential” step

Figure 3.13 shows the reversible electrochemically induced FTIR difference spectra of the unlabeled and labeled QFR WT enzyme, respectively, at pH 7 for the full potential step.

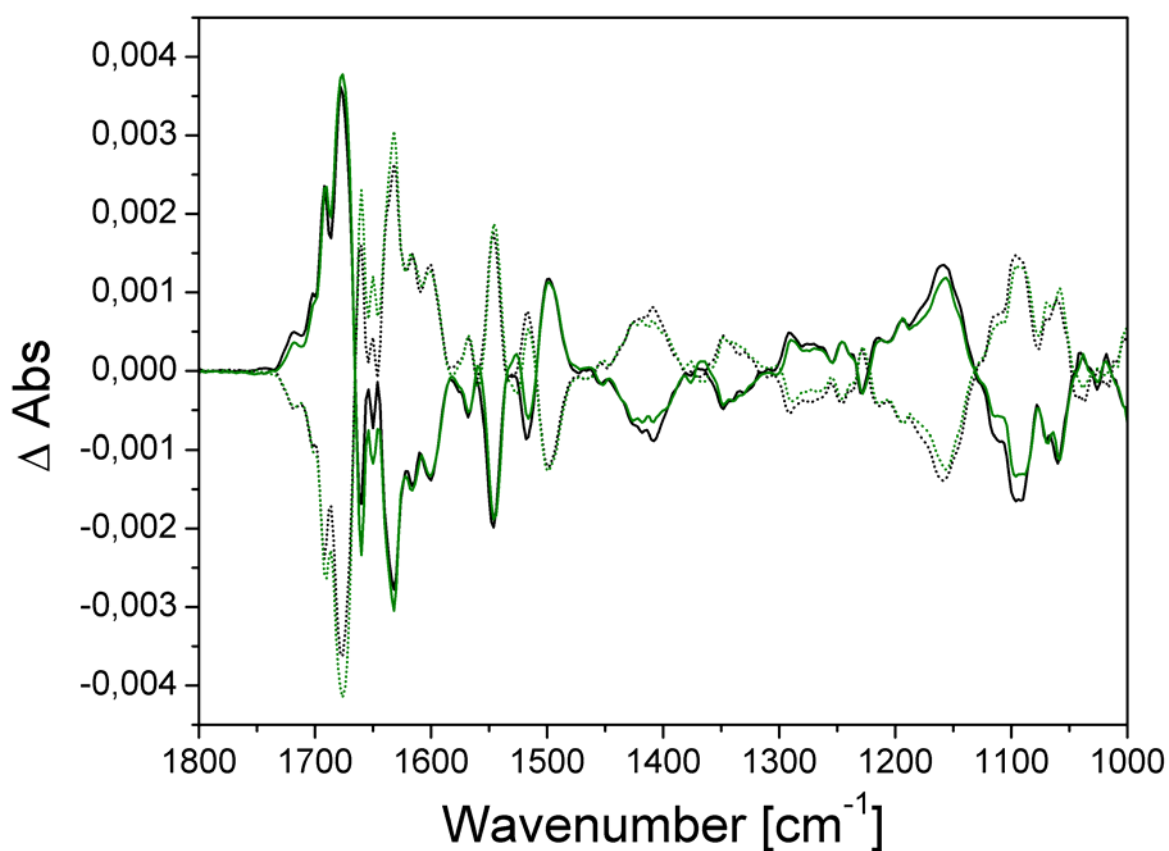


Figure 3.13: Electrochemically induced FTIR difference spectra of unlabeled and ^{13}C -labeled QFR.

Reversible full potential steps “oxidized-minus-reduced” (*solid line*) and “reduced-minus-oxidized” (*dotted line*) FTIR difference spectra of the unlabeled QFR WT (in *black*), and ^{13}C -labeled enzyme (in *olive*) at pH 7. The reference electrode potentials (vs. SHE’) for the shown FTIR difference spectra were +0.21 V (full oxidative potential) and -0.37 V (full reductive potential).

The FTIR difference spectra obtained for the QFR containing the ^{13}C -labeled heme propionates are very similar to those for the unlabeled WT (see Figure 3.13), which indicates that the possible heme propionate contributions in the full potential step are of small amplitude. Thus, it is advisable to compute double-difference spectra in order to better resolve any smaller signals (see below).

3.2.2.3 Separation of redox-induced IR signals from hemes b_D and b_P

Since the midpoint potentials of the two heme groups of QFR differ by almost 150 mV, it is feasible to separate the heme corresponding signals and address the low- and high-potential hemes individually by setting the appropriate reference potentials in the experiment. The best separation is achieved at an “intermediate” potential, which corresponds to the average of the two midpoints. At this intermediate electrode potential of -81 mV, about 95 % of the high-potential hemes are reduced, and 95 % of the low-potential hemes are oxidized. Thus, the separation of the two heme midpoint potentials is wide enough to guarantee negligible contributions (≤ 5 %) of the respective other heme in the two partial potential steps “reduced-minus-intermediate” and “intermediate-minus-oxidized” (and vice versa). The corresponding spectra are shown in Figure 3.14 and Figure 3.15 ¹.

¹ Because of the small signals that are investigated and the occurrence of noticeable baseline instabilities in the respective experiments, the spectra corresponding to the partial potential steps had to be baseline-corrected (the respective pairs of difference spectra, e.g., “reduced-minus-intermediate” and “intermediate-minus-reduced”, were summed to determine the baseline drift). This did not seem to have a disturbing impact on the quality of the data, since independently baseline-corrected spectra are practically identical. As a consequence of the correction, the opposite directions, e.g., “reduced-minus-intermediate” and “intermediate-minus-reduced”, are symmetrical and contain the same information.)

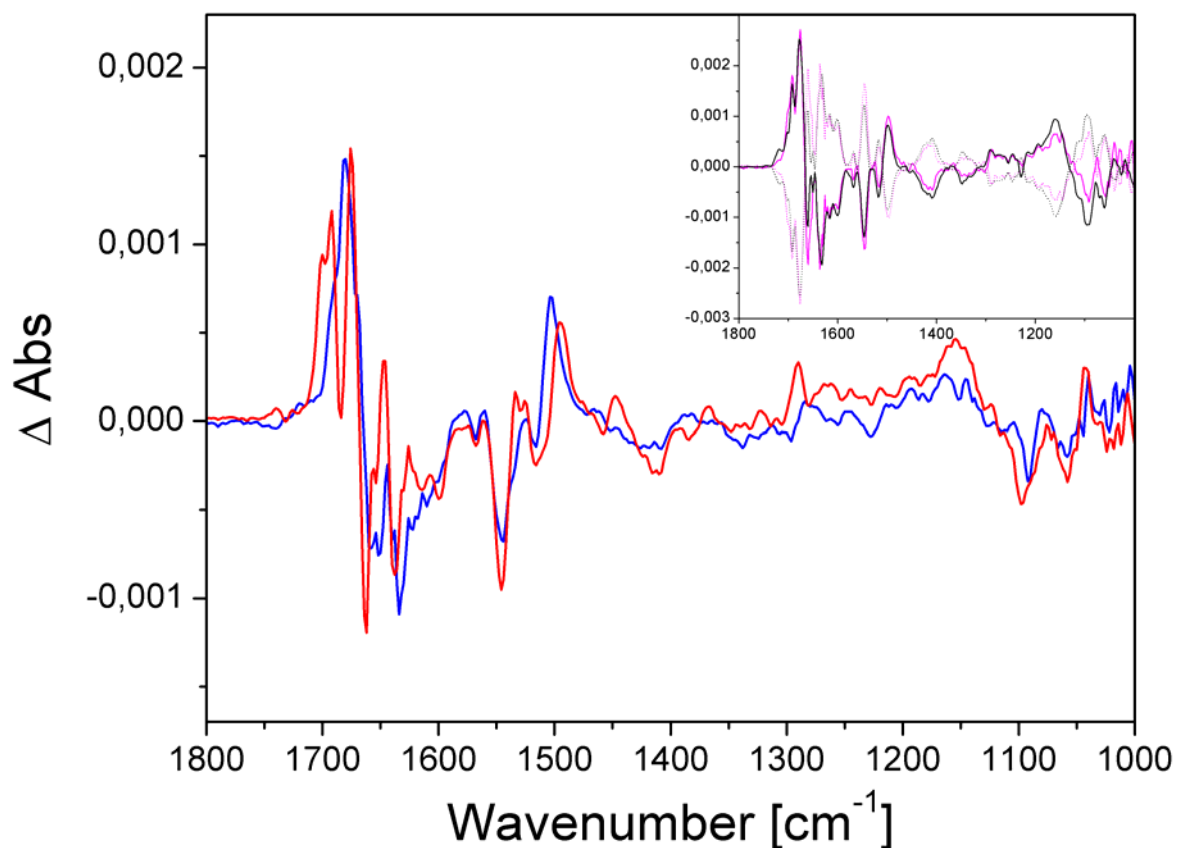


Figure 3.14: Electrochemically induced FTIR difference spectra of unlabeled QFR at pH 7 with intermediate step.

Reversible “oxidized-minus-intermediate” (*solid blue line*), and reversible “intermediate-minus-reduced” (*solid red line*) FTIR difference spectra. The reference electrode potentials for the shown FTIR difference spectra were +0.21 V (full oxidative potential), −0.08 V (intermediate potential), and −0.37 V (full reductive potential). The inset shows a comparison of the difference spectra of the measured full potential step (in *black*, same data as in Fig. 3.13) with computed “full potential step” difference spectra (in *magenta*), which are based on the sum of the respective pairs of spectra including the intermediate step (e.g., “reduced-minus-oxidized” is compared with the sum: “intermediate-minus-oxidized” plus “reduced-minus-intermediate”).

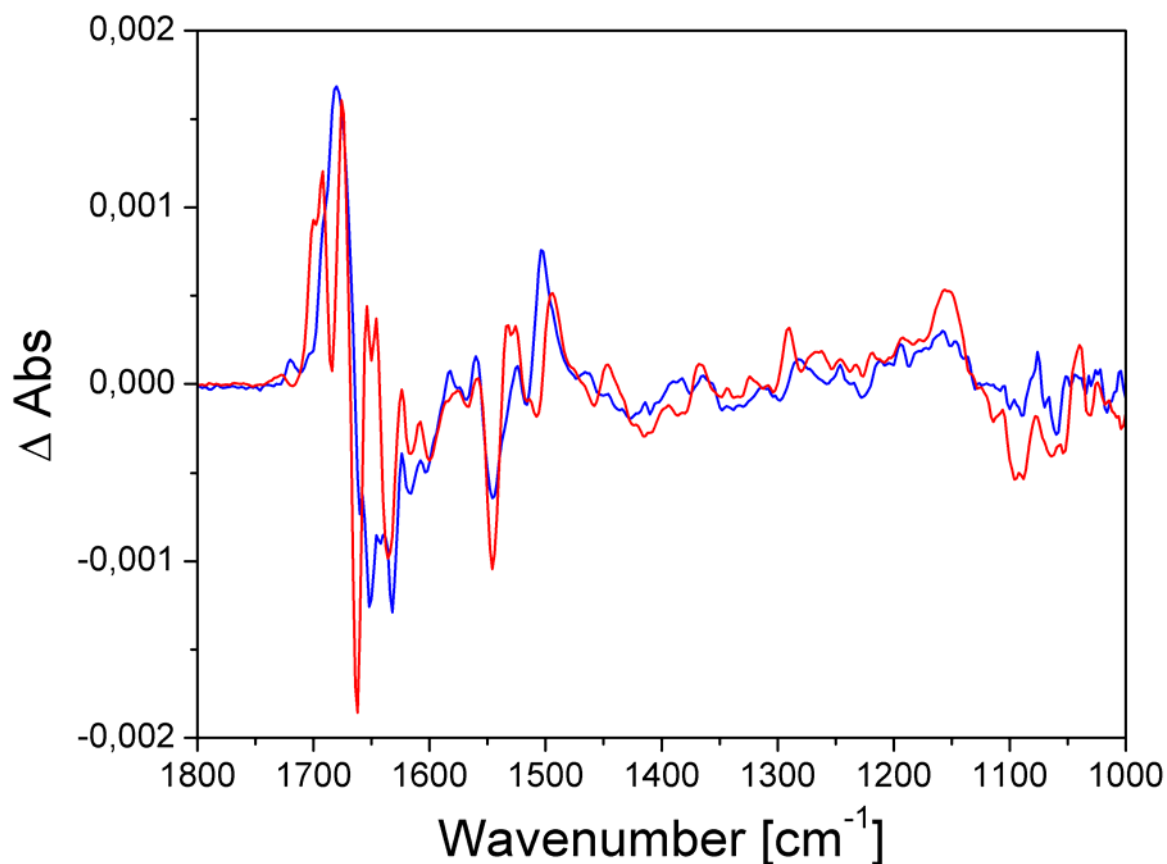


Figure 3.15: Electrochemically induced FTIR difference spectra of ^{13}C -labeled QFR at pH 7 with intermediate step.

Reversible “oxidized-minus-intermediate” (*solid blue line*), and reversible “intermediate-minus-reduced” (*solid red line*) FTIR difference spectra. The reference electrode potentials for the shown FTIR difference spectra were +0.21 V (full oxidative potential), -0.07 V (intermediate potential), and -0.37 V (full reductive potential).

Again, the spectra of labeled and unlabeled QFR are very similar, as can be seen by comparing Figure 3.14 and Figure 3.15; and thus, it is necessary to look at double-difference spectra (see below). In addition, the inset of Figure 3.14 shows how well the full potential step, i.e., the electrochemically induced redox reaction, can be subdivided in two halves (see explanation in the figure legend). This addition of difference spectra can equally be performed for the labeled enzyme (data not shown).

The FTIR difference spectra of the two potential steps, which include the intermediate potential, reflect the redox transitions of the two heme groups b_D and b_P (contributions from or due to the other cofactors and prosthetic groups in the spectra are inevitable). Although the difference spectra reveal clear deviations, the positions and proportions of the main spectral features are similar for both partial potential steps, and also comparable for the unlabeled and labeled QFR enzyme (see Figure 3.14 and Figure 3.15). The differences between the two steps in the amide I range of the spectra could arise from distinct sets of amino acid residues,

which are only addressed in the course of the individual potential step, and/or they could indicate redox-induced structural changes of the polypeptide backbone of QFR, which are either related to the redox transition of the high- or the low-potential heme. The sharp peak at 1545 cm^{-1} , which is observed in the full potential step, has tentatively been assigned to heme porphyrin $\nu(\text{C}_b\text{C}_b)$ and/or $\nu_{\text{as}}(\text{C}_a\text{C}_m)$ vibrations (cf. Table 3.3 for the tentative IR band assignments). An analogous signal is present in both partial potential steps (with lower intensity than in the full potential step), which is in line with the performed assignment. The tentative Tyr modes, observed at 1516 cm^{-1} and 1501 cm^{-1} in the full potential step, are also visible in the high-potential partial step at 1516 cm^{-1} and 1503 cm^{-1} , and at 1516 cm^{-1} and 1496 cm^{-1} in the low-potential step. If the performed assignment (cf. Table 3.3) is correct, this observation would indicate the (de)protonation reaction of two different Tyr residues or that a single Tyr is engaged in a very broad transition with respect to the applied redox potential. Alternatively, as mentioned earlier, the pair of bands might however have to be assigned to heme vibrations. Further mutagenesis work is required to clarify the precise origin of this distinct spectral feature.

The sharp peak, which can be observed for both enzyme types in the low-potential partial step at 1292 cm^{-1} (see Figure 3.14 and Figure 3.15), could be identified as a spectral artifact from the mediators (probably from the various quinones in the mixture) that were too highly concentrated in this particular experiment. Importantly, the position of this band does not interfere with the intended assignments of heme propionate signals (this was checked by measuring the mediator-buffer mixture alone, data shown in APPENDIX, Fig. 6.7).

The PO modes from the potassium phosphate buffer below 1200 cm^{-1} reflect proton exchange between the protein (and the mediators) and the buffer (Hellwig *et al.*, 1996 and 1999c; and Baymann *et al.*, 1999). The spectra for the two partial potential steps show that this effect is more pronounced in the low-potential partial step (see Figure 3.14 and Figure 3.15) since the amplitude of the respective bands is stronger in this step.

3.2.2.4 Tentative signals of protonated heme propionate(s) of heme b_D

The range of Asp or Glu $\nu(\text{COOH})$ modes above approximately 1710 cm^{-1} (Venjaminov & Kalnin, 1990) is of particular interest with respect to a possible coupling of proton transfer via acidic groups to the redox transition of the high- and low-potential heme, respectively. At 1718 cm^{-1} , a signal in the full potential step of the unlabeled QFR WT enzyme has tentatively been assigned to a FAD $\nu(\text{C}_4=\text{O})$ vibration in the oxidized state. This

signal can also be identified in the oxidized state of the high-potential partial step, and it is more pronounced in the ^{13}C -labeled enzyme (see Figure 3.14 and Figure 3.15). The affiliation of this signal to the high potential is in line with the midpoint potential of the covalently bound FAD in QFR (-20 mV, as reviewed in ref. Lancaster, 2004). The difference spectra of the ^{13}C -labeled and unlabeled QFR associated with the low-potential step - and thus with heme b_D - differ considerably above 1710 cm^{-1} . In the unlabeled WT, two separated positive contributions associated with the intermediate state are centered at 1740 cm^{-1} and 1726 cm^{-1} . The peak at 1740 cm^{-1} looks similar to the “reduced-minus-oxidized” difference spectrum of the enzyme variant E180Q (see Fig. 3.10). In the ^{13}C -labeled enzyme, the low-potential step reveals one broad contribution in the intermediate state around 1728 cm^{-1} . Hence, it has to be concluded that at least one propionate of b_D contributes in this high frequency range, and that the vibration is downshifted by 15 to 20 wavenumbers upon ^{13}C -labeling (see Fig. 3.16).

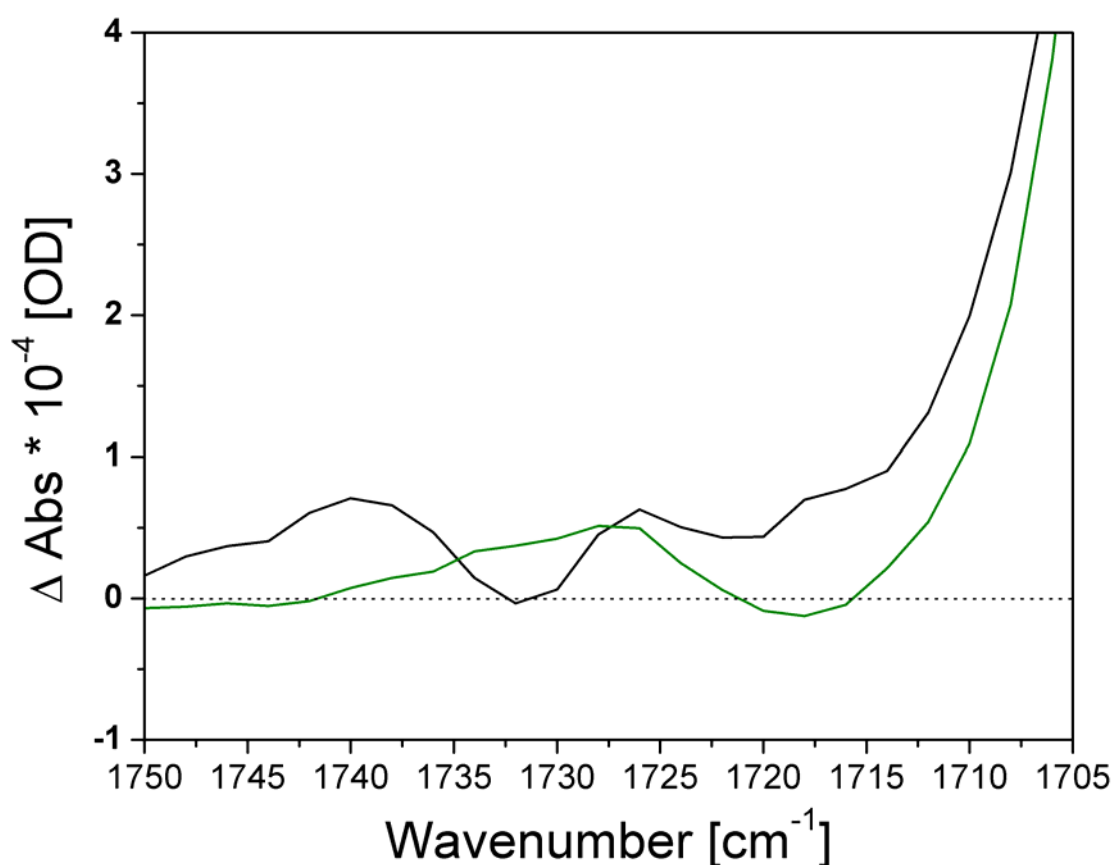


Figure 3.16: Detail of FTIR difference spectra of unlabeled and ^{13}C -labeled QFR at pH 7.

FTIR difference spectra of the partial potential step “intermediate-minus-reduced” (*solid black line*), for the unlabeled WT; and “intermediate-minus-reduced” (*solid olive line*) for the ^{13}C -labeled WT. The reference electrode potentials are the same as indicated above.

3.2.2.5 “Unlabeled-minus- ^{13}C -labeled” QFR FTIR double-difference spectra

The results presented above are summarized by their corresponding double-difference spectra, which are shown in Figure 3.17.

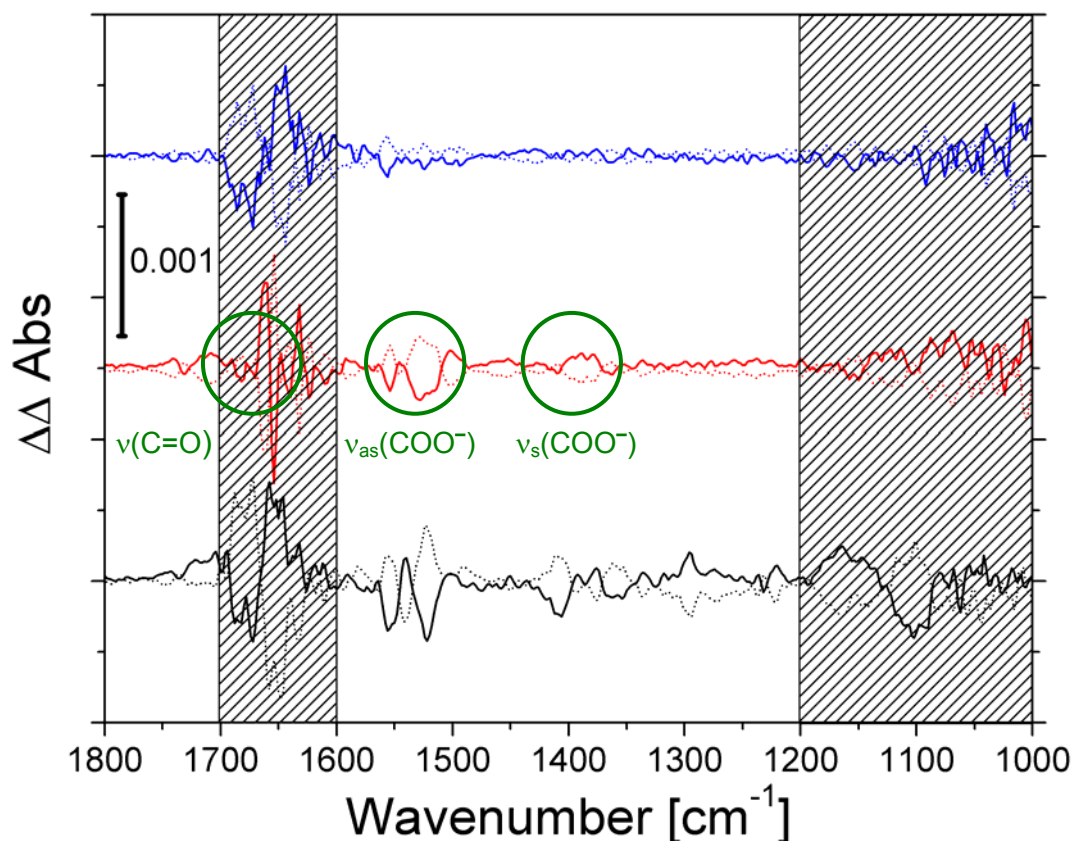


Figure 3.17: FTIR double-difference spectra of “unlabeled-minus- ^{13}C -labeled” QFR at pH 7.

The upper traces show the data for the potential step “oxidized-minus-intermediate” (*solid blue line*), and vice versa (*dotted blue line*); in the middle for “intermediate-minus-reduced” (*solid red line*), and vice versa (*dotted red line*). The full potential step “oxidized-minus-reduced” (*solid black line*), and vice versa (*dotted black line*), is shown in the lower pair of traces (reference potentials as indicated above). The dark green circles point out the frequency ranges in which the contributions of the heme propionates are expected. The *hatched areas* correspond to regions of elevated noise level (in the amide I region, 1700 cm^{-1} to 1600 cm^{-1} , due to the strong H_2O absorbance, and below 1200 cm^{-1} due to the absorbance of KP_1 -buffer modes), which are difficult to handle in double-difference spectra and should thus be excluded from the analysis.

The computed double-difference spectra are rather noisy, which is almost inevitable since independent experiments always differ slightly from each other and have to be scaled for comparison. Furthermore, the signals, which are of interest here, are comparatively small. Despite the noise, the double-difference spectra allow to assign the observed contributions in the respective spectra of the full potential step to the redox transition of the low-potential distal heme b_D . As can be seen in Figure 3.17 for the low-potential step, the positions of the

obtained FTIR double-difference bands of “unlabeled-minus- ^{13}C -labeled” QFR in the IR-spectrum coincide very well with the expected ranges (Behr *et al.*, 1998). The spectral features observed in the full and in the “reduced-minus-intermediate” potential step are very similar with respect to size and wavenumber of their occurrence. The series of difference-signals at 1553, 1528, and 1501 cm^{-1} can be attributed to antisymmetric vibrations of at least one deprotonated heme propionate of b_D , and the signal around 1388 cm^{-1} to the corresponding symmetric modes, respectively. Only residual contributions of very small amplitude (as mentioned above, an overlap of 5 % at the intermediate potential was estimated for the contributions of the two hemes) plus noise are seen at the corresponding wavenumbers in the “oxidized-minus-intermediate” potential step. Additional discrepancies between the double-difference spectra of the full and the “reduced-minus-intermediate” potential step might arise due to conformational changes or environmental differences, which could affect the heme propionate vibrations, and which are specifically related to the *intermediate* potential, as this state is does not contribute in the *full* potential step.

3.2.3 The pH-dependence of QFR WT and E180Q heme *b* midpoint potentials: The redox Bohr effect

The midpoint potentials of the two *b*-type hemes of *Wolinella succinogenes* WT QFR enzyme and variant E180Q, respectively, were determined with the help of VIS redox titrations as a function of the ambient pH (see Table 3.4).

| pH | WT | | | E180Q | | |
|-----|------------|-------------|--------|------------|-------------|--------|
| | $E_{m,H}$ | $E_{m,L}$ | # data | $E_{m,H}$ | $E_{m,L}$ | # data |
| 4.9 | 58 | -76 | 10 | | | |
| 5.5 | 35 | -98 | 4 | 48 | -115 | 20 |
| 6.0 | 29 | -128 | 12 | | | |
| 6.1 | | | | 51 | -123 | 15 |
| 6.5 | 6 | -146 | 18 | 37 | -140 | 12 |
| 7.0 | -4 | -152 | 24 | 35 | -148 | 16 |
| 7.5 | -31 | -167 | 24 | 38 | -143 | 12 |
| 8.0 | -56 | -171 | 26 | 35 | -157 | 12 |
| 8.5 | -77 | -188 | 11 | -2 | -164 | 14 |
| 8.8 | -80 | -189 | 16 | | | |
| 9.0 | | | | -34 | -172 | 12 |

Table 3.4: QFR WT and E180Q heme *b* midpoint potentials at various pH values.

The midpoints $E_{m,H}$ and $E_{m,L}$ are given in [mV]. The columns labeled “# data” indicate the number of averaged individual data points (which were obtained from the Soret- and the α -band in multiple oxidative and reductive titrations, i.e., 4 values per heme for a typical single experiment).

For both QFR enzyme types, WT and E180Q, a pronounced pH-dependence was observed for the midpoint potentials of the high- and low-potential hemes. Although a broad pH range was covered in the experiments, it was not possible to extend it to pH values high and/or low enough to clearly observe the disappearance of the pH-dependence above and below the respective pK values (see Figure 3.18). Figure 3.18 shows the fitting-curves of the obtained data according to equation (12) in chapter 1.2.1.

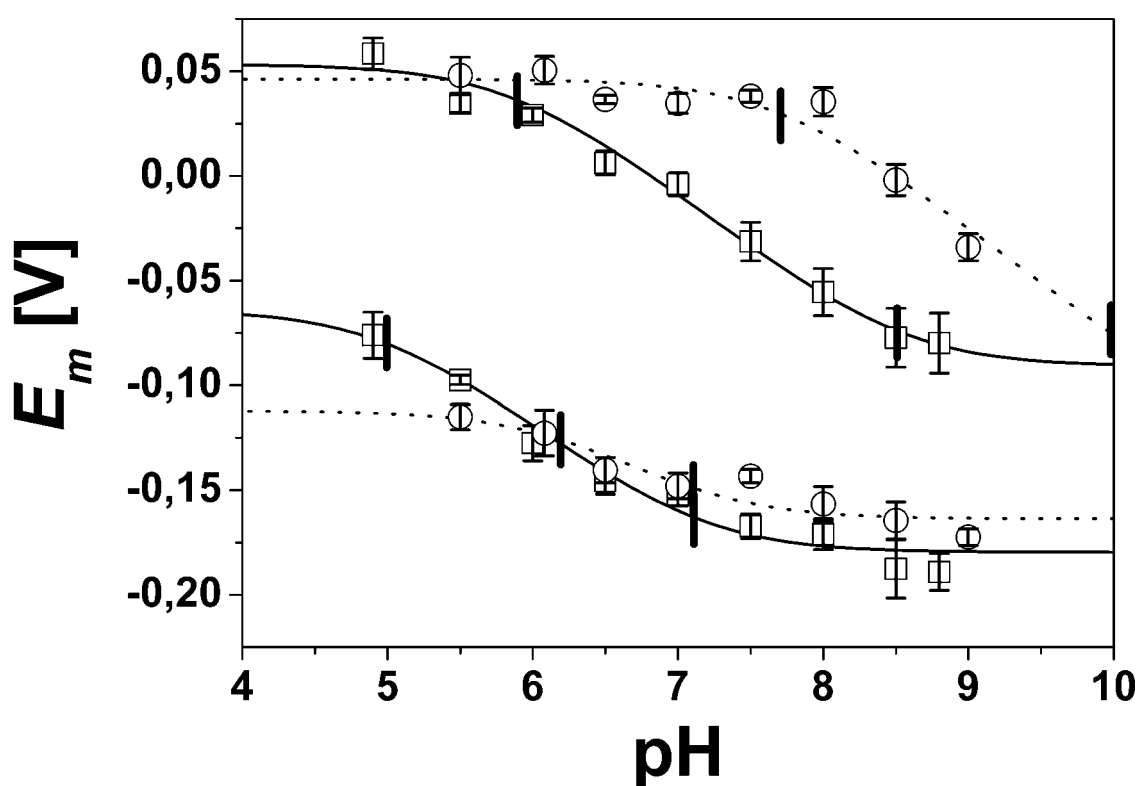


Figure 3.18: The pH-dependence of the heme b midpoint potentials of *W. succinogenes* QFR WT and E180Q.

Data for QFR WT are shown as *open squares* and the corresponding fitting-curve as *solid line*, *open circles* and *dotted line* for E180Q, respectively. Upper and lower data correspond to high- and low-potential heme, respectively. The error bars indicate the standard deviation of the data points measured at a specific pH and do not unequivocally reflect the real error of the midpoint potential. The *vertical bars* indicate the positions of the values for pK_{ox} and pK_{red} (see text for the numbers).

The differences between the two enzyme types are more distinct for the high-potential heme. Unfortunately, it was not possible to obtain useful data for E180Q below pH 5.5. Thus, it is unclear whether the value for E_{m0} in the case of the low-potential heme is really lower for the variant as indicated by the obtained fitting-curve or whether the missing data leads to a

incorrect value for E_{m0} . The respective values for the high-potential hemes are very comparable, although the corresponding values for pK_{ox} and pK_{red} are very different. The experimental errors at higher and lower pH values might be bigger compared to neutral pH since the enzyme is exposed to conditions far from its native environment and might thus be less stable and the structure less well defined.

The parameters obtained by fitting the data with eq. (12) are summarized in Table 3.5.

| | WT | | E180Q | |
|-----------------------|------------------|------------------|------------------|------------------|
| | b_H | b_L | b_H | b_L |
| E_{m0} | 53 ± 3 | -64 ± 6 | 46 ± 3 | -112 ± 3 |
| $E_{m(\text{Bases})}$ | -90 | -180 | — | -164 |
| pK_{ox} | 5.9 ± 0.1 | 5.0 ± 0.2 | 7.7 ± 0.1 | 6.2 ± 0.1 |
| pK_{red} | 8.5 ± 0.1 | 7.1 ± 0.1 | < 10 | 7.1 ± 0.1 |
| R^2 | 0.94 | 0.89 | 0.88 | 0.80 |

Table 3.5: Summary of the redox Bohr-parameters, E_{m0} and $E_{m(\text{bases})}$, and pK_{red} and pK_{ox} .

Values for $E_{m(\text{bases})}$ were read directly from the fitting-curves. For E180Q, the value for pK_{red} is a lower limit (this number was set fixed as a lower limit during the fitting-procedure; values below $K_{red} = 1 \times 10^{-10}$ did not change the other results in the respective column). The respective value for $E_{m(\text{bases})}$ could not be determined. R^2 is the coefficient of determination of the fit.

The value of pK_{red} for enzyme variant E180Q is a lower limit since the real value cannot be determined on the basis of the obtained results. Fitting of the data with eq. (12) does not give a stable and sensible number with respect to the fitting parameter pK_{red} . The number obtained for pK_{ox} , though, is reliable. The respective curve in Figure 3.18 is a simulation with the obtained result for pK_{ox} , and $pK_{red} = 10$ as an approximate lower limit. Unfortunately, it was not possible to measure above pH 9 since QFR is not stable, and the experiment would not yield reasonable data (the same applies for very low pH).

4 DISCUSSION

The results from the electrostatic calculations shall be discussed before the experimental spectroscopic results. If necessary, a reference to related results obtained with the respective other technique is given in the discussion. Finally, the results from both approaches are summarized in the conclusions.

4.1 Electrostatics

The focus of the MCCE calculations lay on the simulation of the heme *b* redox-titration behavior, and the response of the QFR model with respect to the modeled intermediate states of electron transfer. Both aspects reflect equilibrium states of the protein. Thus, the results from MCCE calculations can also be related to the static spectroscopic experiments, which deal with equilibrium states in a first approximation as well.

4.1.1 Simulated heme E_h titrations

The results of the simulated E_h titrations of QFR presented in Figure 3.1 clearly reproduce the redox behavior of the heme groups of the detergent-solubilized enzyme as determined experimentally (Lancaster *et al.*, 2000). The values calculated for the midpoints of the high- and low-potential hemes agree very well with available experimental data, and the obtained agreement of midpoint potentials between simulation and experiment is in line with results from other studies using comparable (Gunner & Honig, 1991) or identical approaches (Mao *et al.*, 2003). The agreement for the high-potential heme based on model W is excellent. The agreement for the low-potential heme is better in the case of model X. However, the proximal heme site in the crystal structure is better defined than the distal site, as is reflected in higher temperature factors in the environment of the distal heme site (Lancaster *et al.*, 1999). Thus, the slight discrepancy of the simulation, based on the favored model W and the experiment, could be due to the higher temperature factors of the crystal structure around the distal heme. Also the inevitable backbone rigidity in the MCCE simulations might be inappropriate with respect to the different redox states of the hemes. It has been shown (e.g., in ref. Mao *et al.*, 2003) that the calculated E_m 's can largely depend on the starting structure of

the investigated cytochrome. For instance, MCCE calculations with oxidized and reduced structures of the same cytochrome might yield very different midpoint potentials. The most dominating origin for this discrepancy is that the heme-containing protein might undergo a conformational change upon reduction, which involves the backbone. Thus, the structure of the reduced cytochrome is not optimized to stabilize the oxidized heme. Such a backbone conformational change cannot be accounted for by the MCCE method since the conformational flexibility within the scope of MCCE is restricted to different side-chain orientations of polar and ionizable residues and polar hydrogen positions. In this respect, it should be kept in mind that the employed QFR model was based on a crystal structure of the oxidized enzyme, and it is presently not clear which structural changes QFR enzyme might undergo upon reduction. Yet the comparison of the obtained results with available experimental data shows that many effects, which are observed in the simulations, are directly reflected in the experiment. This finding enhances the level of confidence in the employed MCCE method, which is necessary for the evaluation of the generated results.

The obtained midpoint potentials of the high- and low-potential hemes are slightly decreased (by -24 mV for the low-, and by -36 mV for the high-potential heme) in the case of model X. In principle, the oxidized, charged heme species is always destabilized due to the loss of reaction field energy if it is removed from aqueous solution and is instead introduced into the protein (Kassner, 1972 and 1973). This destabilization of the oxidized state is then reflected in an elevated midpoint potential. Thus, the observed effect with waters is somewhat contradictory. But comparison of the electrostatic interaction energies in both cases (with and without water) shows that the positive Arg and Lys bases, which are highlighted in Figure 3.2, have slightly higher positive interaction energies with the oxidized heme groups in the case with the waters. This indicates a stronger destabilization of the oxidized heme species in the presence of the water molecules, which are included in model W.

The obtained relative difference between high- and low-potential midpoint potentials of the two hemes in the QFR model agrees very well with the previously measured experimental data (Lancaster *et al.*, 2000). This relative difference is of greater relevance than the consistence of the absolute midpoint potential values as this absolute value depends on the initial reference potentials that have been chosen for the bis-histidine-ligated heme *b* groups (Gunner & Honig, 1991). The presented results of simulated redox titrations show how well the employed method is able to reproduce the influence of the protein environment on the reference (midpoint) potentials of the heme groups and how the presented interactions of

individual groups with the hemes modify the absolute value of the oxidation-reduction potentials, which were obtained as a result of the simulations.

All effects related to the hemes (and also individual amino acid residues like Glu C180) in the QFR model, which were observed and discussed in this study, are related to the various mutual electrostatic interaction energies, as they are shown in Table 3.1. The 37 entries are only a small excerpt of the $n \times n$ interaction matrix, and in principle every conformer in the model interacts with all others. But as shown in the results section for the different heme midpoint potentials (and the redox-dependent pK_a values of Glu C180), it is feasible in most cases to restrict the analysis to the direct strong electrostatic interactions around the residue or group of interest. Only taking into account the strong electrostatic interactions listed in Table 1 was sufficient to explain the result that the protein environment destabilizes the oxidized heme species for the proximal site more strongly than for the distal site. Yet for a more exact reproduction of the difference in the two midpoint potentials, as it was found in the simulated titration at pH 7 (see Figure 3.1), it was necessary to sum over all occupancy-weighted interactions of the individual heme groups.

4.1.2 Assignment of the low- and high-potential heme to b_D and b_P

As a second main aspect of the simulated heme redox titrations, it was possible to assign the low-potential heme to the distal position and the high-potential heme to the proximal position in the QFR structure. For the two heme groups of the cytochrome *b* of QFR, this assignment was still a matter of debate. With the help of spectroscopically monitored heme redox titrations of a cytochrome, it is feasible to determine the presence of multiple heme groups and their respective midpoint potentials. Yet an unequivocal assignment of an individual heme to its position in a known structure is not a straightforward task. A tentative assignment, based on mutagenesis experiments, has been made for a close relative of *W. succinogenes* QFR, the SQR from *Bacillus subtilis* (Hägerhäll *et al.*, 1995). But in this study, the authors explicitly state with respect to their assignment: “However, the properties of the mutant cytochromes could be misleading since the loss of one heme may change the properties of the remaining heme.” For the performed electrostatic calculations the situation is different, as the results can directly be correlated with the individual coordinates on which the simulation is based. Thus, it becomes immediately apparent which site accommodates the low- and which the high-potential heme in the structure. The reliability of this assignment is increased by the fact that the employed approach has been well established

for many years, and also by how well the simulated and experimental data match. Figure 4.1 shows the experimentally deduced midpoint potentials of the substrates, prosthetic groups, and cofactors (as well as the corresponding electron transfer rates) of QFR, which are involved in the catalytic mechanism of the enzyme. The scheme shows that some of the involved electron transfer steps are endergonic and some are exergonic. Efficient tunneling of electrons is ensured due to the spatial proximity of the prosthetic groups and cofactors (Page *et al.*, 1999). This scheme has so far been incomplete due to the missing proper assignment of the two hemes with respect their position in the structure. The now accomplished assignment of the low-potential heme to the distal position and of the high-potential heme to the proximal position in the structure of QFR gives a precise picture of the electron transport chain of the *W. succinogenes* quinol:fumarate reductase.

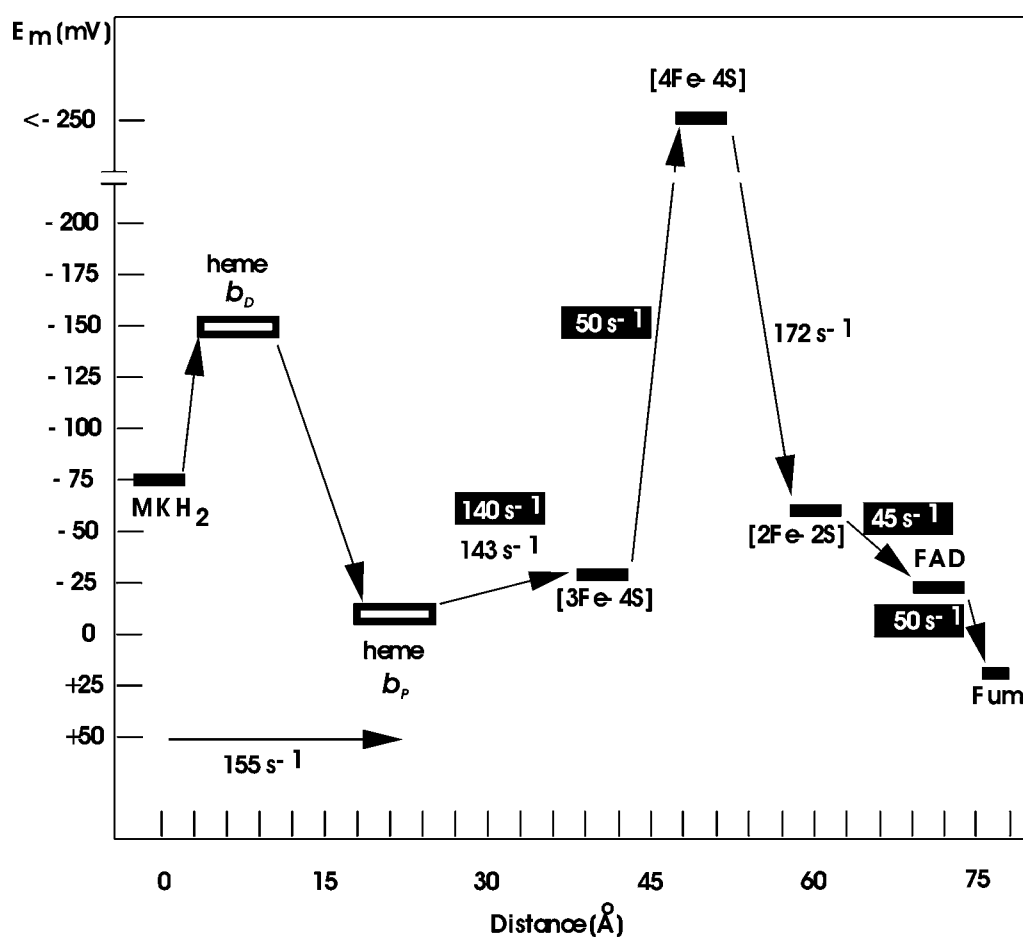


Figure 4.1: Oxidation-reduction potentials of the constituents of the ET chain of *W. succinogenes* QFR.

The distances are given in Ångstrom (Å) and refer to inter-cofactor distances. The equilibrium oxidation-reduction potentials are given in [mV] and refer to pH 7. Electron transfer rates in *white* are re-oxidation rates of the fully reduced enzyme by fumarate; those in *black* are reduction rates of the fully oxidized enzyme, as compiled in (Lancaster, 2004). The assignment of the hemes ($b_{Distal} \equiv b_{Low}$ and $b_{Proximal} \equiv b_{High}$) is indicated as obtained by simulated heme redox titrations in the study presented here. The experimental heme midpoint potentials are taken from ref. (Lancaster *et al.*, 2000), all others have been compiled in ref. (Lancaster, 2004).

4.1.3 Simulated heme reduction and affected ionization states as a function of pH

There are some drawbacks to the employed MCCE method: If one wants to describe the *in vivo* activity of an enzyme such as QFR, the catalytic mechanism is inevitably described unsatisfactorily by a method which considers static equilibrium states of the protein only, as the simulated redox states are at the utmost transiently populated *in vivo*. Yet this approach has proven to yield valuable results in other studies on other membrane bound enzymes before (see ref. Lancaster, 2003b for a recent review) and to be very useful in order to identify the potential importance and function of individual groups or residues and their possible interplay with respect to the enzymatic activity of the protein.

On the other hand, the evaluation of the employed static method can be completely different if it is compared to results from other static experimental methods such as electrochemical redox titrations in combination with methods like FTIR and UV/VIS spectroscopy (Moss *et al.*, 1990). Those types of experiments are more comparable to the results of electrostatic calculations, since they also deal with equilibrium states. Thus, the titrations simulated here are an ideal complement to the experimental redox titrations of the heme *b* groups of QFR (Lancaster *et al.*, 2000).

The results presented in Figure 3.4 show which residues of QFR undergo a change of their ionization state (as a function of pH) in response to the changed redox state of the two heme *b* groups of QFR. The observed changes reflect the putative importance of the involved groups or residues for the catalytic mechanism of QFR, especially in the framework of coupled electron and proton transfer. When discussing redox-related changes of the protonation state of Glu C180 with respect to the physiological activity of QFR enzyme, it is sensible to restrict the analysis to intermediate pH values, although data have been obtained from pH 0 to pH 14. In the intermediate pH range, the highly dominant contribution incorporates a single amino acid residue, which was identified to be Glu C180.

The change of protonation state of Glu C180 is directly related to the pK_a value of the particular residue in the four different modeled heme *b* redox states (see Figure 3.5), and the differences in pK_a directly come into play as the system is taken from one redox state to the next. Again, direct and indirect (via other residues that are influenced by the heme charges) interactions of residue Glu C180 with the reduced and especially oxidized heme species lead to different occupancies of neutral and ionized Glu C180 conformers in the different redox states. This adjustment of conformer distribution between neutral and ionized states is then

reflected in a changed pK_a value or, in other words, in protonation or deprotonation of the residue if a fixed pH value is considered as point of reference.

4.1.4 Reorientation of the Glu C180 side chain upon heme reduction

The results in Figure 3.4 and Figure 3.5 show net effects concerning the protonation state of Glu C180. But one major advantage of the multiconformation method is the possibility to study conformational changes of individual residues, as it has been described for Glu C180 in the results section (see Figure 3.6). This observed re-orientation upon reduction of the distal heme b_D is apparently mediated by the neighboring water molecules, as the effect could not be observed for model X (data shown in APPENDIX, Fig. 6.4). As mentioned before and indicated in Table 1, conformers “k” and “l” of Glu^- C180 have several stabilizing and destabilizing interactions with the conformers of water molecule W33 and, to a lesser extent, also with W11 in common. The presence of the two crystallographically determined water molecules in the vicinity of Glu C180 in model W increases the number of possible microstates that have to be considered in the Monte Carlo sampling. Thus, in contrast to model X, a scenario is created in which the energies of the different Glu C180 conformers are subjected to a more subtle selection and the resulting distinction is reflected in a pronounced dependency of the “intermediate” and “distal” conformations of Glu C180 with respect to the different heme b redox states. Another indication for the correctness and relevance of the two different side-chain conformations of Glu C180 was given by recent structural data on QFR WT enzyme at 1.78 Å resolution (C. R. D. Lancaster, *unpublished*), where significant electron density is observed for another side-chain conformation of Glu C180 that resembles the conformer which was created in the course of the MCCE calculations and which could not be resolved in the previous structure (1QLA) at 2.2 Å resolution.

The observed combination of (de)protonation and conformational changes of Glu C180 as a consequence of the modified heme redox states was also found from the comparison of electrochemically induced FTIR difference spectra on the wild-type enzyme and of a corresponding variant, in which the relevant amino acid residue Glu C180 has been replaced by a glutamine (see discussion of FTIR results below).

4.1.5 Protonation state of the ring C propionate of heme b_D

In addition to Glu C180, also the ring C propionate of the distal heme b group of QFR was suggested to be involved in the proposed “E-pathway” of QFR. Unfortunately, this could not readily be deduced from the presented simulations, since the obtained protonation states of all four heme propionates were very stable around neutral pH and did not change as a function of the heme redox states. Interestingly, the ring C propionate of the distal heme was the only one, which was calculated to be protonated in all investigated cases. The crystal structure 1QLA of QFR does not feature any water molecules in the vicinity of the ring C propionate of the distal heme. If water molecules would serve as proton donors and acceptors for this propionate in the tentative “E-pathway”, the lack of water sites in the model could be a possible reason why MCCE falls short of properly simulating protonation changes of the ring C propionate of QFR. In a recent electrostatics study on the bovine heart cytochrome c oxidase (Popović & Stuchebrukhov, 2004), the authors discuss a possible drawback of the continuum solvent model, which neglects the directed dipoles of explicit water molecules, to create artifacts in the form of strong salt bridges between the involved heme propionates and surrounding arginines. As a result, the propionates could not serve as pumping elements. In their simulations, the authors obtained coupling strengths of about 10 to 15 ΔpK units between the ionized propionates and arginines. Similar values were found in this study for the ionized heme propionates of QFR and the respective Arg⁺ and Lys⁺ residues (see Table 3.1). Furthermore, an estimation is made in ref. (Popović & Stuchebrukhov, 2004), which leads to the conclusion that the influence of water dipoles could indeed weaken a strong salt bridge, but unlikely to an extent which would result in deprotonation of the respective arginine/propionate pair and enable the propionate to accept a proton.

In the case of QFR, such strong salt bridges can be identified for the two propionates of the proximal heme and the ring D propionate of the distal heme (see Figure 3.2). For the ring C propionate of the distal heme, no evident acceptor for a salt bridge could be identified. Thus, the observed full protonation of this site could indicate that the ring C propionate might serve as a transient proton donor/acceptor of the proposed “E-pathway”. For this function, the residue does not necessarily need to exhibit different protonation in the various modeled redox states. The internal pK_{int} value of this propionate was calculated to be 15.5. Thus, it could easily donate a proton at neutral pH and be immediately re-protonated. Furthermore, as stated above, there are no relevant electrostatic interactions available for the ring C propionate of the distal heme to possibly stabilize an ionized equilibrium state.

In this line of argumentation, two other examples can be given: Glu L212 in the bacterial photosynthetic reaction centre (RC) is a key residue for proton transfer in this enzyme. In electrostatic calculations on the RC of *Rhodospseudomonas viridis* (Lancaster *et al.*, 1996), this residue is predominantly protonated in all modeled redox states, and the simulated proton uptake between the two states $DQ_A^-Q_B \rightarrow DQ_AQ_B^-$ is negligible at neutral pH, which is in line with FTIR measurements on this enzyme (Breton *et al.*, 1997; and Breton *et al.*, 1999). The second example is Glu 278 of the cytochrome *c* oxidase from *Paracoccus denitrificans*, which was found to be neutral at pH 7 for all simulated redox states in comparable electrostatic calculations (Kannt *et al.*, 1998) and in redox-induced FTIR difference spectra (Hellwig *et al.*, 1998 and 2002).

4.1.6 Implications for the E-pathway hypothesis

The obtained results and interpretation of the data with respect to transmembrane proton transfer via Glu C180, which is coupled to the redox states of the heme groups, strengthen the proposed model of catalytic action of QFR enzyme. The main aspect of the proposed “E-pathway” hypothesis (Lancaster, 2002b) is the existence of a transient proton transfer pathway in the QFR structure leading from the periplasm to the cytoplasm. A requirement of this hypothesis is that the “E-pathway” is active only upon reduction of the hemes but closed in the oxidized state. Two protons were suggested to be transferred via this pathway, which should compensate for the two protons that are released towards the periplasm via Glu C66 (Lancaster *et al.*, 2000) and the two protons, which are bound on the cytoplasmic side of QFR upon fumarate reduction (Lancaster *et al.*, 1999). The ionization state changes of Glu C180 can be interpreted as proton uptake and release that is directly coupled to the redox state of the distal and proximal heme. This observation under the applied conditions is consistent with *in vivo* proton translocation via Glu C180. Thus, the localization of Glu C180 and its strong interactions with the two heme groups give it the necessary characteristics to be the key element for the coupling of transmembrane electron transfer (via the hemes) to transmembrane proton transfer via the proposed “E-pathway”.

4.2 Spectroscopy

4.2.1 Comparison of QFR WT and variant FTIR difference spectra, and redox-induced conformational changes of the enzyme

QFR WT enzyme and three different variants from *Wolinella succinogenes* were investigated by electrochemically induced FTIR difference spectroscopy. The obtained IR data of WT and variant enzymes correspond very well and no major differences in the overall band pattern were observed (except for the presented differences that are related to the absence of protonated/deprotonated carboxylic acid groups in the three enzyme variants, as discussed below). This result underlines the consistency and the reproducibility of the “reduced-minus-oxidized” (and vice versa) difference spectra. The same consistency was also found for all spectra measured in D₂O.

For the enzyme variant E66Q, it was found via three-dimensional X-ray crystallography that this mutant does not feature significant structural changes with respect to the WT structure (both oxidized; Lancaster *et al.*, 2000 and 1999). Comparison of the FTIR difference spectra of the four presented enzyme types (see Figure 3.8) indicates that the conformational changes, which occur upon reduction, as judged by the difference signals in the amide I range, are the same for WT, E180Q, E66Q, and E270Q, respectively.

As mentioned above, all four enzyme types (WT and variants) have a relatively large redox-linked difference band in the amide I range in common, which features a zero-crossing at approximately 1663 cm⁻¹ (see Figure 3.8). This signal can be interpreted in terms of a conformational reorganization of the enzyme upon reduction. But the assignment is tentative as there is no crystal structure of the reduced form of QFR available so far. In a similar experiment on the heme-copper oxidases cytochrome *aa*₃ from *Rhodobacter sphaeroides* and the ubiquinol oxidase cytochrome *bo*₃ from *Escherichia coli*, which involved smaller absorbance changes (but a comparable total IR absorbance) upon redox reaction in the amide I region, the number of peptide bonds involved in a redox induced conformational change was estimated to be 3 to 5 (Lübber & Gerwert, 1996). Even if a comparable number of peptide bonds were involved in the redox-dependent conformational changes of QFR, it is not evident how noticeably the induced conformational change would affect the structure of QFR. Generally speaking, just very few peptide bonds could serve as a hinge and thus enable a movement of an otherwise rigid domain of the protein, and only those peptide bonds involved in the hinge region would be visible in the IR difference spectrum (Barth & Zscherp, 2002). A

possible candidate for such a domain movement in QFR is the capping domain in the hydrophilic subunit A, which has been shown to be susceptible for larger conformational changes (Lancaster *et al.*, 2001). In addition, when difference bands in the amide I region are assigned to conformational changes of the protein, it is possible that some (even large) conformational changes might contribute to the IR difference spectra in such a way that they cancel each other out, and hence the changes would not be adequately reflected in the IR difference spectrum (Barth & Zscherp, 2002). Thus, in the absence of additional information, such as the structure of the reduced QFR enzyme, the intensity of the involved difference bands is not sufficient to make a reliable statement about the extent of the underlying structural changes of QFR, which might be induced upon the redox reaction at the working electrode.

4.2.2 Effects of $^1\text{H}/^2\text{H}$ isotope exchange in QFR WT and implications for conformational changes

The $^1\text{H}/^2\text{H}$ isotope exchange behavior of QFR can serve as another possible source of information on conformational changes of the enzyme. This exchange occurs passively via diffusion and rinsing of the sample with a D_2O -based buffer but can also be actively influenced via redox induced conformational changes of the enzyme. Such exchange processes can be triggered electrochemically in the spectroelectrochemical cell and monitored with the help of FTIR spectroscopy.

All protein samples that have been prepared in D_2O buffer still contain a substantial amount of H_2O , although the samples have been thoroughly washed with D_2O before. This is reflected in the IR absorbance, which shows a residual H_2O infrared band at 1648 cm^{-1} (i.e., the H-O-H bending mode) of varying size depending on the individual preparation (see APPENDIX 6.2.5 and Fig. 6.9). When the experiment is started by taking IR spectra at oxidative and reductive potentials, the corresponding difference spectra reveal an unstable baseline that exhibits three broad bands (i.e., the H-O-H bending mode at 1648 cm^{-1} , a mixed H-O-D mode at 1456 cm^{-1} , and the D-O-D bending mode at 1210 cm^{-1} ; data shown in APPENDIX, Fig. 6.6) which directly show the decrease of H_2O and the increase of D_2O content in (and around) the area of the IR beam. Obviously, the induced redox reaction triggers further $^1\text{H}/^2\text{H}$ exchange in the enzyme via redox-dependent structural reorganizations of the protein. By this mechanism, H_2O molecules or protons, which are tightly bound in the oxidized state of the enzyme, are “loosened” and made accessible to $^1\text{H}/^2\text{H}$ exchange. This

interpretation would also be in line with the IR difference bands of QFR in the amide I region that have tentatively been assigned to redox-induced structural reorganizations of the enzyme (see Figure 3.8). With successive cycles of reduction and subsequent re-oxidation, the characteristic $^1\text{H}/^2\text{H}$ exchange bands decrease in size until they totally disappear. Stable baselines are subsequently observed for the remaining experimental session. Thus, a stable equilibrium has been reached and no further $^1\text{H}/^2\text{H}$ exchange can be induced. Yet the process of ongoing $^1\text{H}/^2\text{H}$ exchange in the spectroelectrochemical appears to be a “background reaction” with respect to the electrochemically induced redox reaction of QFR, since the observed difference spectra (baseline-corrected with respect to the $^1\text{H}/^2\text{H}$ exchange bands) do not significantly change upon progressive $^1\text{H}/^2\text{H}$ exchange. The described process of redox induced $^1\text{H}/^2\text{H}$ exchange has previously been observed and analyzed for the cytochrome *c* oxidase from *Paracoccus denitrificans* (Hellwig, 1998).

4.2.3 Analysis of the $\nu(\text{COOH})$ signals in QFR WT and variants

The focus of the presented study was to analyze possible contributions of protonated glutamic and aspartic acid residues to the FTIR difference spectra of QFR enzyme. In the context of coupled electron and proton transfer, it has been shown that the corresponding experimental results can yield extensive information about the underlying enzyme mechanism. The presented results can be compared and discussed with respect to other examples such as Glu278 of the cytochrome *c* oxidase from *Paracoccus denitrificans* (Hellwig *et al.*, 1998) or the corresponding Glu286 of cytochrome *bo₃* from *Escherichia coli* (Lübben *et al.*, 1999), and also Glu L212 in the photosynthetic reaction center of *Rhodobacter sphaeroides* (Hienerwadel *et al.*, 1995; and Nabadryk *et al.*, 1995). The respective band assignments in the cited studies were also accomplished with the help of site directed mutagenesis and $^1\text{H}/^2\text{H}$ isotope exchange.

The analysis of the band pattern of the IR difference spectra in the spectral region between approximately 1745 cm^{-1} and 1725 cm^{-1} indicates that there are contributions of several $\nu(\text{COOH})$ modes from acidic residues (see Figure 3.10 and Figure 3.12). This is plausible since the conservative substitution of the glutamate at position C180 with a glutamine modifies the observed signal of enzyme variant E180Q in comparison to the WT. Yet, a residual difference signal is observed at 1743 cm^{-1} for E180Q, showing that the band pattern in the WT enzyme around 1740 cm^{-1} has a more complex origin than only a single protonated side chain, namely that of Glu C180. The occurrence of this negative signal in the

“reduced-minus-oxidized” difference spectrum of enzyme variant E180Q indicates the protonation of at least one other Glu or Asp side chain upon oxidation of the enzyme. This assignment is supported by the observed sensitivity to $^1\text{H}/^2\text{H}$ isotope exchange of this band, which has already been mentioned.

The effect of the side chain exchange is that the high-frequency carbonyl stretching vibration of the protonated carboxyl group is lost since the C=O stretching vibration of the Gln side chain absorbs at considerably lower frequencies (around $\sim 1680\text{ cm}^{-1}$; Venyaminov & Kalnin, 1990) and a possible contribution of the introduced Gln could be heavily obscured by the dominating strong difference signal in the amide I range. Thus, if residue Glu C180 was the exclusive source of this specific difference signal, which appears in the course of the induced redox reaction, then there should be no observable signal left at all in the difference spectra in this particular frequency range upon removal of the protonatable group. The existence of several protonated carboxyl groups in the QFR enzyme also explains the slight broadening of the involved overlapping difference bands in D_2O (see inset of Figure 3.9) since the actual frequency shift upon $^1\text{H}/^2\text{H}$ isotope exchange might differ somewhat for different Asp or Glu sites within the enzyme. Furthermore, the discussed signals exhibit an increased intensity (around 1734 cm^{-1}) upon $^1\text{H}/^2\text{H}$ isotope exchange. The simplest explanation for this observation is that the overlapping bands increase the IR absorbance at the specific wavenumber. A slight increase of the involved extinction coefficients upon deuteration is also expected (Barth, 2000). Another possibility is that the pK_a value of the involved group(s) is changed in D_2O (Hellwig *et al.*, 1999a).

4.2.4 The pH-dependence of the observed $\nu(\text{COOH})$ signals in QFR WT

The pH-dependence of the FTIR difference signals of QFR WT enzyme above 1715 cm^{-1} (see Figure 3.12) indicates that numerous groups are involved in the signal pattern, thus making it difficult to perform a detailed deconvolution of the observed signals. The fact that there are contributions of protonated glutamic and/or aspartic amino acid side chains at pH values up to pH 8.8 demonstrates the capability of the local protein environment to stabilize protonated groups at elevated pH values which usually have pK values of around 4 in aqueous solution (Baymann *et al.*, 1999).

4.2.5 Hydrogen bonding strength of the observed $\nu(\text{COOH})$ signals

The discussed difference signals around 1740 cm^{-1} (see Figure 3.10) are indicative for protonated carboxyl groups that are moderately hydrogen-bonded and are likely to be situated inside the protein, and which are thus also not directly accessible to intense hydrogen-bonding with the solvent. Without any hydrogen bonds, frequencies above 1740 cm^{-1} are expected (Barth & Zscherp, 2002). For example, the vibration of a protonated Asp side chain without any noticeable hydrogen bond in its protein environment has been observed at 1762 cm^{-1} (Fahmy *et al.*, 1993). A single hydrogen bond might cause a frequency decrease of 25 cm^{-1} for the involved vibration, or even up to 50 cm^{-1} for strong hydrogen bonding (Barth, 2000). In general, the more surface exposed a protonated carboxyl group is, the lower is the frequency of the $\nu(\text{C=O})$ carbonyl stretching vibration. Even signals at 1694 cm^{-1} have tentatively been assigned to $\nu(\text{C=O})$ modes of Asp or Glu side chains (Hellwig *et al.*, 1999a and 1999d).

The position of the FTIR difference signal, which has been assigned to residue Glu C180, is consistent with its location in the three-dimensional structure of QFR as it is located near the center of transmembrane helix V and thus buried in the hydrophobic part of QFR, apparently inaccessible to bulk solvent.

4.2.6 Analysis of QFR WT and variant double-difference spectra

Provided the conditions of the induced reactions are always identical, subtracting the difference spectra of QFR WT and the corresponding variant enzymes yields double-difference spectra in which - in the ideal case - the remaining signal can solely be attributed to the differences that were induced by the single mutation. In this study, the effects of replacing Glu residues with Gln were investigated. In the context of the “E-pathway” hypothesis, Glu C180 is the key element. Thus, in order to check the protonation state of this particular residue, which is supposedly affected by the induced electrochemical redox reaction, the analysis of the resulting (double) differences is focused on the exposed IR signal of the protonated carboxyl group, since this characteristic vibration is effectively lost in the variant enzyme E180Q.

The double-difference spectra “WT-minus-E66Q” and “WT-minus-E270Q” basically support the finding that WT, E66Q, and E270Q signals are very comparable. The observable non-zero signals in the double-difference spectra of “WT-minus-E66Q”, which peak around

1722 cm^{-1} , may be attributed to the almost inevitable mismatch of spectra from different experiments which can not be overcome by simple adjustment of scaling. However, it cannot be excluded that the residual signal in the “WT-minus-E66Q” double-difference spectrum is indeed significant and reflects protonation or environmental changes of amino acid residue Glu C66.

In the case of the “WT-minus-E270Q” double-difference spectrum, the residual non-zero signal is negligible. Hence, it can be ruled out that Glu A270 undergoes any significant protonation changes within the framework of the performed experiment.

In contrast, the experiment with the enzyme variant E180Q shows that the protonation state of Glu C180 is directly related to the changed redox state of the heme groups (see Figure 3.10 and Figure 3.11c). The double-difference spectrum that has been calculated for WT QFR and enzyme variant E180Q data reflects the contribution of the individual amino acid residue Glu C180 to the QFR WT signal. The signal pattern of the “reduced-minus-oxidized” double-difference spectrum shows a maximum at 1741 cm^{-1} and a minimum at 1734 cm^{-1} , and both bands are related to residue Glu C180.

The possible origins for the observed difference signals are generally deprotonation and protonation of acidic amino acid residues or environmental changes or a superposition of both. For example, a full deprotonation of a previously fully protonated Glu or Asp side chain due to the electrochemically induced redox reaction would be reflected in the absence of the respective vibration above 1710 cm^{-1} in the FTIR spectrum of the final state, leading to a negative signal in the corresponding difference spectrum. An environmental change around protonated Glu or Asp residues would shift the respective band and thus yield a positive and negative signal of equal area (this assumes that the extinction coefficient does not change in the process) in the corresponding difference spectrum. Finally, the sign of the difference band is indicative for its affiliation to the initial (negative) or final (positive) state of the reaction.

Thus, in a basic approach, the two difference bands in the double-difference spectrum “WT-minus-E180Q” can be analyzed with respect to their spectral position, sign, and area. The wavenumber is determined by the origin of the vibration, and values of 1741 cm^{-1} and 1734 cm^{-1} are in line with vibration frequencies of protonated Asp or Glu side chains (Venjaminov & Kalnin, 1990). The difference of the two numerical values (in the present case approximately 7 cm^{-1}) reflects the intensity of the induced environmental change. As mentioned above, a single H-bond can cause a decrease of 25 cm^{-1} (Barth, 2000). The area, which is enclosed by the positive and negative difference bands in the “WT-minus-E180Q” double-difference spectrum, is not equal. Therefore, the most probable interpretation would

be that amino acid residue Glu C180 undergoes a change of protonation state in the course of the induced redox reaction, which is superimposed by an environmental change of its hydrogen-bonding pattern. This proposed superimposition is plausible if the experiment (pH 7) is performed near the apparent pK_a value, which, as shown experimentally, depends on the redox state of the enzyme (i.e., the applied electrode potential). Based on the “reduced-minus-oxidized” difference spectra, this means that a certain fraction of Glu C180 side chains in the population of all QFR molecules experiences complete protonation upon reduction of the hemes, whereas the remaining fraction is still protonated in the oxidized state but with a different hydrogen-bonding environment. Estimated from the amplitude of the negative peak at 1734 cm^{-1} in the “reduced-minus-oxidized” double-difference spectrum, the fraction of Glu C180, which is protonated in the oxidized state, seems to be comparatively small with respect to the deprotonated form. The obtained result of a combination of a conformational change and proton uptake by Glu C180 is strongly supported by the performed multiconformation continuum electrostatics (MCCE) calculations as previously discussed.

4.2.7 FTIR difference spectroscopy on QFR with ^{13}C -labeled heme propionates

The obtained FTIR spectroscopic results based on ^{13}C -labeling of the QFR heme propionates clearly indicate an involvement of at least one of the two propionate groups of the low potential distal heme b_D of QFR in the electrochemically induced redox reaction. This is reflected in contributions of the protonated and deprotonated forms of the respective group(s) to the computed “unlabeled-minus-labeled” QFR double-difference spectra.

4.2.7.1 Tentative vibrations of protonated heme propionates

Above 1700 cm^{-1} , similar and rather broad contributions are observed in the FTIR double-difference spectra for the full potential, and for the “reduced-minus-intermediate” potential step, which might be assigned to vibrations of protonated heme propionate(s) of b_D and which are shifted to lower wavenumbers where they are heavily obscured by other vibrations (i.e., the amide I and the strong water absorbance, which are both centered around 1650 cm^{-1}) upon ^{13}C -labeling. Based on observations from multiple independent experiments on the unlabeled QFR WT enzyme, the signal around 1718 cm^{-1} appears to be more susceptible for amplitude variations. Although frequencies above 1710 cm^{-1} would be very high for a $\nu(\text{COOH})$ heme propionate vibration (Behr *et al.*, 1998), the results obtained in this

study indicate a frequency for a propionate carboxyl group vibration which is in the range of Glu or Asp $\nu(\text{COOH})$ modes. The apparent differences between the labeled and unlabeled QFR in this range are very likely related to the ^{13}C -labeling of the heme propionates, if experimental errors such as insufficient equilibration or pH effects can be excluded. The observed frequencies are very high for propionate contributions. Yet this is conceivable if the local environment of the specific propionate is very hydrophobic so that it is not hydrogen-bonded, enabling the observed high frequency for the $\nu(\text{COOH})$ mode. In principle, such a scenario is covered by the particular position and environment of the ring C propionate of b_D as it is oriented parallel to the membrane plane inside the hydrophobic subunit (and not along the membrane normal as the other propionates, see Figure 1.6 and Figure 3.6). Thus, it is feasible that the observed difference signals above 1710 cm^{-1} contain (ring C) heme propionate contributions, which indicates a redox-coupled protonation change and/or an environmental change of a propionate group of b_D . Yet it remains difficult to explain the entire spectral features in terms of heme propionate vibrations, and additional effects arising from scaling errors cannot be excluded presently.

4.2.7.2 Tentative anti- and symmetric vibrations of deprotonated heme propionates

The distinct series of positive and negative double-difference bands in the frequency range between 1560 cm^{-1} and 1500 cm^{-1} are more reliable to discuss, and they are indicative of antisymmetric $\nu_{\text{as}}(\text{COO}^-)$ vibrations of deprotonated heme propionates and/or environmental changes (e.g., due to a redox-coupled conformational change of the propionate group resulting in a different coordination of the oxygen atoms) of the respective groups. The band pattern is too complicated for a simple downshift of a single deprotonated heme propionate mode upon ^{13}C -labeling, and hence the observed pattern points out combined redox-effects. As inferred from the crystal structure of QFR and rationalized by the electrostatic calculations presented in this work, the ring D propionate of the distal heme b_D is engaged in a salt bridge with the positively charged Arg C162. Thus, the spectroscopic results could be due to a superposition of a (de)protonation event and/or environmental changes on the ring C propionate of the low-potential distal heme b_D , and an environmental change of the ring D propionate, which might reflect a variation in the strength of the salt bridge, for instance. Corresponding mandatory signals for the symmetric $\nu_{\text{s}}(\text{COO}^-)$ vibrations are present in the double-difference spectra in the frequency range between 1410 cm^{-1} and 1360 cm^{-1} , but they are more pronounced in the full potential step, where the agreement between the sign of

the tentative antisymmetric and symmetric contributions is better (in principle, the sign of the respective signals should be the same). Possible reasons for the discrepancy shall be discussed in the following paragraph.

4.2.7.3 Differences between the full and partial potential step for b_D

It is assumed that the spectral features in the double-difference spectra of the full and the low-potential step arise from the heme propionates of (the low-potential) heme b_D . The observed discrepancies that are visible for the two steps could be due to the different reference potentials “intermediate” and “oxidized”, respectively. At the intermediate potential, the (high-potential) proximal heme b_P is still reduced, and *only* heme b_D is oxidized. At the oxidizing potential, *both* hemes are fully oxidized. Hence, it is feasible that the redox state of the proximal heme influences the redox transition of the distal heme b_D . In the electrostatic calculations, the two oxidized hemes destabilize each other by 0.6 ΔpK units (cf. Table 3.1 in chapter 3.1.1), whereas the interactions with and among the reduced heme species are negligible. Thus, it is conceivable that the different redox state of the proximal heme b_P has a noticeable influence (minor frequency shifts and/or intensity variations, as can be seen in Figure 3.17) on the vibrations of the ionized propionates of the oxidized distal heme b_D .

The absence of significant contributions from the propionates of the high-potential proximal heme b_P is in line with the result from the electrostatic calculations that both propionates are involved in stable salt bridges and consequently not available for redox-driven proton transfer. For the distal heme b_D , it is assumed that the ring C propionate is the dominating source for the observed double-difference bands. An additional contribution of the ring D propionate of b_D cannot be ruled out at present, although it would be restricted to an environmental change (due to the salt bridge, which was identified in the MCCE calculations).

The interpretation of the obtained experimental data associated with the distal heme b_D , and particularly with the ring C propionate, in terms of a (de)protonation event possibly accompanied by an environmental effect, which could well be a conformational change, agrees very well with the suggested role of this propionate in the proposed “E-pathway” hypothesis of coupled transmembrane electron and proton transfer (Lancaster, 2002b).

4.2.8 Analysis of the observed redox Bohr effect

In recent studies, redox Bohr effects were also observed in the succinate dehydrogenase (SDH) from *Rhodothermus marinus* (Fernandes *et al.*, 2001), and in the quinol:fumarate (oxido)reductase from *Desulfovibrio gigas* (Lemos *et al.*, 2002a). Both enzymes, reviewed in (Lemos *et al.*, 2002b), are phylogenetically related to the quinol:fumarate reductase (QFR) from *Wolinella succinogenes* as all three succinate:quinone oxidoreductases are classified as “type B” enzymes (Lancaster, 2002a) with respect to their heme content and (hydrophobic) subunit composition (Hederstedt, 1999). The observed pH-dependence of the heme midpoint potentials for QFR WT are comparable to the ones obtained for the QFR from *D. gigas*, indicating similarities between the two enzymes with respect to the redox Bohr effect in the WT enzyme. The *R. marinus* SDH has much higher heme midpoint potentials than the QFRs from *W. succinogenes* and *D. gigas*, and a redox Bohr effect could only be quantified for heme b_L . Unfortunately, no amino acid sequence or three-dimensional structure is presently available for the *D. gigas* and *R. marinus* enzymes, which makes it difficult to compare the three systems more thoroughly, and hence the discussion will exclusively focus on the results obtained in this study.

4.2.8.1 Redox Bohr effect in WT QFR and the role of the ring C propionate of heme b_D

The observation of a redox Bohr effect of the heme groups indicates the presence of protolytic residues in the vicinity of the hemes. For heme groups, apparently, the heme propionates and their corresponding redox-dependent (de)protonation could be causative for the effect. Yet the description of the redox Bohr effect does not imply assumptions on the actual distance between the site of oxidation-reduction and the site of protonation-deprotonation. Thus, the effect can be considerably delocalized (Louro *et al.*, 1996).

Based on the analysis of the crystal structure of the *W. succinogenes* QFR (Lancaster *et al.*, 1999) and the performed electrostatic calculations discussed above, it was found that all heme propionates, except for the ring C propionate of the distal heme b_D , are engaged in salt bridges with protonated Arg or Lys residues at pH 7. Effectively, a pair of residues connected via a salt bridge “shares” one proton and behaves as a single titratable site (Popović & Stuchebrukhov, 2004). The strength of a salt bridge is sensitive to the ambient pH and might also depend on the redox state of the heme group. As a result of electrostatic calculations on *W. succinogenes* QFR, the observed salt bridges appeared to be stable around neutral pH,

independent of the heme redox state, whereas the ring C propionate of the distal heme was found to be protonated. Although the general finding of three salt-bridged heme propionates and a protonated fourth in QFR is in line with the experimental data, the constant protonation of the ring C propionate of heme b_D at neutral pH does not fully agree with the experimental results since the observed redox Bohr effect as well as the performed ^{13}C -labeling indicates protonation changes of this propionate. A possible explanation for this discrepancy is the conformational rigidity of the polypeptide backbone of the QFR model in the MCCE calculations. Also the presence (or rather the absence) of particular crystallographic water molecules might significantly influence the results of the calculations.

Nonetheless, as inferred from the crystal structure of the oxidized QFR (Lancaster *et al.*, 1999), the ring C propionate of heme b_D is kinked and points somewhat inwards, almost parallel to the membrane surface, in the direction of the proposed “E-pathway”, whereas the three salt-bridged heme propionates point approximately in the direction of the membrane surface. Thus, in conclusion, only the ring C propionate of heme b_D is available for protonation around neutral pH in the *Wolinella succinogenes* QFR, and it is unlikely that the three salt-bridged heme propionates are predominantly responsible for the observed redox Bohr effect of the heme groups. Further contributions of other protolytic groups, even farther from the heme groups, are conceivable. A likely candidate is the residue Glu C180, which is about 12 to 13 Å away from the iron atoms of the heme groups.

4.2.8.2 Redox Bohr effect in variant E180Q and the role of Glu C180 in the WT

The enzymatic activity of the E180Q variant is not detectable in the membrane-bound state, and it is approximately a tenth of the QFR WT activity at neutral pH in the detergent-solubilized state (Sauer, 2001). For the enzyme variant E180Q, this observation could possibly be explained *in vivo*, if it is assumed that an ambient membrane potential is present in the membrane-bound state. Consequently, the electrons had to be transferred towards the negative side of the membrane (against the potential). The difference of the midpoint potentials of the hemes at pH 7 is 39 mV for the high-potential, and 4 mV for the low-potential heme. According to the quantitative model for intra-protein electron transfer rates proposed in ref. (Page *et al.*, 1999), it can be estimated that in the detergent-solubilized variant E180Q, the maximum rate of electron transfer from the proximal heme to the [3Fe-4S] cluster is 38 % of the WT rate due to the elevated midpoint potential of the high-potential heme in the variant.

The FTIR spectroscopic results described here, as well as the electrostatic calculations on the *Wolinella succinogenes* QFR show that the protonation state and the side-chain orientation of Glu C180 depend on the heme redox state, and that Glu C180 electrostatically interacts with the two heme *b* groups, which is in line with the observed redox Bohr effect. Furthermore, as inferred from the “E-pathway” hypothesis, the suggested redox-switch for coupled transmembrane electron and proton transfer, namely Glu C180, is not functional in the variant. This also agrees with the results mentioned above from FTIR spectroscopy and MCCE calculations.

The pronounced differences found for WT and E180Q (see Figure 3.18) indicate unequivocally that Glu C180 is involved in the pH-dependence of the heme midpoint potentials due to redox-coupled (de)protonation and/or environmental changes of this residue. The discrepancy between pK_{ox} and pK_{red} for WT and E180Q, respectively, is considerably stronger for the high-potential “proximal” heme than for the low-potential “distal” heme. In the variant E180Q, the high-potential heme is much harder to oxidize at pH values above pH 5.5. This indicates that the invariably neutral charge on the side chain of the Gln C180 in the variant, which mimics the Glu C180 in its neutral protonated state, stabilizes the reduced state of the proximal heme. The asymmetry of the impact of the mutation E180Q on the heme redox behavior might be related to the observed conformational change of Glu C180, which occurs in a concerted manner with respect to proton uptake upon reduction of the hemes. This redox-related conformational change of the Glu C180 side chain was theoretically predicted as a result of the performed electrostatic calculations (cf. chapter 3.1.7), and could experimentally be confirmed by electrochemically induced FTIR difference spectroscopy on the *W. succinogenes* WT, and the variant enzyme E180Q (presented earlier in this work). Most probably, the Gln C180 side chain in the variant is locked in an orientation, which is similar to the one of Glu C180 in the protonated state. In addition, the proximal heme is inevitably harder to re-oxidize in the variant since the Gln C180 cannot be deprotonated to electrostatically ease the re-oxidation of heme *b_p* as it is conceivable for the residue Glu C180 in the WT. Consequently, as observed experimentally, the activity of the enzyme variant E180Q is substantially decreased compared to the WT.

4.2.8.3 Consequences of the observed redox Bohr effect on heme b_P in QFR variant E180Q for the “E-pathway”

The observation of a redox Bohr effect in the variant E180Q also proves that Glu C180 is not the only protolytic group responsible for the pH-dependence of both heme groups of QFR (and especially of heme b_P). For the low-potential heme the differences in the variant might be less pronounced because the ring C propionate of this heme is assumed to be the dominating protolytic site for b_D . The redox Bohr effect on the high-potential heme in the variant yields evidence for the presence of further protolytic groups, which interact with heme b_P in the WT enzyme in addition to Glu C180 and which could also be a further presently unidentified constituent of the “E-pathway”. This is in line with the “E-pathway” hypothesis, since Glu C180 and the ring C propionate of heme b_D alone would presumably not suffice for efficient proton transfer across the bacterial membrane.

4.3 Conclusions

- 1.) The simulation of heme *b* redox titrations agreed very well with the corresponding experimental (VIS) titrations, and this high correspondence also allowed the assignment of the high and low heme *b* midpoint potentials to the proximal and distal positions in the *Wolinella succinogenes* QFR structure, respectively. In addition, the results of the simulations provided an explanation for the observed difference in midpoint potential for heme *b_D* and *b_P*, which results from the higher loss of reaction field energy for the proximal heme, and the stronger destabilization of the oxidized form of the proximal heme due to several buried and ionized Arg and Lys residues.
- 2.) The results of electrochemically induced FTIR and VIS difference spectroscopy and theoretical MCCE calculations presented here indicate that the protonation state of Glu C180 and its side-chain conformation depend on the redox state of the heme *b* groups of QFR enzyme. An additional side-chain conformation of Glu C180, which resembles the one identified in the calculations, was recently observed in a crystal structure of QFR of higher resolution than the original 2.2 Å (C. R. D. Lancaster, *unpublished*). Furthermore, from the observation of a different behavior of QFR WT and variant E180Q with respect to a redox Bohr effect on heme *b_P*, it was concluded that Glu C180 is one of the groups which control the observed effect on heme *b_P*.
- 3.) Similar results were obtained for the propionates of the distal heme. Although it was systematically not possible to distinguish between the two propionates of heme *b_D* in the spectroscopic experiments, structural and computational considerations make a contribution of the heme *b_D* ring D propionate very unlikely, as this group is connected to Arg C162 via a salt bridge. Since the unusual, full protonation state of the ring C propionate of heme *b_D* was calculated to be stable throughout the simulated heme redox states, possible improvements of the model employed (e.g., further water molecules) should be considered, which could stabilize a (partially) deprotonated ring C propionate when heme *b_D* is

oxidized. However, the conclusion is that it is indeed the ring C propionate, which contributes to the FTIR difference signal. This is also in line with the observed redox Bohr effect on heme b_D . It is inferred that the pH-dependence of the distal heme is dominated by the ring C propionate of b_D .

- 4.) Thus, the results support the “E-pathway” hypothesis of coupled transmembrane electron and proton transfer in *W. succinogenes* QFR in that the two acidic residues, Glu C180 and the ring C propionate of b_D , have the necessary characteristics to be constituents of a redox-controlled proton transfer pathway.
- 5.) The assignment of at least part of the electrochemically induced IR difference signal of WT QFR to Glu C180 and the heme propionates of the distal heme required site-directed mutagenesis, site-specific ^{13}C -labeling as well as $^1\text{H}/^2\text{H}$ isotope exchange and signal separation via appropriate reference potentials. Other assignments are merely tentative and further experiments are necessary. Even without a full assignment of all the involved difference signals, the respective IR difference spectra can be viewed as a “characteristic fingerprint” (Barth & Zscherp, 2002) of the investigated enzyme, with the obtained spectra being representative for QFR from *Wolinella succinogenes* and the enzymatic redox reaction which has been induced electrochemically in the spectroelectrochemical cell.
- 6.) In the future, the spectroscopic investigation of further enzyme variants of QFR could help to identify further possible constituents of the “E-pathway”. Also for the MCCE calculations there are possibilities for improvement, as it would be worthwhile trying to extend the model to the full dimeric QFR structure and also to include a reliable menaquinone model in the identified binding site. Furthermore, the obtained results could be refined by using a structure determined at higher resolution, which was not available when the project was initiated. The next stage of desirable experiments and simulations would also include the kinetic study of the catalytic mechanism of QFR with the help of kinetic spectroscopy and the so-called computational “Q-HOP” method (Lill & Helms, 2001) for the simulation of intra-protein proton transfer.

5 REFERENCES

Adam, G., Lauger, P., and Stark, G. (1995) Chemiosmotische Theorie der oxidativen Phosphorylierung und Photophosphorylierung, in *Physikalische Chemie und Biophysik*, 3rd ed., Springer-Verlag, Berlin, Heidelberg, New York.

Alexov, E. G., and Gunner, M. R. (1997) Incorporating protein conformational flexibility into the calculation of pH-dependent protein properties, *Biophys. J.* 74, 2075–2093.

Alexov, E. G., and Gunner, M. R. (1999) Calculated protein and proton motions coupled to electron transfer: electron transfer from Q_A^- to Q_B in bacterial photosynthetic reaction centers, *Biochemistry* 38, 8253–8270.

Allen, J. F., and Holmes, N. G. (1986) Electron transport and redox titration, in *Photosynthesis, Energy Transduction, A Practical Approach* (Hipkins, M. F., and Baker, N. R., Eds.) pp 103–141, IRL Press, Oxford, Washington DC.

Barth, A. (2000) The infrared absorption of amino acid side chains, *Prog. Biophys. Mol. Biol.* 74, 141–173.

Barth, A., and Zscherp, C. (2002) What vibrations tell about proteins, *Quart. Rev. Biophys.* 35, 369–430.

Baymann, F., Robertson, D. E., Dutton, P. L., and Mantele, W. (1999) Electrochemical and spectroscopic investigations of the cytochrome bc_1 complex from *Rhodobacter capsulatus*, *Biochemistry* 38, 13188–13199.

Behr, J., Hellwig, P., Mantele, W., and Michel, H. (1998) Redox dependent changes at the heme propionates in cytochrome *c* oxidase from *Paracoccus denitrificans*: direct evidence

from FTIR difference spectroscopy in combination with heme propionate ^{13}C labeling, *Biochemistry* 37, 7400–7406.

Beinert, H. (2000) Iron-sulfur proteins: ancient structures, still full of surprises, *J. Biol. Inorg. Chem.* 5, 2–15.

Beroza, P., Fredkin, D. R., Okamura, M. Y., Feher, G. (1991) Protonation of interacting residues in a protein by a Monte Carlo method: application to lysozyme and the photosynthetic reaction center of *Rhodobacter sphaeroides*, *Proc. Natl. Acad. Sci. USA* 88, 5804–5808.

Berthomieu, C., Boussac, A., Mäntele, W., Breton, J., and Navedryk, E. (1992) Molecular changes following oxidoreduction of cytochrome *b559* characterized by Fourier transform infrared difference spectroscopy and electron paramagnetic resonance: photooxidation in photosystem II and electrochemistry of isolated cytochrome *b559* and iron protoporphyrin IX-bisimidazole model compounds, *Biochemistry* 31, 11460–11471.

Biel, S., Simon, J., Groß, R., Ruiz, T., Ruitenber, M., and Kröger, A. (2002) Reconstitution of coupled fumarate respiration in liposomes by incorporating the electron transport enzymes isolated from *Wolinella succinogenes*, *Eur. J. Biochem.* 269, 1974–1983.

Bohr, C., Hasselbalch, K. A., and Krogh, A. (1904) Über einen in biologischer Beziehung wichtigen Einfluss, den die Kohlensäurespannung des Blutes auf dessen Sauerstoffbindung übt, *Skand. Arch. Physiol.* 16, 402–412.

Breton, J., Berthomieu, C., Thibodeau, D. L., and Navedryk, E. (1991a) Probing the secondary quinone (Q_B) environment in photosynthetic bacterial reaction centers by light-induced FTIR difference spectroscopy, *FEBS Lett.* 288, 109–113.

Breton, J., Bauscher, M., Berthomieu, C., Thibodeau, D., Andrianambinintsoa, S., Dejonghe, D., Mäntele, W., and Navedryk, E. (1991b) FTIR difference spectroscopy of menaquinone photoreduction in bacterial reaction centers, in *Spectroscopy of Biological*

Molecules (Hester, R. E., and Girling, R. B., Eds.) pp 43–46, The Royal Society of Chemistry, Cambridge, UK.

Breton, J., Boullais, C., Berger, G., Mioskowski, C., and Nabedryk, E. (1995) Binding sites of quinones in photosynthetic bacterial reaction centers investigated by light-induced FTIR difference spectroscopy: symmetry of the carbonyl interactions and close equivalence of the Q_B vibrations in *Rhodobacter sphaeroides* and *Rhodospseudomonas viridis* probed by isotope labeling, *Biochemistry* 34, 11606–11616.

Breton, J., and Nabedryk, E. (1996) Protein-quinone interactions in the bacterial photosynthetic reaction center: light-induced FTIR difference spectroscopy of the quinone vibrations, *Biochim. Biophys. Acta* 1275, 84–90.

Breton, J., Nabedryk, E., Allen, J. P., and Williams, J. C. (1997) Electrostatic influence of Q_A reduction on the IR vibrational mode of the 10a-ester C=O of H_A demonstrated by mutations at residues Glu L104 and Trp L100 in reaction centers from *Rhodobacter sphaeroides*, *Biochemistry* 36, 4515–4525.

Breton, J., Bibikova, M., Oesterhelt, D., and Nabedryk, E. (1999) Conformational heterogeneity of the bacteriopheophytin electron acceptor H_A in reaction centers from *Rhodospseudomonas viridis* revealed by Fourier transform infrared spectroscopy and site-directed mutagenesis, *Biochemistry* 38, 11541–11552.

Brudler, R., de Groot, H. J. M., van Liemt, W. B. S., Gast, P., Hoff, A. J., Lugtenburg, J., and Gerwert, K. (1995) FTIR spectroscopy shows weak symmetric hydrogen bonding of the Q_B carbonyl groups in *Rhodobacter sphaeroides* R26 reaction centres, *FEBS Lett.* 370, 88–92.

de Levie, R. (2003) The Henderson-Hasselbalch equation: its history and limitations, *J. Chem. Educ.* 80, 146–146.

Dunbrack, R. L., and Karplus, M. (1994) Conformational analysis of the backbone-dependent rotamer preferences of protein side-chains, *Nature Struct. Biol.* 1, 334–340.

Dunbrack, R. L., and Cohen, F. E. (1997) Bayesian statistical analysis of protein side-chain rotamer preferences, *Protein Sci.* 6, 1661–1681.

Dutton, P. L. (1978) Redox potentiometry: determination of midpoint potentials of oxidation-reduction components of biological electron-transfer systems. *Meth. Enz.* 54, 411–435.

Fabian, H., and Mäntele, W. (2002) Infrared spectroscopy of Proteins, in *Handbook of Vibrational Spectroscopy* (Chalmers, J. M., and Griffiths, P. R., Eds.) Vol. 5, pp 3399–3425, John Wiley & Sons, Ltd., Chichester.

Fahmy, K., Weidlich, O., Engelhard, M., Sigrist, H., Siebert, F. (1993) Aspartic acid-212 of bacteriorhodopsin is ionized in the M and N photocycle intermediates - an FTIR study on specifically ^{13}C -labeled reconstituted purple membranes, *Biochemistry* 32, 5862–5869.

Fernandes, A. S., Pereira, M. M., and Teixeira, M. (2001) The succinate dehydrogenase from the thermohalophilic bacterium *Rhodothermus marinus*: redox-Bohr effect on heme b_L, *J. Bioenerg. Biomemb.* 33, 343–352.

Foerstendorf, H., Mummert, E., Schäfer, E., Scheer, H., and Siebert, F. (1996) Fourier-transform infrared spectroscopy of phytochrome: difference spectra of the intermediates of the photoreactions, *Biochemistry* 35, 10793–10799.

Geisler, V., Ullmann, R., and Kröger, A. (1994) The direction of the proton exchange associated with the redox reactions of menaquinone during the electron transport in *Wolinella succinogenes*, *Biochim. Biophys. Acta* 1184, 219–226.

Georgescu, R. E., Alexov, E. G., and Gunner, M. R. (2002) Combining conformational flexibility and continuum electrostatics for calculating pK_as in proteins, *Biophys. J.* *83*, 1731–1748.

Gilson, M. K., and Honig, B. (1986) The dielectric constant of a folded protein, *Biopolymers* *25*, 2097–2199.

Glasoe, P. K., and Long, F. A. (1960) Use of glass electrodes to measure acidities in deuterium oxide, *J. Phys. Chem* *64*, 188–190.

Gries, C., Hellwig, P. and Mäntele, W. (1997) Spectroelectrochemical investigations of cytochrome *c* oxidase on chemically modified semitransparent electrodes by FTIR-spectroscopy, in *Spectroscopy of Biological Molecules: Modern Trends* (Carmona, P., Navarro, R., and Hernanz, A., Eds.), Kluwer Academic Publishers.

Gunner, M. R., and Honig, B. (1991) Electrostatic control of midpoint potentials in the cytochrome subunit of the *Rhodospseudomonas viridis* reaction center, *Proc. Natl. Acad. Sci. USA* *88*, 9151–9155.

Gunner, M. R., and Alexov, E. G. (2000) A pragmatic approach to structure based calculations of coupled proton and electron transfer in proteins, *Biochim. Biophys. Acta* *1458*, 63–87.

Hägerhäll, C., Fridén, H., Aasa, R., and Hederstedt, L. (1995) Transmembrane topology and axial ligands to hemes in the cytochrome *b* subunit of *Bacillus subtilis* succinate:menaquinone reductase, *Biochemistry* *34*, 11080–11089.

Hägerhäll, C., and Hederstedt, L. (1996) A structural model for the membrane-integral domain of succinate:quinone oxidoreductases, *FEBS Lett.* *389*, 25–31.

Hägerhäll, C. (1997) Succinate:quinone oxidoreductases - variations on a conserved theme, *Biochim. Biophys. Acta* 1320, 107–141.

Hederstedt, L. (1999) Respiration without O₂, *Science* 284, 1941–1942.

Hellwig, P., Rost, B., Kaiser, U., Ostermeier, C., Michel, H., and Mänteles, W. (1996) Carboxyl group protonation upon reduction of the *Paracoccus denitrificans* cytochrome *c* oxidase: direct evidence by FTIR spectroscopy, *FEBS Lett.* 385, 53–57.

Hellwig, P. (1998) Elektronen- und Protonentransfer in der Cytochrom *c* Oxidase von *Paracoccus denitrificans*, PhD thesis, University of Erlangen, Germany.

Hellwig, P., Behr, J., Ostermeier, C., Richter, O.-M. H., Pfitzner, U., Odenwald, A., Ludwig, B., Michel, H., and Mänteles, W. (1998) Involvement of glutamic acid 278 in the redox reaction of the cytochrome *c* oxidase from *Paracoccus denitrificans* investigated by FTIR spectroscopy, *Biochemistry* 37, 7390–7399.

Hellwig, P., Soulimane, T., Buse, G., and Mänteles, W. (1999a) Similarities and dissimilarities in the structure-function relation between the cytochrome *c* oxidase from bovine heart and from *Paracoccus denitrificans* as revealed by FT-IR difference spectroscopy, *FEBS Lett.* 458, 83–86.

Hellwig, P., Mogi, T., Tomson, F. L., Gennis, R. B., Iwata, J., Miyoshi, H., and Mänteles, W. (1999b) Vibrational modes of ubiquinone in cytochrome *bo*₃ from *Escherichia coli* identified by Fourier transform infrared difference spectroscopy and specific ¹³C labeling, *Biochemistry* 38, 14683–14689.

Hellwig, P., Soulimane, T., Buse, G., and Mänteles, W. (1999c) Electrochemical, FTIR, and UV/VIS spectroscopic properties of the *ba*₃ oxidase from *Thermus thermophilus*, *Biochemistry* 38, 9648–9658.

Hellwig, P., Grzybek, S., Behr, J., Ludwig, B., Michel, H., and Mäntele, W. (1999d) Electrochemical and ultraviolet/visible/infrared spectroscopic analysis of heme *a* and *a*₃ redox reactions in the cytochrome *c* oxidase from *Paracoccus denitrificans*: separation of heme *a* and *a*₃ contributions and assignment of vibrational modes, *Biochemistry* 38, 1685–1694.

Hellwig, P., Scheide, D., Bungert, S., Mäntele, W., and Friedrich, T. (2000) FT-IR spectroscopic characterization of NADH : ubiquinone oxidoreductase (complex I) from *Escherichia coli*: oxidation of FeS cluster N2 is coupled with the protonation of an aspartate or glutamate side chains, *Biochemistry* 39, 10884–10891.

Hellwig, P., Barquera, B., and Gennis, R. B. (2001) Direct evidence for the protonation of aspartate-75, proposed to be at a quinol binding site, upon reduction of cytochrome *bo*₃ from *Escherichia coli*, *Biochemistry* 40, 1077–1082.

Hellwig, P., Pfitzner, U., Behr, J., Rost, B., Pesavento, R. P., v. Donk, W., Gennis, R. B., Michel, H., Ludwig, B., and Mäntele, W. (2002) Vibrational modes of tyrosines in cytochrome *c* oxidase from *Paracoccus denitrificans*: FTIR and electrochemical studies on Tyr-D4-labeled and on Tyr280His and Tyr35Phe mutant enzymes, *Biochemistry* 41, 9116–9125.

Herres, W. and Gronholz, J. (1985) Part 1: Data acquisition and Fourier transformation, in *Understanding FT-IR data processing*, Dr. Alfred Hüthig Publishers, Heidelberg, Germany.

Herzberg, G. (1962) Infrared and Raman spectra of polyatomic molecules, in *Molecular spectra and molecular structure: II*, D. van Nostrand Company, Inc., Princeton, NJ.

Hienerwadel, R., Grzybek, S., Fogel, C., Kreutz, W., Okamura, M. Y., Paddock, M. L., Breton, J., Nabedryk, E., and Mäntele, W. (1995) Protonation of Glu L212 following Q_B⁻ formation in the photosynthetic reaction center of *Rhodobacter sphaeroides*: evidence from time-resolved infrared spectroscopy, *Biochemistry* 34, 2832–2843.

Honig, B., and Nicholls, A. (1995) Classical electrostatics in biology and chemistry, *Science* 268, 1144–1149.

Jensen, G. M., Warshel, A., and Stephens, P. J. (1994) Calculation of the redox potentials of iron-sulfur proteins: the 2-/3- couple of [Fe₄S₄*Cys₄] clusters in *Peptococcus aerogenes* ferredoxin, *Azotobacter vinelandii* ferredoxin I, and *Chromatium vinosum* high-potential iron protein, *Biochemistry* 33, 10911–10924.

Kannt, A., Lancaster, C. R. D., and Michel, H. (1998) The coupling of electron transfer and proton translocation: electrostatic calculations on *Paracoccus denitrificans* cytochrome *c* oxidase, *Biophys. J.* 74, 708–721.

Kassner, R. J. (1972) Effects of nonpolar environments on redox potentials of heme complexes, *Proc. Natl. Acad. Sci. USA* 69, 2263–2267.

Kassner, R. J. (1973) Theoretical model for effects of local nonpolar heme environments on redox potentials in cytochromes, *J. Am. Chem. Soc.* 95, 2674–2677.

Kröger, A. (1978) Fumarate as terminal acceptor of phosphorylative electron transport, *Biochim. Biophys. Acta* 505, 129–145.

Kröger, A., Biel, S., Simon, J., Groß, R., Unden, G., and Lancaster, C. R. D. (2002) Fumarate respiration of *Wolinella succinogenes*: enzymology, energetics and coupling mechanism, *Biochim. Biophys. Acta* 1553, 23–38.

Lancaster, C. R. D., Michel, H., Honig, B., and Gunner, M. R. (1996) Calculated coupling of electron and proton transfer in the photosynthetic reaction center of *Rhodospseudomonas viridis*, *Biophys. J.* 70, 1469–2492.

Lancaster, C. R. D., Kröger, A., Auer, M., and Michel, H. (1999) Structure of fumarate reductase from *Wolinella succinogenes* at 2.2 Å resolution, *Nature* 402, 377–385.

Lancaster, C. R. D., Groß, R., Haas, A., Ritter, M., Mäntele, W., Simon, J., and Kröger, A. (2000) Essential role of Glu-C66 for menaquinol oxidation indicates transmembrane electrochemical potential generation by *Wolinella succinogenes* fumarate reductase, *Proc. Natl. Acad. Sci. USA* 97, 13051–13056.

Lancaster, C. R. D. (2001) Succinate:quinone oxidoreductases, in *Handbook of Metalloproteins* (Messerschmidt, A., Huber, R., Poulos, T., and Wieghardt, K., Eds.) Vol. 1, pp 379–401, John Wiley & Sons Ltd., Chichester.

Lancaster, C. R. D., Groß, R., and Simon, J. (2001) A third crystal form of *Wolinella succinogenes* quinol:fumarate reductase reveals domain closure at the site of fumarate reduction, *Eur. J. Biochem.* 268, 1820–1827.

Lancaster, C. R. D. (2002a) Succinate:quinone oxidoreductases - an overview, *Biochim. Biophys. Acta* 1553, 1–6.

Lancaster, C. R. D. (2002b) *Wolinella succinogenes* quinol:fumarate reductase - 2.2 Å resolution crystal structure and the “E-pathway” hypothesis of coupled transmembrane proton and electron transfer, *Biochim. Biophys. Acta* 1565, 215–231.

Lancaster, C. R. D. (2003a) The structure of *Wolinella succinogenes* quinol:fumarate reductase and its relevance to the superfamily of succinate:quinone oxidoreductases, *Adv. Prot. Chem.* 63, 131–149.

Lancaster, C. R. D. (2003b) The role of electrostatics in proton-conducting membrane protein complexes, *FEBS Lett.* 545, 52–60.

Lancaster, C. R. D. (2003c) *Wolinella succinogenes* quinol:fumarate reductase and its comparison to *E. coli* succinate:quinone reductase, *FEBS Lett.* 555, 21–28.

Lancaster, C. R. D. (2003d) Crystallization of *Wolinella succinogenes* quinol:fumarate reductase, in *Membrane Protein Purification and Crystallization* (Hunte, C., Schagger, H., and von Jagow, G., Eds.) 2nd ed., pp 219–228, Academic Press, San Diego, CA, USA.

Lancaster, C. R. D. (2004) Structure and function of succinate:quinone oxidoreductases and the role of quinol:fumarate reductases in fumarate respiration, in *Respiration in Archaea and Bacteria, Vol. 1: Diversity of Prokaryotic Electron Transport Carriers* (Zannoni, D., Ed.) pp 57–85, Kluwer, Dordrecht, NL.

Lemma, E., Hägerhäll, C., Geisler, V., Brandt, U., von Jagow, G., and Kröger, A. (1991) Reactivity of the *Bacillus subtilis* succinate dehydrogenase complex with quinones, *Biochim. Biophys. Acta* 1059, 281–285.

Lemos, R. S., Gomes, C. M., LeGall, J., Xavier, A. V., and Teixeira, M., (2002a) The quinol:fumarate oxidoreductase from the sulphate reducing bacterium *Desulfovibrio gigas*: spectroscopic and redox studies, *J. Bioenerg. Biomemb.* 34, 21–30.

Lemos, R. S., Fernandes, A. S., Pereira, M. M., Gomes, C. M., and Texeira, M. (2002b) Quinol:fumarate oxidoreductases and succinate:quinone oxidoreductases: phylogenetic relationships, metal centres and membrane attachment, *Biochim. Biophys. Acta* 1553, 158–170.

Leonhard, M., and Mäntele, W. (1993) Fourier transform infrared spectroscopy and electrochemistry of the primary electron donor in *Rhodobacter sphaeroides* and *Rhodospseudomonas viridis* reaction centers: vibrational modes of the pigments in situ and evidence for protein and water modes affected by P⁺ formation, *Biochemistry* 32, 4532–4538.

Li, J., Nelson, M. R., Peng, C. Y., Bashford, D., and Noodleman, L. (1998) Incorporating protein environments in density functional theory: a self-consistent reaction field calculation of redox potentials of [2Fe2S] clusters in ferredoxin and phthalate dioxygenase reductase, *J. Phys. Chem. A* 102, 6311–6324.

Li, X.-Y., Czernuszewicz, R. S., Kincaid, J. R., Su, Y. O., and Spiro, T. G. (1990) Consistent porphyrin force field. 1. Normal-mode analysis for nickel porphine and nickel tetraphenylporphine from resonance Raman and infrared spectra and isotope shifts, *J. Phys. Chem.* *94*, 31–47.

Lill, M. A., and Helms, V. (2001) Molecular dynamics simulation of proton transport with quantum mechanically derived proton hopping rates (Q-HOP MD), *J. Chem. Phys.* *115*, 7993–8005.

Louro, R. O., Catarino, T., Salgueiro, C. A., LeGall, J., and Xavier, A. V. (1996) Redox-Bohr effect in the tetrahaem cytochrome c_3 from *Desulfovibrio vulgaris*: a model for energy transduction mechanism, *J. Biol. Inorg. Chem.* *1*, 34–38.

Lübber, M., and Gerwert, K. (1996) Redox FTIR difference spectroscopy using caged electrons reveals contributions of carboxyl groups to the catalytic mechanism of haem-copper oxidases, *FEBS Lett.* *397*, 303–307.

Lübber, M., Prutsch, A., Mamat, B., and Gerwert, K. (1999) Electron transfer induces side-chain conformational changes of glutamate-286 from cytochrome bo_3 , *Biochemistry* *38*, 2048–2056.

Mäntele, W. (1993) Reaction-induced infrared difference spectroscopy for the study of protein function and reaction mechanisms, *Trends Biochem. Sci.* *18*, 197–202.

Mäntele, W. (1996) Infrared and Fourier-transform infrared spectroscopy, in *Biophysical Techniques in Photosynthesis* (Hoff, A. J., and Ames, J., Eds.) pp 137–160, Kluwer, Dordrecht, NL.

Mao, J., Hauser, K., and Gunner, M. R. (2003) How cytochromes with different folds control heme redox potentials, *Biochemistry* *42*, 9829–9840.

Michal, G. (1999) Tetrapyrroles, in *Biochemical Pathways: An Atlas of Biochemistry and Molecular Biology* (Michal, G., Ed.) pp 68–74, John Wiley & Sons, Inc., New York, USA.

Mills, D. A., Ferguson-Miller, S. (2003) Understanding the mechanism of proton movement linked to oxygen reduction in cytochrome *c* oxidase: lessons from other proteins, *FEBS Lett.* 545, 47–51.

Mitchell, P. (1961) Coupling of phosphorylation to electron and hydrogen transfer by a chemiosmotic type of mechanism, *Nature* 191, 144–148.

Mitchell, P. (1979) Keilin's respiratory chain concept and its chemiosmotic consequences, *Science* 206, 1148–1159.

Moss, D. A., Nabedryk, E., Breton, J., and Mäntele, W. (1990) Redox-linked conformational changes in proteins detected by a combination of infrared spectroscopy and protein electrochemistry: evaluation of the technique with cytochrome *c*, *Eur. J. Biochem.* 187, 565–572.

Mouesca, J.-M., Chen, J. L., Noodleman, L., Bashford, D., and Case, D. A. (1994) Density functional/Poisson-Boltzmann calculations of redox potentials for iron-sulfur clusters, *J. Am. Chem. Soc.* 116, 11898–11914.

Nabedryk, E., Breton, J., Hienerwadel, R., Fogel, C., Mäntele, W., Paddock M. L., Okamura, M. Y. (1995) Fourier transform infrared difference spectroscopy of secondary quinone acceptor photoreduction in proton transfer mutants of *Rhodobacter sphaeroides*, *Biochemistry* 34, 14722–14732.

Nicholls, A., and Honig, B. (1991) A rapid finite difference algorithm utilizing successive over-relaxation to solve the Poisson-Boltzmann equation, *J. Comp. Chem.* 12, 435–445.

Ohnishi, T., Moser, C. C., Page, C. C., Dutton, P. L., and Yano, T. (2000) Simple redox-linked proton-transfer design: new insights from structures of quinol-fumarate reductase, *Structure* 8, R23–R32.

Page, C. C., Moser, C. C., Chen, X., and Dutton, P. L. (1999) Natural engineering principles of electron tunnelling in biological oxidation–reduction. *Nature* 402, 47–52.

Popović, D. M., and Stuchebrukhov, A. A. (2004) Electrostatic study of the proton pumping mechanism in bovine heart cytochrome *c* oxidase, *J. Am. Chem. Soc.* 126, 1858–1871.

Rabenstein, B., Ullmann, G. M., and Knapp, E.-W. (1998) Energetics of electron-transfer and protonation reactions of the quinones in the photosynthetic reaction center of *Rhodospseudomonas viridis*, *Biochemistry* 37, 2488–2495.

Rich, P. R., and Breton, J. (2001) FTIR studies of the CO and cyanide adducts of fully reduced bovine cytochrome *c* oxidase, *Biochemistry* 40, 6441–6449.

Ritter, M., Anderka, O., Ludwig, B., Mäntele, W., and Hellwig, P. (2003) Electrochemical and FTIR spectroscopic characterization of the cytochrome *bc*₁ complex from *Paracoccus denitrificans*: evidence for protonation reactions coupled to quinone binding, *Biochemistry* 42, 12391–12399.

Saraste, M. (1999) Oxidative phosphorylation at the *fin de siècle*, *Science* 283, 1488–1493.

Sauer, U. S. (2001) Gezielter Austausch von Aminosäuren im Bereich des proximalen Häms der Fumarat-Reduktase von *Wolinella succinogenes*, Diploma thesis, Johann Wolfgang Goethe-University, Frankfurt am Main, Germany.

Schlereth, D. D., and Mäntele, W. (1992) Redox-induced conformational changes in myoglobin and hemoglobin: electrochemistry and ultraviolet-visible and Fourier transform

infrared difference spectroscopy at surface-modified gold electrodes in an ultra-thin-layer spectroelectrochemical cell, *Biochemistry* 31, 7494–7502.

Simon, J., Gross, R., Ringel, M., Schmidt, E., and Kröger, A. (1998) Deletion and site-directed mutagenesis of the *Wolinella succinogenes* fumarate reductase operon, *Eur. J. Biochem.* 251, 418–426.

Sinning, I. (1989) Der Elektronenakzeptorkomplex im photosynthetischen Reaktionszentrum des Purpurbakteriums *Rhodospseudomonas viridis*, PhD thesis, University of Munich, Germany.

Sitkoff, D., Sharp, K. A., and Honig, B. (1994) Accurate calculation of hydration free energies using macroscopic solvent models, *J. Phys. Chem.* 98, 1978–1988.

Stephens, P. J., Jollie, D. R., and Warshel, A. (1996) Protein control of redox potentials of iron-sulfur proteins, *Chem. Rev.* 96, 2491–2513.

Tanford, C., and Kirkwood, J. G. (1957) Theory of protein titration curves I. General equations for impenetrable spheres, *J. Am. Chem. Soc.* 79, 5333–5339.

VanAken, T., Foxall-VanAken, S., Castleman, S., and Ferguson-Miller, S. (1986) Alkyl glycoside detergents: synthesis and applications to the study of membrane proteins, *Methods Enzymol.* 125, 27–35.

Venyaminov, S. Y., and Kalnin, N. N. (1990) Quantitative IR spectrophotometry of peptide compounds in water (H₂O) solutions. I. Spectral parameters of amino acid residue absorption bands, *Biopolymers* 30, 1243–1257.

Voet, D., Voet, J. G., and Pratt, C. W. (1999) Oxidative phosphorylation, in *Fundamentals of Biochemistry*, John Wiley & Sons, Inc., New York, USA.

Wille, G., Ritter, M., Friedemann, R., Mäntele, W., and Hübner, G. (2003) Redox-triggered FTIR difference spectra of FAD in aqueous solution and bound to flavoproteins, *Biochemistry* 42, 14814–14821.

Zhang, J., Oettmeier, W., Gennis, R. B., and Hellwig, P. (2002) FTIR spectroscopic evidence for the involvement of an acidic residue in quinone binding in cytochrome *bd* from *Escherichia coli*, *Biochemistry* 41, 4612–4617.

6 APPENDIX

6.1 Electrostatics

6.1.1 Non-uniform and uniform partial charges for QFR iron-sulfur clusters

The partial charges that were assigned to the three iron-sulfur centers and used for the MCCE calculations were extracted from (Stephens *et al.*, 1996) for the [3Fe-4S] center, from (Li *et al.*, 1998) for the [2Fe-2S] center, and from (Jensen *et al.*, 1994) for the [4Fe-4S] center:

Non-uniform partial charges on iron-sulfur clusters:

[2Fe-2S]:

| | | | | | |
|-----|-----|--------|-----|-----|--------|
| FE1 | FES | 0,693 | FE1 | FE- | 0,828 |
| FE2 | FES | 0,693 | FE2 | FE- | 0,828 |
| S1 | FES | -0,573 | S1 | FE- | -0,830 |
| S2 | FES | -0,573 | S2 | FE- | -0,830 |
| SG1 | FES | -0,560 | SG1 | FE- | -0,749 |
| SG2 | FES | -0,560 | SG2 | FE- | -0,749 |
| SG3 | FES | -0,560 | SG3 | FE- | -0,749 |
| SG4 | FES | -0,560 | SG4 | FE- | -0,749 |

[3Fe-4S]:

| | | | | | |
|-----|-----|--------|-----|-----|--------|
| FE1 | F3S | -0,057 | FE1 | F3- | -0,109 |
| FE2 | F3S | -0,057 | FE2 | F3- | -0,109 |
| FE3 | F3S | -0,057 | FE3 | F3- | -0,109 |
| S1 | F3S | -0,305 | S1 | F3- | -0,414 |
| S2 | F3S | -0,305 | S2 | F3- | -0,414 |
| S3 | F3S | -0,305 | S3 | F3- | -0,414 |
| S4 | F3S | -0,305 | S4 | F3- | -0,414 |
| SG1 | F3S | -0,203 | SG1 | F3- | -0,339 |
| SG2 | F3S | -0,203 | SG2 | F3- | -0,339 |
| SG3 | F3S | -0,203 | SG3 | F3- | -0,339 |

[4Fe-4S]:

| | | | | | |
|-----|-----|--------|-----|-----|--------|
| FE1 | FS4 | 0,411 | FE1 | FS- | 0,488 |
| FE2 | FS4 | 0,411 | FE2 | FS- | 0,488 |
| FE3 | FS4 | 0,411 | FE3 | FS- | 0,488 |
| FE4 | FS4 | 0,411 | FE4 | FS- | 0,488 |
| S1 | FS4 | -0,395 | S1 | FS- | -0,539 |
| S2 | FS4 | -0,395 | S2 | FS- | -0,539 |
| S3 | FS4 | -0,395 | S3 | FS- | -0,539 |
| S4 | FS4 | -0,395 | S4 | FS- | -0,539 |
| SG1 | FS4 | -0,516 | SG1 | FS- | -0,699 |
| SG2 | FS4 | -0,516 | SG2 | FS- | -0,699 |
| SG3 | FS4 | -0,516 | SG3 | FS- | -0,699 |
| SG4 | FS4 | -0,516 | SG4 | FS- | -0,699 |

Uniform partial charges on iron-sulfur clusters:**[2Fe-2S]:**

| | | | | | |
|-----|-----|--------|-----|-----|--------|
| FE1 | FES | -0.250 | FE1 | FE- | -0.375 |
| FE2 | FES | -0.250 | FE2 | FE- | -0.375 |
| S1 | FES | -0.250 | S1 | FE- | -0.375 |
| S2 | FES | -0.250 | S2 | FE- | -0.375 |
| SG1 | FES | -0.250 | SG1 | FE- | -0.375 |
| SG2 | FES | -0.250 | SG2 | FE- | -0.375 |
| SG3 | FES | -0.250 | SG3 | FE- | -0.375 |
| SG4 | FES | -0.250 | SG4 | FE- | -0.375 |

[3Fe-4S]:

| | | | | | |
|-----|-----|--------|-----|-----|--------|
| FE1 | F3S | -0.200 | FE1 | F3- | -0.300 |
| FE2 | F3S | -0.200 | FE2 | F3- | -0.300 |
| FE3 | F3S | -0.200 | FE3 | F3- | -0.300 |
| S1 | F3S | -0.200 | S1 | F3- | -0.300 |
| S2 | F3S | -0.200 | S2 | F3- | -0.300 |
| S3 | F3S | -0.200 | S3 | F3- | -0.300 |
| S4 | F3S | -0.200 | S4 | F3- | -0.300 |
| SG1 | F3S | -0.200 | SG1 | F3- | -0.300 |
| SG2 | F3S | -0.200 | SG2 | F3- | -0.300 |
| SG3 | F3S | -0.200 | SG3 | F3- | -0.300 |

[4Fe-4S]:

| | | | | | |
|-----|-----|--------|-----|-----|--------|
| FE1 | FS4 | -0.167 | FE1 | FS- | -0.250 |
| FE2 | FS4 | -0.167 | FE2 | FS- | -0.250 |
| FE3 | FS4 | -0.167 | FE3 | FS- | -0.250 |
| FE4 | FS4 | -0.167 | FE4 | FS- | -0.250 |
| S1 | FS4 | -0.167 | S1 | FS- | -0.250 |
| S2 | FS4 | -0.167 | S2 | FS- | -0.250 |
| S3 | FS4 | -0.167 | S3 | FS- | -0.250 |
| S4 | FS4 | -0.167 | S4 | FS- | -0.250 |
| SG1 | FS4 | -0.167 | SG1 | FS- | -0.250 |
| SG2 | FS4 | -0.167 | SG2 | FS- | -0.250 |
| SG3 | FS4 | -0.167 | SG3 | FS- | -0.250 |
| SG4 | FS4 | -0.167 | SG4 | FS- | -0.250 |

6.1.2 Influence of FeS-cluster redox state on simulated heme redox titrations

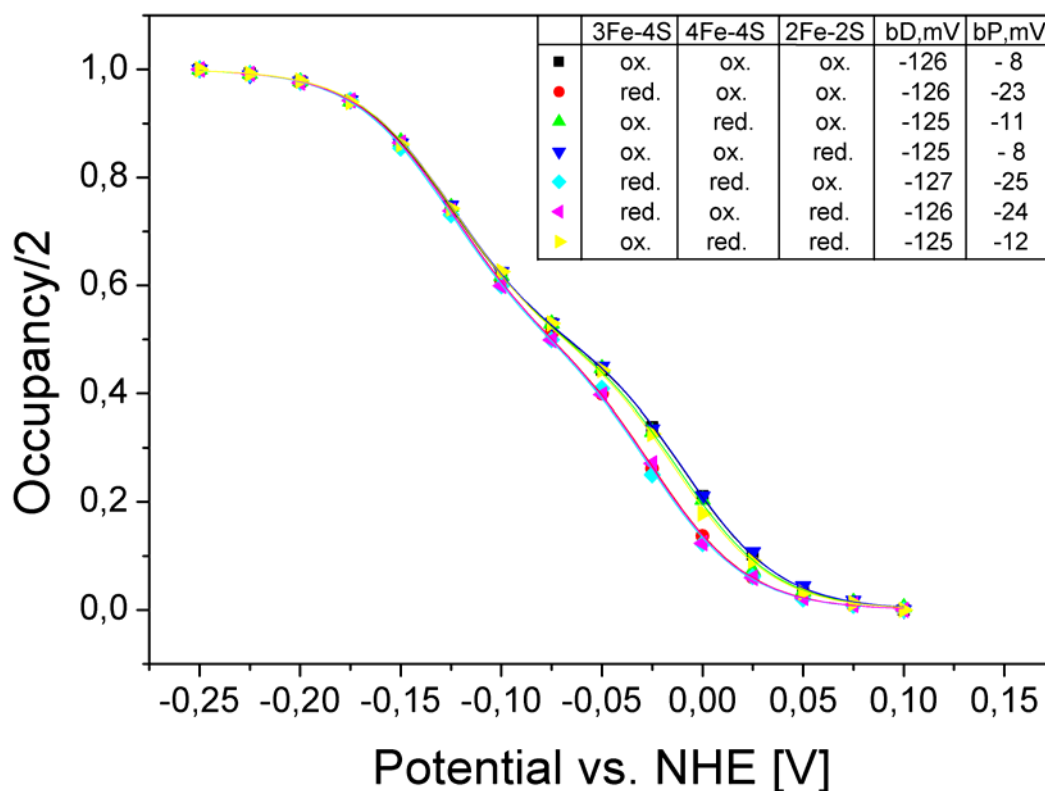


Figure 6.1: Simulated heme b_D and b_P redox titrations of QFR with 1 or 2 electrons on the system of FeS clusters.

The redox state of the FeS clusters was set as it is indicated in the table in the figure. The *solid lines* represent the corresponding Nernst fitting-curves, and the respective midpoint potentials of the heme groups (model W, pH 7) are given in [mV]. The influence of the different FeS redox states on the distal heme b_D is negligible. The redox state of the [3Fe-4S] cluster modulates the midpoint potential of the proximal heme b_P by approximately 15 mV.

6.1.3 Results of simulated heme reduction in QFR based on model X

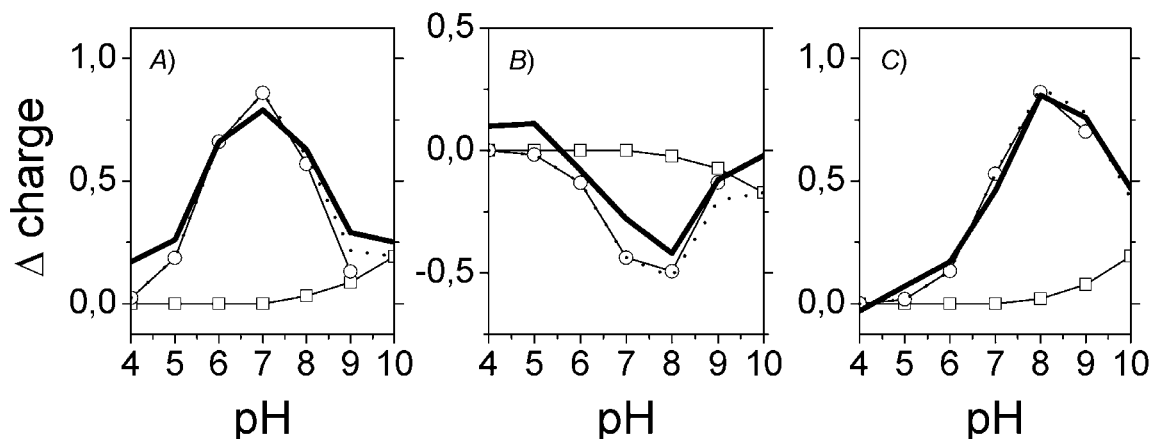


Figure 6.2: Analogous to Figure 3.4, but based on model X (no water molecules).

A—C Comparison of the change of the total charge of model X (*bold solid line*) as a function of pH for the three considered electron transfer steps with the summed contribution of two individual residues (*bold dotted line*), which are in detail: Glu⁻ C66 (*open squares*), and Glu⁻ C180 (*open circles*). The data show the sum of the occupancies of the respective deprotonated, charged species. The change of charge in panel (A) is calculated as the difference of the total charge in state $b_D^{red} b_P^{ox}$ minus $b_D^{ox} b_P^{ox}$, in (B) $b_D^{ox} b_P^{red}$ minus $b_D^{red} b_P^{ox}$, and in (C) $b_D^{red} b_P^{red}$ minus $b_D^{ox} b_P^{red}$.

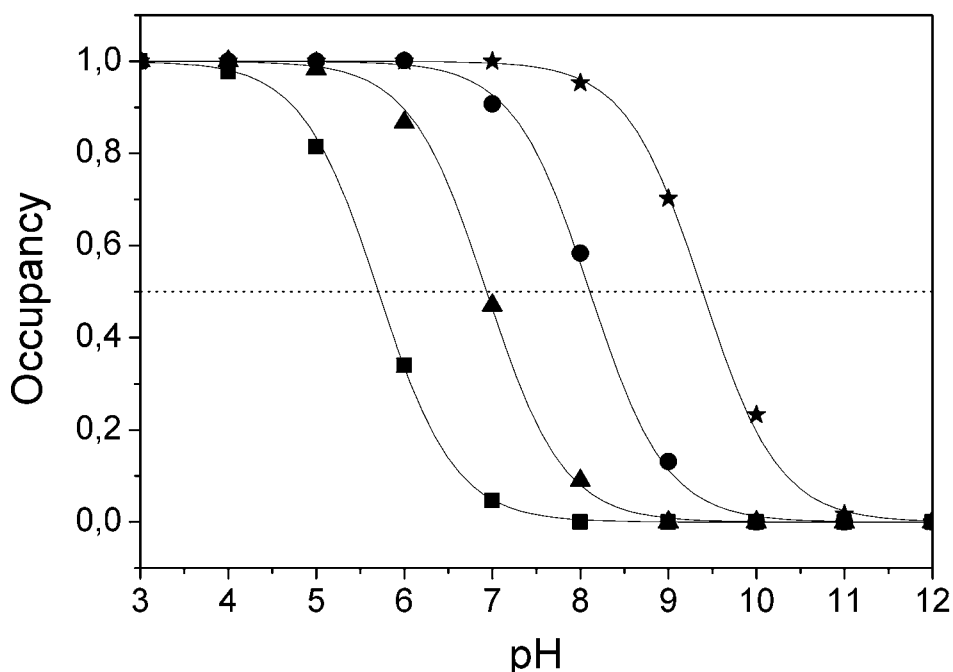


Figure 6.3: Analogous to Figure 3.5, but based on model X (no water molecules).

The pH titration curves of Glu⁰ C180 (sum of all neutral conformers) are shown as a function of the four considered heme redox states. The *solid lines* represent fitting curves according to a simple Henderson-Hasselbalch equation. The corresponding pK_a values are 5.7 in the oxidized state $b_D^{ox} b_P^{ox}$ (*squares*), 8.1 for $b_D^{red} b_P^{ox}$ (distal heme reduced, *circles*), 6.9 for $b_D^{ox} b_P^{red}$ (proximal heme reduced, *triangles*), and 9.4 for $b_D^{red} b_P^{red}$ (both hemes reduced, *stars*).

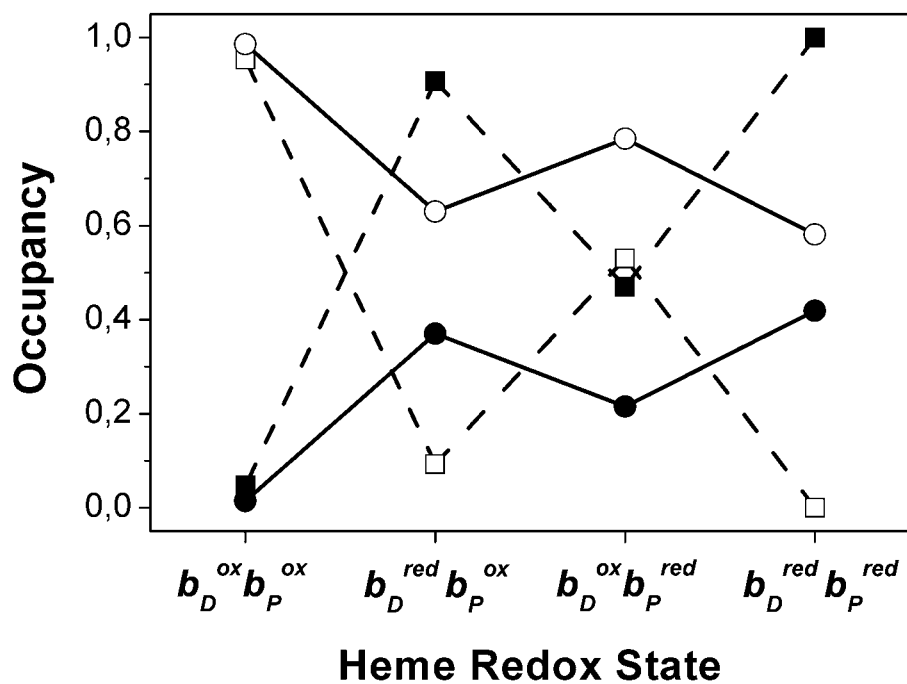
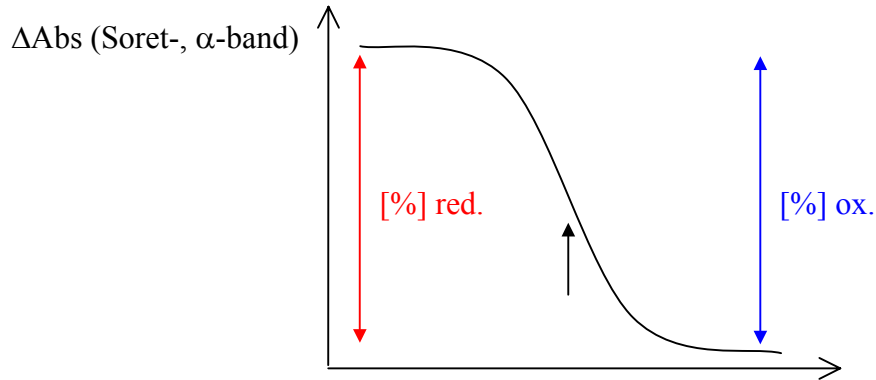


Figure 6.4: Analogous to Figure 3.7, but based on model X (no water molecules).

Summed occupancies of all conformers in the conformation “intermediate” (*full circles*) and “distal” (*open circles*), and summed occupancies of all protonated (*full squares*) and deprotonated (*open squares*) conformers at pH 7 as a function of the heme *b* redox state. This figure also illustrates that the “distal” conformation (*open circles*) is always preferred over the “intermediate” conformation (*full circles*) in all modeled heme redox states.

6.2 Spectroscopy

6.2.1 Data fitting of (VIS) heme redox titrations with the Nernst equation



[%] red. = $\Delta\text{Abs}(E_h) = [\text{red}] =$ occupancy of reduced heme state

[%] ox. = $\Delta\text{Abs}_{\text{max}} - \Delta\text{Abs}(E_h) = [\text{ox}] =$ occupancy of oxidized heme state

Nernst equation:

$$E_h = E_m + \frac{RT}{nF} \ln \frac{[\text{ox}]}{[\text{red}]} \quad \rightarrow \quad \ln \frac{[\text{ox}]}{[\text{red}]} = \frac{nF}{RT} (E_h - E_m); \text{ insertion for } [\text{red}] \text{ and } [\text{ox}] \text{ yields:}$$

$$\ln \left(\frac{\Delta\text{Abs}_{\text{max}} - \Delta\text{Abs}(E_h)}{\Delta\text{Abs}(E_h)} \right) = \frac{nF}{RT} (E_h - E_m) \quad \rightarrow$$

$$\frac{\Delta\text{Abs}_{\text{max}} - \Delta\text{Abs}(E_h)}{\Delta\text{Abs}(E_h)} = \exp \left(\frac{nF}{RT} (E_h - E_m) \right) \quad \rightarrow$$

$$\frac{\Delta\text{Abs}_{\text{max}}}{\Delta\text{Abs}(E_h)} - 1 = \exp \left(\frac{nF}{RT} (E_h - E_m) \right) \quad \rightarrow \quad \Delta\text{Abs}(E_h) = \frac{\Delta\text{Abs}_{\text{max}}}{1 + e^{\frac{nF}{RT} (E_h - E_m)}}$$

„two-step“:
$$\Delta\text{Abs}_{\text{total}}(E_h) = \frac{\Delta\text{Abs}_{\text{max,Low}}}{1 + e^{\frac{nF(E_h - E_{m,Low})}{RT}}} + \frac{\Delta\text{Abs}_{\text{max,High}}}{1 + e^{\frac{nF(E_h - E_{m,High})}{RT}}}$$

With:

n = number of (transferred) electrons

R = universal gas constant ($8.3145 \text{ J}\cdot\text{K}^{-1}\cdot\text{Mol}^{-1}$)

F = Faraday constant ($96,485.3415 \text{ C}\cdot\text{Mol}^{-1}$)

T = absolute temperature (K)

6.2.2 Preparation and calibration of the Ag/AgCl reference electrode

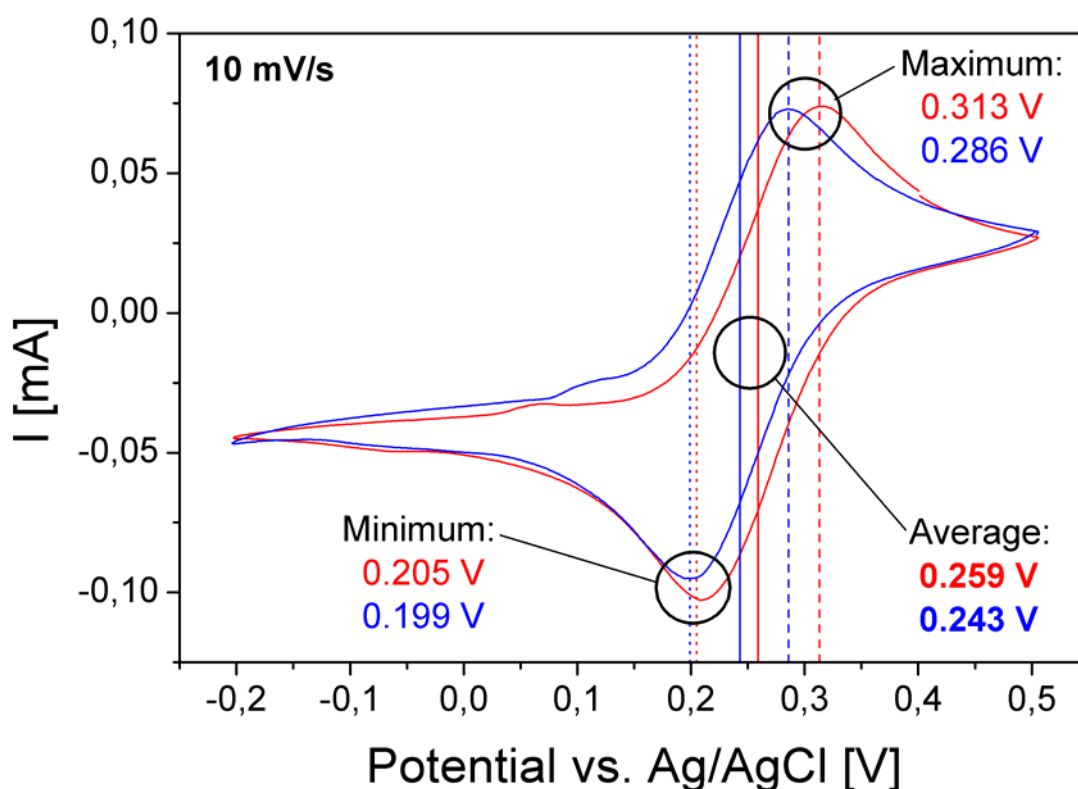


Figure 6.5: Calibration and preparation of the Ag/AgCl reference electrode.

The graph shows single cyclic voltammograms of the Ag/AgCl reference electrode in potassium ferrocyanide ($\text{K}_4[\text{Fe}(\text{CN})_6]$) solution (dissolved in 100 mM KP_i -buffer, pH 7, with 100 mM KCl). The maximum and minimum currents are indicated in the graph. The reference “midpoint” (average) potential values are indicated in bold numbers. *Red color* represents data measured with the Ag/AgCl reference electrode and an older chlorination. Data in *blue* was measured after mechanically removing the AgCl layer with abrasive paper and subsequent fresh chlorination of the electrode. The expected reference value for the average of minimum and maximum current was 250 mV. The vertical lines indicate the positions of the observed minimum (*dotted*), maximum (*dashed*), and average (*solid*) potential values. The sweep speed of the applied potential was 10 mV/s, as indicated in the figure. The chlorination of the electrode was performed in 1 M HCl containing KCl as electrolyte by applying a voltage of 1.3 V to the electrode for 5 minutes. The voltammogram was measured with the same setup used for the electrochemically induced VIS and FTIR difference spectroscopy.

6.2.3 KP_i -buffer spectra

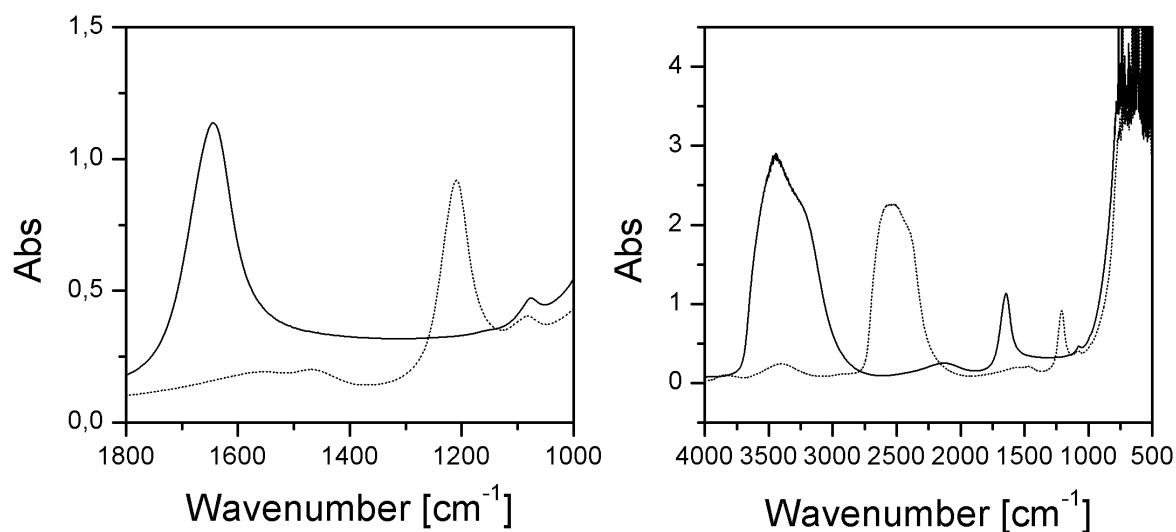


Figure 6.6: IR absorbance spectra of KP_i -buffer in H_2O and D_2O .

The figure shows the IR absorbance of 100 mM KP_i -buffer, with 100 mM KCl and 1 mM LM in H_2O at pH 7 (*solid line*) and in D_2O at pD 7.4 (*dotted line*). Both panels show the same data. The optical path was 20 μm . The figure on the left points out the regions of increased noise level due to the intense solvent absorbance (around 1650 cm^{-1} for H_2O and 1210 cm^{-1} for D_2O , respectively), which is experienced in FTIR difference spectroscopy in the mid-IR range.

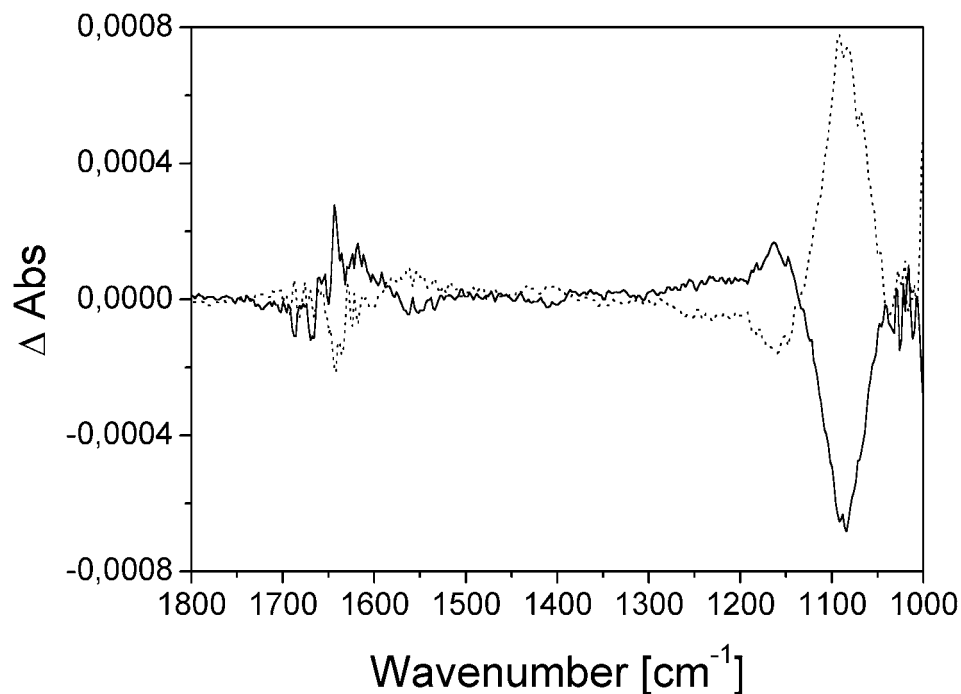


Figure 6.7: Electrochemically induced FTIR difference spectra of KP_i -buffer and mediators at pH 7.

The graph shows FTIR difference spectra of 100 mM KP_i -buffer (with 100 mM KCl and 1 mM LM) and mediators at pH 7. Thirteen difference spectra were averaged. The two reference potentials were -0.37 V and $+0.21$ V (*solid line*: “oxidized-minus-reduced”, *dotted line*: “reduced-minus-oxidized”). Below 1200 cm^{-1} , the strong PO modes are observed. The figure also reflects the higher noise level in the region around 1650 cm^{-1} , where the strong IR water absorbance occurs.

6.2.4 QFR WT IR absorbance spectra

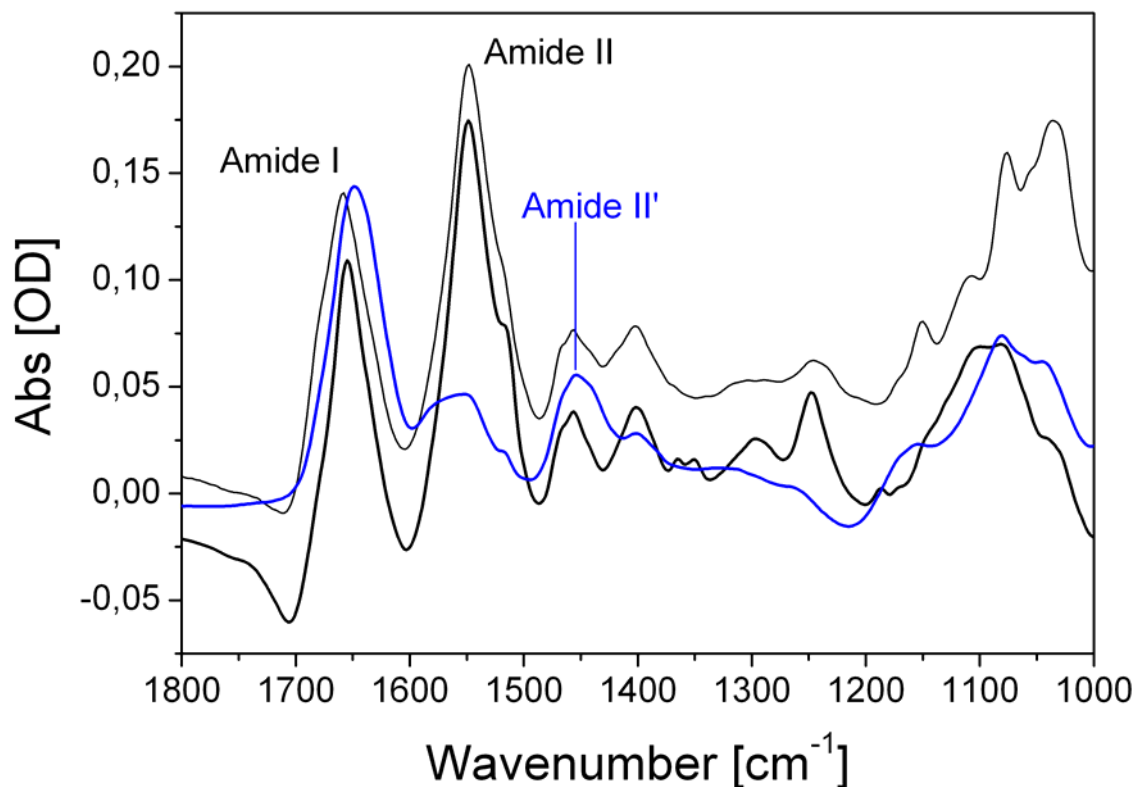


Figure 6.8: IR absorbance spectra of QFR WT in H₂O and D₂O.

The figure shows IR absorbance spectra of QFR WT in H₂O (*black lines*) and D₂O (*blue line*) KP_i-buffers at pH 7 and pD 7.4. The *thin black line* represents data measured in the electrochemical cell on a Bruker IFS 25 IR-spectrophotometer, whereas the data plotted in *bold lines* were measured with an optical path length of 7.4 μm on a Bruker IFS 66 IR-spectrophotometer. The spectra are scaled for comparison and were obtained by subtracting the respective buffer spectra (the procedure was not optimized to obtain absorbance spectra of high quality, yet it was sufficient to determine the positions of the amide I and II bands). The positions of the amide I, and amide II bands are indicated in the figure (also for the tentative amide II' band in D₂O). A small shoulder, which has been assigned to a Tyr mode (see results section), is visible in all three spectra at approximately 1515 cm⁻¹.

6.2.5 Hydrogen/deuterium isotope exchange bands in the IR spectrum

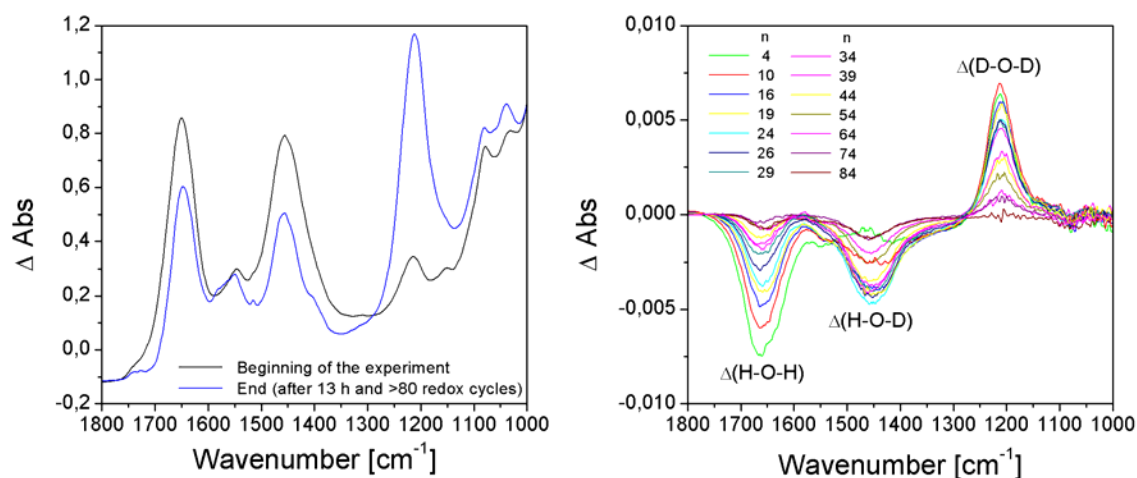


Figure 6.9: Characteristic $^1\text{H}/^2\text{H}$ isotope exchange bands in QFR WT FTIR difference spectra.

The panel on the left shows difference spectra between the empty sample compartment of the Bruker IFS 25 spectrophotometer (without the electrochemical cell) and the compartment with the electrochemical cell (loaded with the QFR sample in D_2O buffer at pD 7.4 and 5°C) for the beginning of the experiment, right after insertion and at the end of the experiment, right before removal of the cell (after 13 hours and more than 80 measured redox cycles). The right panel shows the corresponding $^1\text{H}/^2\text{H}$ exchange bands which were obtained by adding the FTIR difference spectra for the back and forth direction of the induced redox reaction (“n” is the number of performed cycles). Thus, the exchange bands represent the evolution of the baseline with respect to time. In the end (after more than 80 cycles), the baseline is nearly stable and no further $^1\text{H}/^2\text{H}$ exchange occurs in the cell and the protein. In some cases, the residual water absorbance around 1650 cm^{-1} in D_2O was considerably smaller at the end of the experiment than in the experiment shown in the figure. In addition, the better the extent of $^1\text{H}/^2\text{H}$ isotope exchange is prior to the FTIR experiment, the smaller are the characteristic $^1\text{H}/^2\text{H}$ exchange bands in the baseline. The respective pure and mixed vibrational modes of H_2O and D_2O (as identified and assigned in ref. Hellwig, 1998) are indicated in the right panel; and the label “ Δ ” on the bending modes reflects the increasing and decreasing nature of the observed $^1\text{H}/^2\text{H}$ exchange bands.

6.2.6 Electrochemically induced FTIR difference spectra of QFR enzyme variants E180Q and E66Q in D₂O buffer

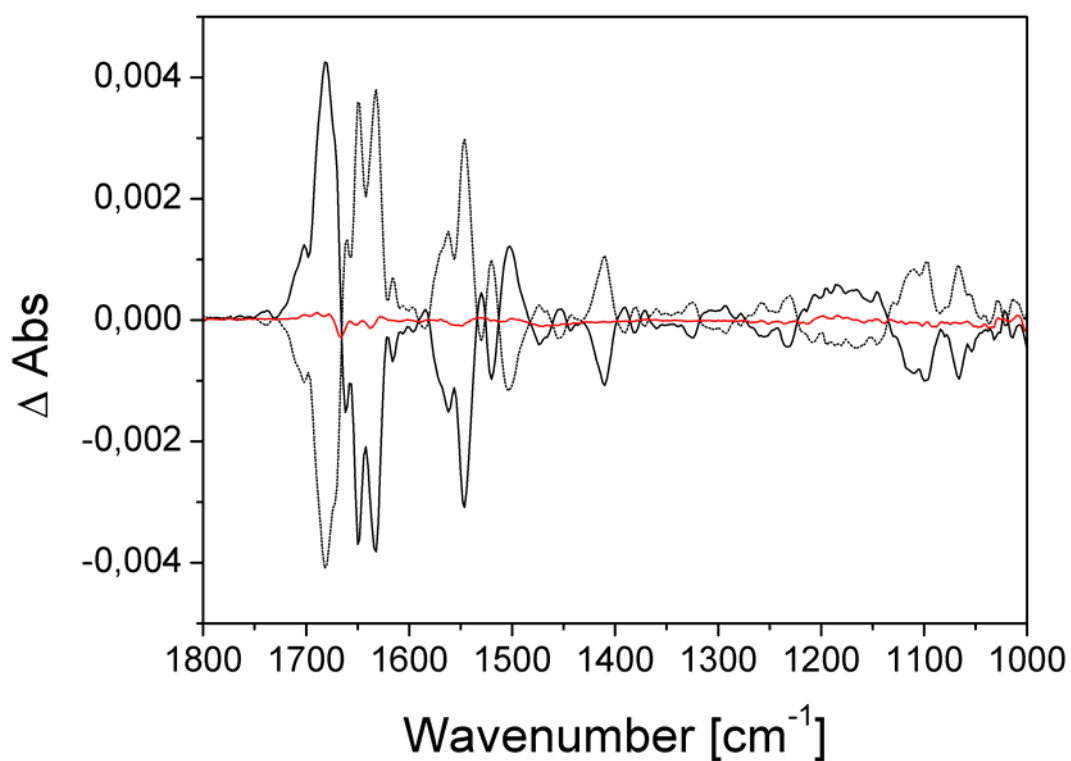


Figure 6.10: Electrochemically induced FTIR difference spectra of QFR E180Q in D₂O at pD 7.4.

The reference potentials and labeling of the data are the same as for the QFR WT data presented in Figure 3.9. Six pairs of difference spectra (128 scans each) were averaged. The *red line* is the sum of the two difference spectra and shows the baseline stability. No ¹H/²H exchange bands had to be subtracted.

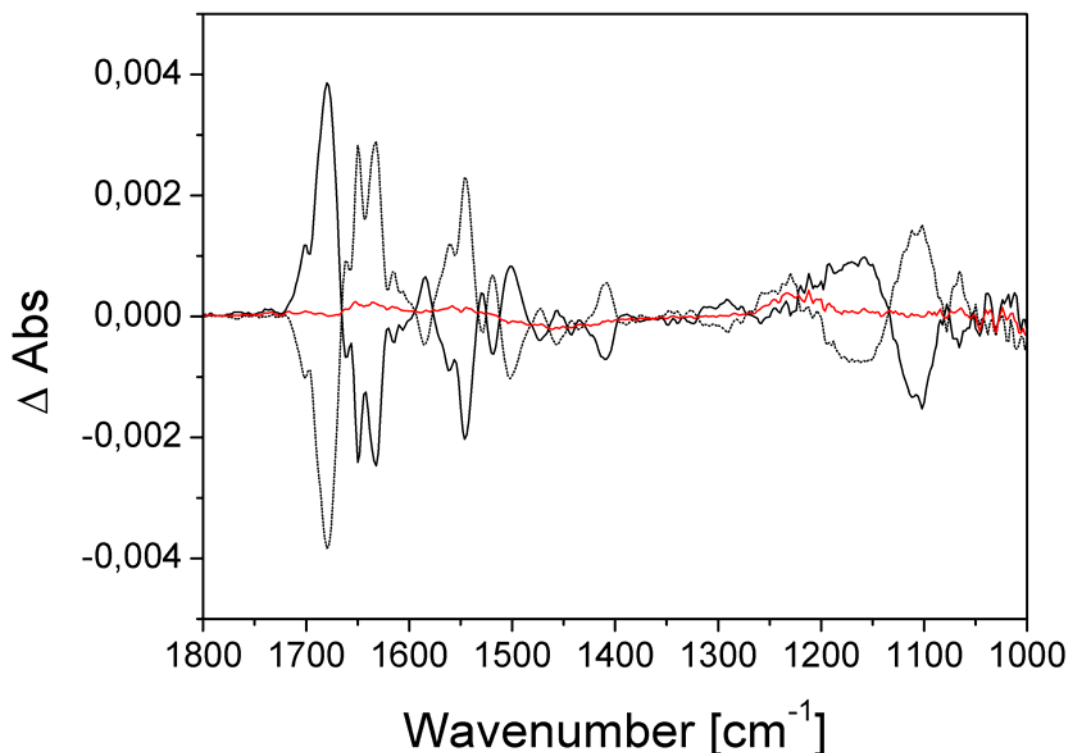


Figure 6.11: Electrochemically induced FTIR difference spectra of QFR E66Q in D₂O at pD 7.4.

The reference potentials and labeling of the data are the same as for the QFR WT data presented in Figure 3.9. Two pairs of difference spectra (128 scans each) were averaged. The *red line* is the sum of the two difference spectra and shows the baseline stability. No data in D₂O were collected for QFR enzyme variant E270Q. No ¹H/²H exchange bands were subtracted.

6.2.7 Baseline instabilities during FTIR data acquisition

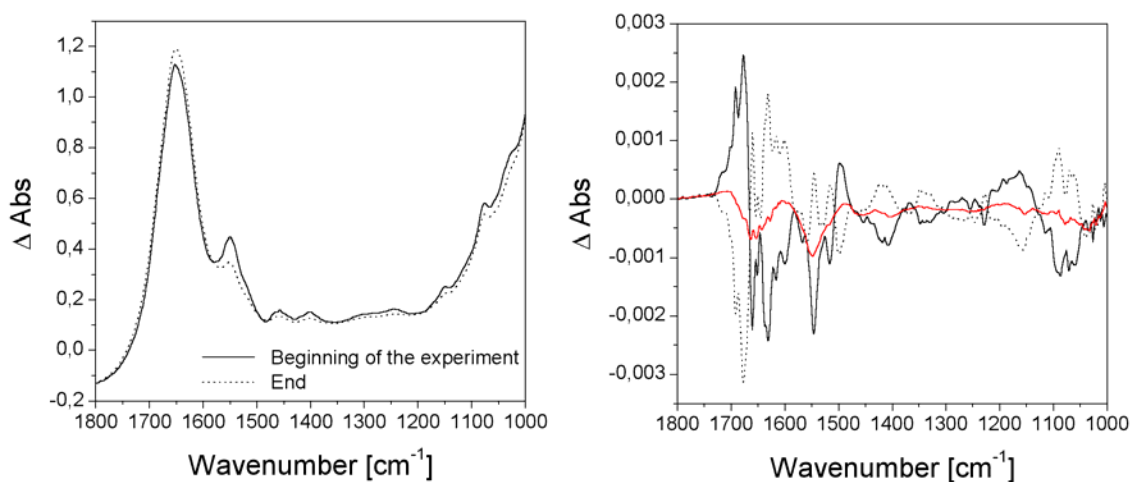


Figure 6.12: Baseline instabilities and technical difficulties in FTIR difference spectroscopy.

The panel on the left shows difference spectra between the empty sample compartment of the Bruker IFS 25 spectrophotometer (without the electrochemical cell) and the compartment with the electrochemical cell (loaded with the QFR sample in H₂O buffer) for the beginning of the experiment, right after insertion; and at the end of

the experiment, right before removal of the cell. The spectra show that the thickness of the water layer had slightly increased (H_2O band at 1648 cm^{-1}) in the course of the experimental session whereas the protein concentration had decreased (cf. amide II band 1550 cm^{-1}). Since this was a continuous effect, the changes are reflected in an unstable baseline (*red line*) in the corresponding averaged FTIR difference bands (“reduced-minus-oxidized” and vice versa, labeling of spectra and reference potentials as indicated earlier), which are shown in the right panel. The negative dip in the (*red*) baseline is a net change of water and amide I absorbance. If the decrease of protein concentration in the IR beam is very high, the baseline is of the shape of a negative protein absorbance spectrum. The “swelling” of the water layer with subsequent decrease of protein concentration in the area of the IR beam can occur if the system, which consists of the cell plus the tightening screws of the holder and the rubber O-rings that seal the cell, is not stable. If the volume between the two CaF_2 windows increases, buffer from the surrounding reservoir enters and dilutes the protein solution. A critical phase is the insertion of the cell, which is accompanied by a temperature change from room temperature down to 5° C (temperature of the cooling liquid). Thus, it is advisable to adjust the final tightness of the four screws of the cell holder (and hence the final thickness of the water layer between the CaF_2 windows) only after the cell is in thermal equilibrium with the cooling liquid and the sample compartment. Such baseline drifts as shown in the figure can be corrected by subtracting the respective baseline, but the goal should be to obtain a stable baseline and avoid mathematical corrections of the data. Similar negative effects can also occur if the cell is not properly sealed and leaking, or if the protein is degrading. The discussed problems can also affect the results of VIS difference spectra.

6.2.8 Disturbing effect of water vapor in the sample compartment on FTIR spectra

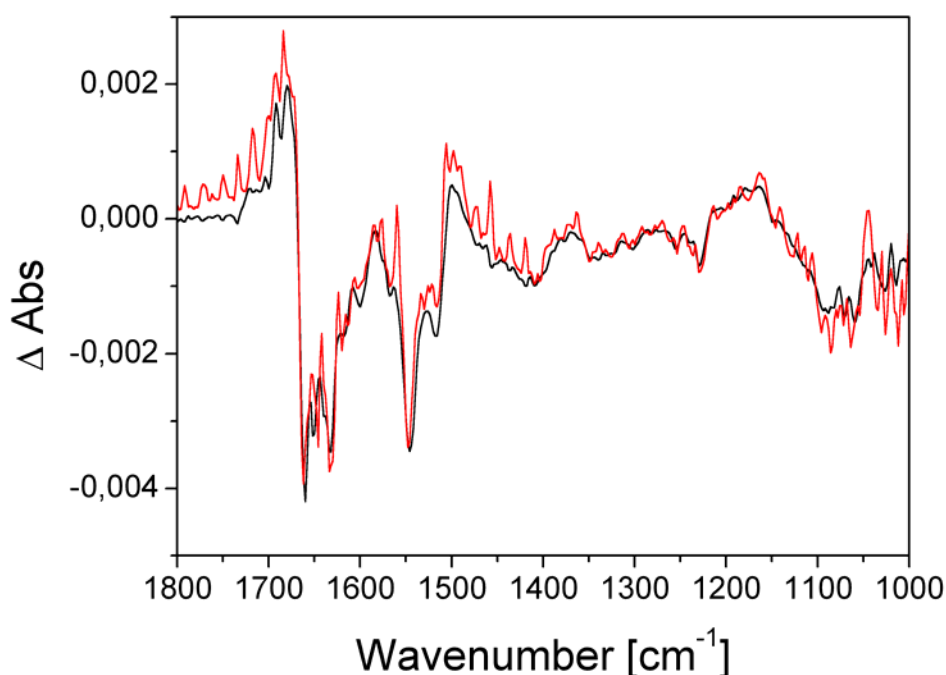


Figure 6.13: The disturbing effect of water vapor in the sample compartment of the FTIR spectrophotometer.

The *black* spectrum shows the average of 11 QFR difference spectra, the *red curve* is an individual difference spectrum, which is strongly obscured by intense sharp absorbance bands due to water vapor. As can be seen in the figure, the effect is smoothed in the averaged spectrum; but it is generally not advisable to rely on such averaged data since spectral artifacts cannot be ruled out and could easily be mistaken for relevant signals. This problem can occur despite the fact that the sample compartment is purged with dry air, especially during hot periods in summertime, which are accompanied by high humidity.

6.2.9 Heme redox titrations of QFR WT with ^{13}C -labeled heme propionates

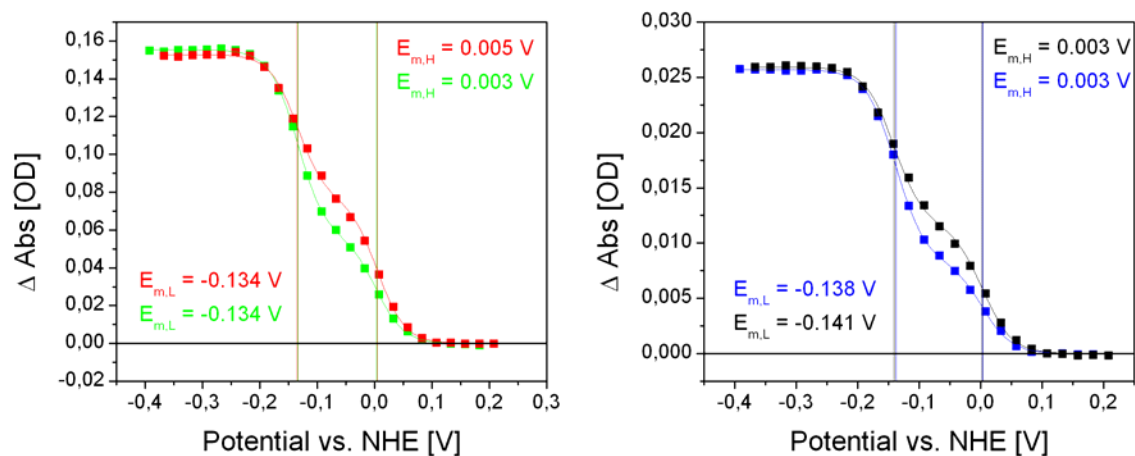


Figure 6.14: Heme redox titration curves of QFR WT enzyme with ^{13}C -labeled heme propionates at pH 7.

The left panel shows the redox dependence of the (Soret) difference band monitored at 427 nm (reductive titration in *green*, oxidative in *red*). The right panel shows the redox dependence of the (a) difference band monitored at 560 nm (reductive titration in *blue*, oxidative in *black*). In the same color-coding, the corresponding Nernst fitting curves are shown in addition to the position of the midpoint potential values (*colored vertical lines*). The absorbance differences in the range between the two midpoints might be due to insufficient equilibration times for the potential steps in this particular range; yet this did not seem to affect the results since the values obtained for both directions are very similar.

6.2.10 Identification of a spectral artifact at 1292 cm⁻¹ due to the mediators

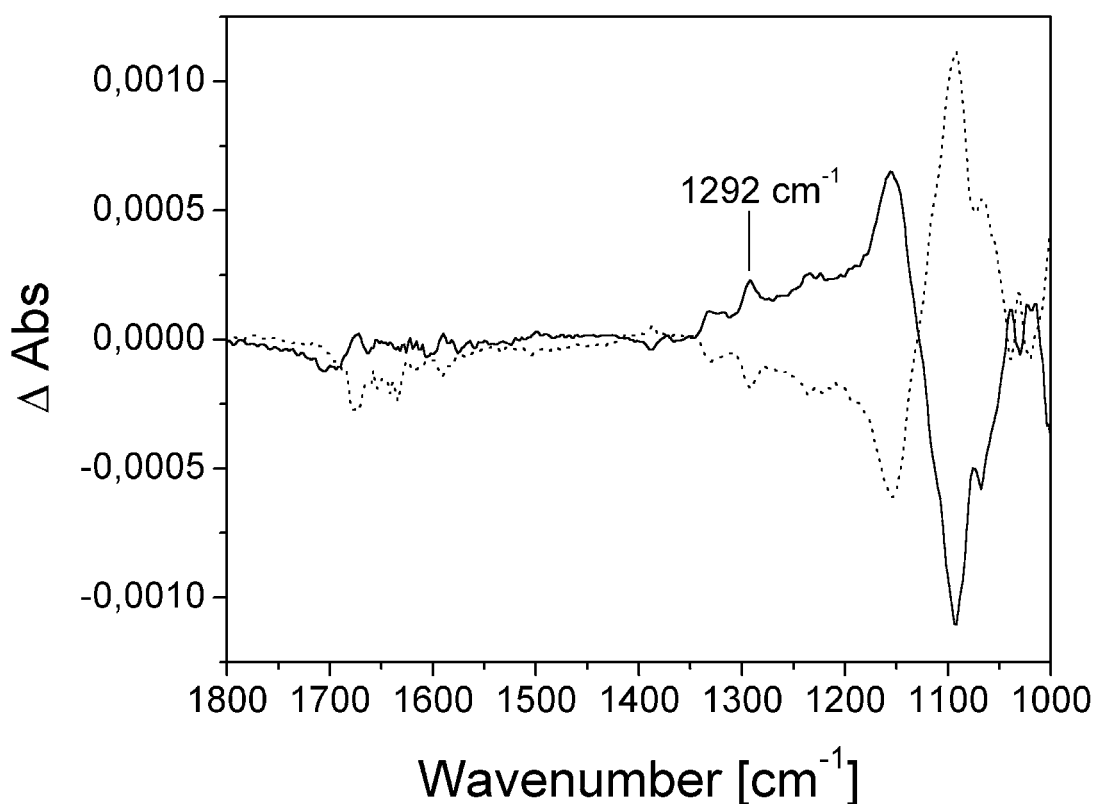


Figure 6.15: Identification of a mediator-related difference signal at 1292 cm⁻¹.

The figure shows electrochemically induced FTIR difference spectra of 100 mM KP_i-buffer (with 100 mM KCl and 1 mM LM) and mediators at pH 7. A total of 34 difference spectra were averaged. The two reference potentials were -0.37 V and +0.21 V (*solid line*: “oxidized-minus-reduced”, *dotted line*: “reduced-minus-oxidized”). Comparison with earlier analogous experiments on the buffer-mediator mixture (see Fig. 6.7) clearly reveals the contribution of too highly concentrated mediators at 1292 cm⁻¹, which was found at the same position in the “full potential step” FTIR difference spectra of the QFR WT with ¹³C-labeled heme propionates (see Figures 3.14, 3.15, and 3.17).

GLOSSARY, INTERCONVERSION OF ENERGY UNITS, AND ABBREVIATIONS

Glossary:

- E_h : electrostatic potential
- E_m : oxidation-reduction (midpoint) potential
- $\Delta G(n)$: free energy of protein microstate n
- $\text{pK}_{\text{sol}}(i)$: pK_a of ionizable group i in aqueous solution
- $\Delta\Delta G_{\text{rxn}}(i)$: reaction field energy (desolvation penalty) of residue i
- $\Delta G_{\text{pol}}(i)$: interaction energy of residue i with polypeptide backbone and polar side chains
- $\Delta G_{\text{nonel}}(i)$: non-electrostatic (Lennard-Jones) interaction of residue i with the backbone and side chains with no conformational degrees of freedom
- $\Delta G_{\text{crg}}(i,j)$: pairwise electrostatic interaction energy of residues i and j
- $\Delta G_{\text{nonel}}(i,j)$: pairwise non-electrostatic (L.-J.) interaction of residues i and j
- pK_{int} : $\text{pK}_{\text{int}} = \text{pK}_{\text{sol}} - c_\alpha(\Delta\text{pK}_{\text{desolv}} + \Delta\text{pK}_{\text{pol}})$; the pK_a of an ionizable group in the protein with all other groups in the neutral state, with $c_\alpha = 1$ for bases and $c_\alpha = -1$ for acids

Interconversion of energy units:

- 1 kcal/mol = 4.184 kJ/mol
- 1 ΔpK unit = 1.38 kcal/mol
- 1 kT = 0.59 kcal/mol = 0.43 ΔpK units
- 1 eV = 23.06 kcal/mol = 16.71 ΔpK units

Abbreviations:

ADP: adenosine diphosphate; Arg⁺: ionized arginine; Arg⁰: neutral arginine; ATP: adenosine triphosphate; cmc: critical micelle concentration; EC: enzyme classification; ET: electron transfer; FAD: flavin adenine dinucleotide; FMN: flavin mononucleotide; FTIR: Fourier transform infrared; Fum: fumarate; Glu⁻: ionized glutamate; Glu⁰: neutral glutamate; ¹H/²H: hydrogen/deuterium; IR: infrared; KP₁-buffer: potassium phosphate buffer; LM: lauryl maltoside (*n*-dodecyl-β-D-maltoside); MCCE: multiconformation continuum electrostatics; MK: menaquinone; MKH₂: menaquinol; NADH: (reduced) nicotinamide adenine dinucleotide; OD: optical density; Paa: ring D heme propionate; PBE: Poisson-Boltzmann equation; Pdd: ring C heme propionate; PT: proton transfer; QFR: quinol:fumarate reductase; RC: reaction centre; SHE⁷: standard hydrogen electrode at pH 7; SQR: succinate:quinone reductase; SQOR: succinate:quinone oxidoreductase; UV: ultraviolet; VIS: visible; WT: wild-type.

DANKSAGUNG

Die vorliegende Arbeit wurde unter der Leitung von Herrn PD Dr. C. Roy D. Lancaster (Max-Planck-Institut für Biophysik, Frankfurt) in Zusammenarbeit mit Herrn Prof. Dr. Werner Mäntele (Institut für Biophysik, Johann Wolfgang Goethe-Universität, Frankfurt) am MPI für Biophysik erstellt.

Ich danke Herrn Dr. Lancaster und Herrn Prof. Dr. Hartmut Michel (MPI für Biophysik) für die Aufnahme an das Institut.

Herrn Dr. Lancaster danke ich sehr herzlich für die Überlassung dieses sehr gut vorbereiteten Projekts und für die exzellenten Arbeitsbedingungen, sowie für seine kontinuierliche und geduldige Unterstützung und Diskussionsbereitschaft, und für die vielen kritischen aber immer konstruktiven Anmerkungen und Verbesserungsvorschläge bezüglich der Manuskripte für Veröffentlichungen und dieser Dissertation.

Herrn Prof. Mäntele danke ich für die Betreuung der von mir durchgeführten spektroskopischen Experimente und für die Vertretung der Arbeit gegenüber dem Fachbereich Physik der Johann Wolfgang Goethe-Universität. Außerdem danke ich ihm für zahlreiche Diskussionen und Anregungen bezüglich der Infrarotspektroskopie sowie für die kritische Durchsicht der Manuskripte.

Ich danke Frau Dr. Michaela Ritter (Inst. für Biophysik, JWG-Universität) für die Einweisung in die FTIR-Technik und ihre Hilfe in der Anfangsphase des Projekts. Weiterhin danke ich Frau PD Dr. Petra Hellwig (Inst. für Biophysik, JWG-Universität) für ihre Empfehlung bezüglich der Wahl der Oberflächenmodifikation der Goldelektrode der elektrochemischen Zelle und für viele andere hilfreiche Kommentare.

Herrn Mauro Mileni (MPI für Biophysik) danke ich für die Herstellung der Fumarat Reduktase mit ^{13}C -markierten Hämpropionaten und für die Bestimmung des Menachinongehaltes einiger der verwendeten Proben.

Frau Elena Herzog (MPI für Biophysik) danke ich für die Überlassung einiger „Perl“-Skripte für die Prozessierung der Daten der elektrostatischen Rechnungen.

Ich danke Frau Annette Roth (MPI), Frau Monica Säger (JWG-Uni), Herrn Oliver Schürmann (JWG-Uni), Frau Christine Ernd (JWG-Uni), und Frau Nicole Hilgerdorff (MPI) für ihre technische Assistenz.

Frau Barbara Schiller und Herrn Dr. Lutz Kampmann danke ich für ihren fortwährenden Einsatz im Hinblick auf funktionierende Rechner- und Netzwerkressourcen am MPI für Biophysik.

Ich danke allen meinen Kollegen der „Gruppe Lancaster“ sowie meinen Zimmergenossinnen Elena Olkhova und Elena Herzog (ich habe trotz all der Jahre nicht Russisch gelernt) und dem gesamten Institut für die gute Atmosphäre und für viele kleinere Diskussionen und Ratschläge.

Meinen Eltern danke ich dafür, daß sie mir mein Studium ermöglicht haben. Insbesondere möchte ich meiner Mutter für ihre Geduld und ihre langjährige Unterstützung danken.

Ich danke auch ganz herzlich meiner Freundin Anna für viele biochemische Nachhilfestunden und ihre tatkräftige Hilfe beim Editieren der endgültigen Fassung dieser Dissertation.

Diese Arbeit wurde finanziell unterstützt von der Deutschen Forschungsgemeinschaft (SFB 472, Teilprojekt P19) und der Max-Planck-Gesellschaft.

CURRICULUM VITAE

Persönliche Angaben

Familienstand : ledig
Staatsangehörigkeit : deutsch
Geburtsdatum : 1. Mai 1974
Geburtsort : Frankfurt am Main
Eltern : Friedel und Ursula Haas (geb. Lehr)

Ausbildung

1980 bis 1984 : Besuch der Liebfrauenschule (Grundschule, Frankfurt am Main)
1984 bis 1993 : Besuch der Musterschule (Gymnasium, Frankfurt am Main)
Juni 1993 : Abitur
ab Oktober 1993 : Physikstudium an der Johann Wolfgang Goethe-Universität, Frankfurt am Main
im Oktober 1995 : Vordiplom
im November 1999 : Diplom; Titel der Diplomarbeit: „Ultraschalluntersuchungen an den Stanniden $\text{Yb}_3\text{Rh}_4\text{Sn}_{13}$ und $\text{Ca}_3\text{Rh}_4\text{Sn}_{13}$ “ (Physikalisches Institut, Prof. Dr. B. Lüthi, PD Dr. G. Bruls)
seit Februar 2000 : Promotion am Max-Planck-Institut für Biophysik (Frankfurt am Main) in der Abteilung für Molekulare Membranbiologie in der Gruppe von Herrn PD Dr. C. Roy D. Lancaster